Sheffield Hallam University

A Sheffield Hallam University thesis

An Infrared and Vision Based Temperature Monitoring System for Glass Forming Process

Carl Chang Tze Ming

A thesis submitted in partial fulfilment of the
requirements of
Sheffield Hallam University
for the degree of Master of Philosophy

March 2013

Abstract

One of the most important steps in optimising the glass container forming process is the determination of the glass temperature. Knowledge of the temperature is necessary because of the strong temperature dependence of the glass properties important to the forming process, especially glass viscosity. During the forming process, a few degrees change in glass temperature can change the glass viscosity, thus significantly affecting the moulding process. This is especially true for narrow neck glass bottle containers where viscosity is critical in maintaining the shape of the parison (unshaped mass of glass before moulded into final form) during the transfer from the blank to the mould, and in determining the forming characteristics during the final blow. By monitoring the glass temperature, it is possible to optimise the glass forming process, thus increasing production rates and/or improving product quality.

The current methods of temperature measurement which utilise handheld thermocouples are used to infer the parison's surface temperature by taking measurements of the blank mould. However, large errors are not uncommon due to inherent variability of operator's measurements, as well as the interference they introduce into the heat flow path. Also, the mould temperature measurement leads to assumptions about the parison temperature, which can be inaccurate. The use of thermal imaging technology to measure the temperature of parison offers an attractive alternative.

This thesis describes a proposed method to monitor the temperature of the glass during the glass forming process by measuring the temperature of the parison. Temperature measurement is performed using machine vision technology and a high speed infrared camera providing real time temperature data to an operator to monitor and control the glass forming process.

The system was developed and tested in a glass manufacturing plant. It is able to aid operators in optimising the I.S. machine by monitoring trend of the parison temperature. While the system is capable of providing temperature trend of the parisons, it is not able to provide reliable temperature reading of the parisons. This is due to the blurring artefact from the image captured, these undesirable artefact exist because of fast parison motion in relative to the speed

of the IR camera response time. This limitation causes the system to be less robust when it is used purely for temperature reading. However, when it is used to monitor trend of the parison temperature, the system could be used to improve and detect faults on the I.S machine. Faults in forming process are detected when the parison temperature starts to decrease or increase beyond a control limit. This information helps operator troubleshoot the I.S. machine and increase productivity.

Acknowledgements

Declaration

I declare that this thesis contains no material which has been accepted for the award of any other degree or diploma in any university of other institutes and affirms that, to the best of my knowledge, the thesis contains no material previously published or written by another person, except where due reference is made in the text of the thesis.

Carl Chang Tze Ming

Contents

Chapter 1

Introduction

Glass forming involves increasing the viscosity of molten glass to result in glass product in a specified shape; it involves controlling the reduction of the glass temperature to an essentially rigid state. Forming operations control this process with a variety of mechanisms, including mechanical pressures with compressed air and moulding plungers, heat extraction from glass physical contact with mould materials, applied cooling air and net radiant heat losses. Forming process are a two step process. In the first step (blank side) a so called parison is formed, which in second step (blow side) is blown into the final container.

Many efforts have been made to provide consistent glass chemistry to assure all its physical properties can be relied upon. For consistent glass temperature, improved forehearth equipment and advanced temperature control schemes have dramatically improved past deficiencies in this area. However, in spite of these efforts, there are still many variables that result in glass temperature being less homogeneous than desired. One area not typically considered involves factors influencing the gob after its formation and before its entry into a finish mould.

The main factors influencing the glass distribution and causing forming process a variation are as follows:

Gob condition

Viscosity, temperature, temperature homogeneity and gob shape.

Gob loading

Shear spray, gob delivery system.

Heat transfer

Cooling systems, mould materials and mould design.

I.S. machine variables

Plunger mechanism, invert mechanism and valves

Human behaviour

Swabbing and machine timing

In order to know how and to what extent each of these factors causes variation of glass distribution, monitoring system at the hot end is needed. In a joint research project with Graphoidal Developments, a non-contact infrared camera system which enable real time parison temperature measurement was developed. Thermal images provide representation of parison's temperature and its distribution. The system, which can be installed on existing as well as new machines, is non-invasive camera system, remotely mounted to the side of the machine. It measures and records parison's temperatures and display this information on a computer. At the most basic level, temperatures are displayed on a simple graph, easy to understand interface with the display in different colours if they are outside of pre-determined limits. Such technology can optimise parison forming by reducing temperature variation and improve quality.

1.1 Thesis outline

This thesis starts with a chapter on literature review that gives an overview of the glass container manufacturing process. Glass forming techniques are introduced to give the reader an understanding of the forming process where the temperature analysis would take place. The chapter reviews the existing technique and technology in the glass industry to obtain glass temperature information during the forming process. As thermal imaging is a core subject in this thesis, thermography theory and the common infrared technologies are also introduced. The chapter ends with a review of thermography specifically in the field of glass temperature measurement.

Chapter 3 gives an overview of the proposed solution to retrieve glass temperature information by utilising an infrared camera. This chapter discusses the benefits of such a system compared to the current technologies in the industry.

Chapter 4 discusses the first procedure of the proposed system which is to acquire infrared images continually and select those that have clear view of the parisons (partially formed molten glass) to be used for the subsequent temperature analysis. These images are termed as "valid images" in this thesis. These valid images are determined and selected by a machine vision algorithm which is discussed in detail.

Chapter 5 discusses one of the main problems encountered in the proposed system; that is, the inaccuracy in parison temperature measurement due to the varying distances of parison relative to the camera. Due to the variable distance between the parison and the camera, the measurement error are caused by the effect of the fixed focus distance, the atmospheric absorption of infrared radiation and, lastly, the slit response function or the pixel resolution that depicts the target object. Each of these factors and their contributions to the measurement error are discussed in this chapter.

Chapter 6 discusses another problem encountered in the system, the blurring artefacts observed in the captured infrared images. This problem arises because of the inherently slow response time of the microbolometer detector in typical infrared cameras. A comparison between a microbolometer based camera and the much faster photon detector based camera is discussed.

This chapter gives a description of image blurring. The image blur is categorised as either a shift variant blur or a shift invariant blur. The latter affects the image in the same way while the former affects the different parts of the image in different ways. The mathematical model for the Point Spread Function (PSF) that describes the blurring is derived from the thermal model of the microbolometer detector. This chapter then discusses the image restoration or the image deblurring process with a shift invariant blur. Three filters, namely, Direct Inverse filter, Wiener filter and Lucy Richardson filter, are introduced and compared.

The remaining part of the chapter deals with the rotational shift variant blur encountered in acquired images from the glass plant. The first method assumes that images are corrupted by linear blur and utilises the Radon transformation to determine the direction of the linear blur. The second method deals with this rotational shift variant blur in a more robust way by converting the rotational shift

variant blur into a linear shift invariant blur by utilising a technique known as image warp or image mapping. The final section of the chapter describes the combination of the image blurring algorithm and the image warping algorithm to deblur a rotational shift variant blur encountered in images from the glass plant.

The final chapter discusses the implementation of the algorithms discussed in the previous chapters. The chapter describes the software structure and the user interface of the system. Hardware aspects of the system are also described. The remaining part of the chapter investigates the performance of the system by analysing the results acquired from a trial performed in the glass plant.

Chapter 2

Literature Review

2.1 Overview of glass forming process

Natural glass, known as obsidian, was widely utilised by the prehistoric man, and glass has been made by people for approximately 9000 years. It was first known to be developed in the Middle East around 7000BC, and glass bottles were made in Egypt in 1500BC. By the Rennaissance, coloured glass, crystal and mirrors had all been developed and were being made in Venice. Glass has continued to be widely used despite the increase in usage of metal and plastic products for containers. It retains its popularity because of its versatility, relative cheapness, and, in an age of depleting resources, its recyclability.

Glass consists mainly of silica, this sand is washed and sifted to remove shells, stones and exceptionally large grains of sand, before it is mixed with other materials shown in Table 2-1 which control the colour and other properties (Wansbrough, 2012).

Ingredient	Composition
Sand	96 - 98 % SiO_2
Soda ash	Na_2CO_3
Limestone	$CaCO_3$
Cullet	glass

Table 2-1 Major ingredients in glass (Wansbrough 2012)

Structure of a glass plant

1) Batch Plant
2) Furnace
3) Working End
4) Forehearth
5) Feeder

6) Forming-Machine
7) Hot Ware Handling
8) Annealing Lehr
9) Inspection and Cold Ware Handling
10) Palletizing
11) Shrink Wrapping and Packing
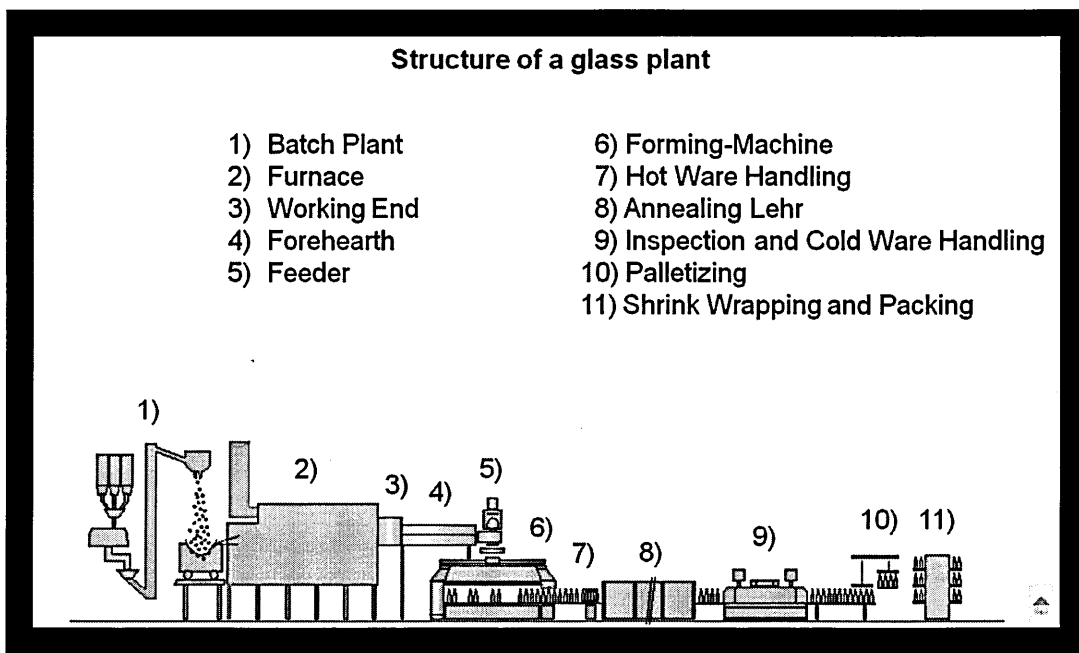
Figure 2-1 Glass plant overview (Port 2007)

Glass containers are made from their raw materials in a carefully controlled process, Figure 2-1 (Port, 2007) illustrates the structure of a glass plant and its major components. The following section (adapted from Quinn Glass, 2012) describes the major processes involved to produce a finished glass container.

Glass Melting

The furnace melts cullet (crushed, recycled glass), sand, soda ash, limestone, and other raw materials together. The furnace control system monitors and controls the firing temperature.

Glass Distribution

With the help of gravity, the glass stream is distributed to different forehearths for the respective production lines. Molten glass is conditioned in the forehearth and its temperature gradient is equalised to ensure uniform temperature homogeneity. The amount of molten glass allowed through the feeder is controlled by a ceramic plunger, which is timed with a shearing device that cuts the glass flow as it exits the feeder. The shearing creates a specific amount of molten glass, known as gob. The gob distributor then routes the gobs into blank moulds at the I.S Machine (Individual Section machine). The I.S. machine will be discussed in more detail in the next section.

Container Forming

Gobs of glass are delivered to blank moulds to form a parison. The ring finish and internal bore are created. It is then transferred to the mould side, where compressed air and vacuum are applied, stretching and cooling the parison to the exact inner cavity profile of the finish mould, forming the final shape of the container.

Annealing Lehr

Once released from the finish moulds, the bottles then cross the cooling plate where the temperature drops to around 900 degrees. They are then loaded into the Annealing Lehr, which brings the temperature back up to near melting point, then slowly reduces the temperature to below 900 degrees. This process relieves internal stresses, making the glass much more durable.

Cold End Coating

After annealing, a layer of polyethylene wax is applied via a water based emulsion. This makes the glass slippery, protecting it from scratching and stopping containers from sticking together when they are moved on a conveyor. The resultant invisible combined coating gives a virtually unscratchable surface to the glass.

Cold End Inspection

While travelling on to their final destination, the containers pass through a number of inspection instruments, which optically and physically test the containers for defects. Typical faults flagged up in this process include small cracks in the glass called checks, foreign inclusions called stones, bubbles in the glass, called blisters and thin glass. Rejected containers are recycled back into the furnace.

Palleting & Wrapping

Glass containers are stacked automatically on pallets and separated by cardboard into rows before undergoing the shrink wrapping process.

2.2 The I.S. Machine

The I.S. Machine or "Individual Section Machine" is designed to ensure efficient production so that operators can take one or more sections out of production for repairs without shutting down production in the other sections. Gobs enter the I.S. Machine and are formed into containers through a process of controlled shaping and cooling of the glass. The machines have anywhere between 6 and 20 sections and each section can produce one to four bottles simultaneously. The total time needed to produce a container varies, as an example beer and soda bottles take approximately 10 seconds. Depending on the container's size and shape, the machine's production speed can be as fast as 700 containers per minute according to (Emhart Glass, 2012). Figure 2-2 shows the I.S. Machine in operation.
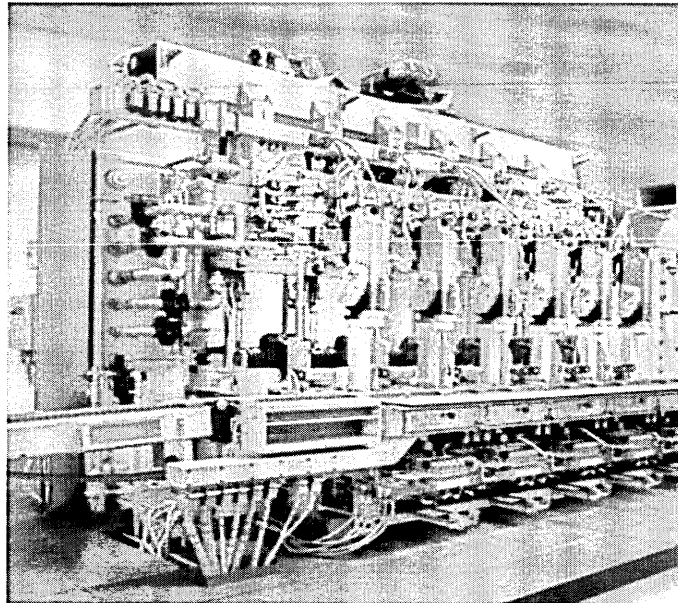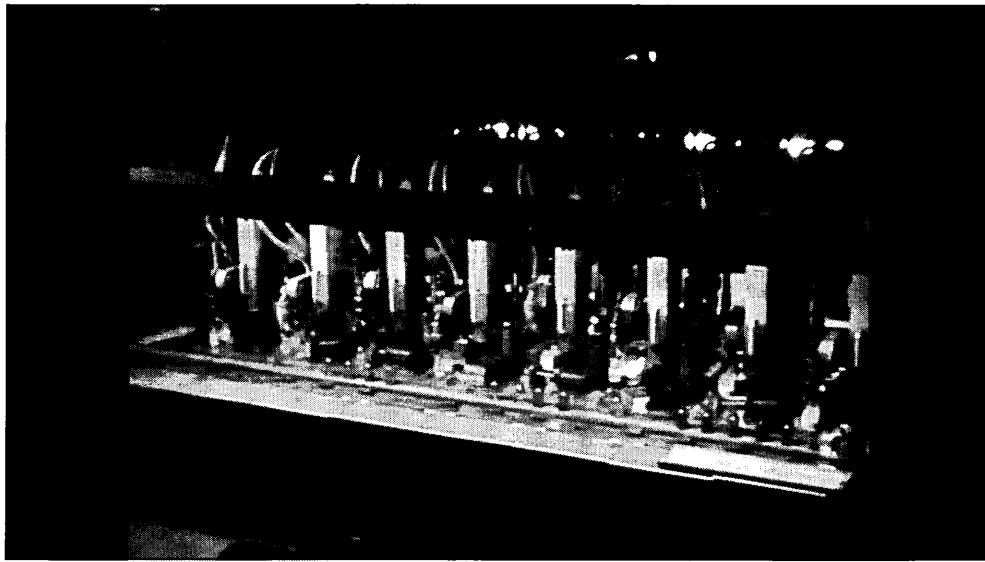
Figure 2-2 I.S. machine and I.S. machine in operation

2.3 Parison

The glass forming process starts from the feeder delivery system to the I.S. Machine. Molten glass flows with the help of gravity from the refiner through the forehearth. From there, it is carefully cooled to a uniform temperature and viscosity prior to reaching the feeder. Using the pull of gravity, the hot glass flows through the orifice at the bottom of the feeder. After the gob has been sheared from the feeder it falls into a series of chutes where it is delivered to the blank mould of the I.S. Machine.The gob drops into the blank side mould, which produces a hollow and partially formed container, known as a parison. From here, we can have three different types of forming processes to choose from, depending on the type of container being produced (Ardagh Group, 2011).

2.4 Glass forming processes

The three processes are called Blow & Blow, Wide Mouth Press & Blow, and Narrow Neck Press & Blow. During the Blow & Blow process, compressed air forces the molten gob into a partially formed container in the back side of the forming machine. The two Press & Blow processes use a metal plunger to shape the gob, allowing for manufactures to increase the overall productivity and reduce weight and variations in the thickness of beer and beverage bottles. The parison is now inverted over to the blow mould, where compressed air

9

blows the container into its final shape. The next sections which are adapted from (Emhart Glass, 2012) describe the three different forming processes.

2.4.1 Blow and Blow Process

In the Blow and Blow process, compressed air blows a cavity into the molten gob in the blank mould of the forming machine thereby creating a parison. From there the parison is transferred to the blow mould where compressed air is used to blow the bottle into its final shape. Figure 2-3 illustrate such a process.
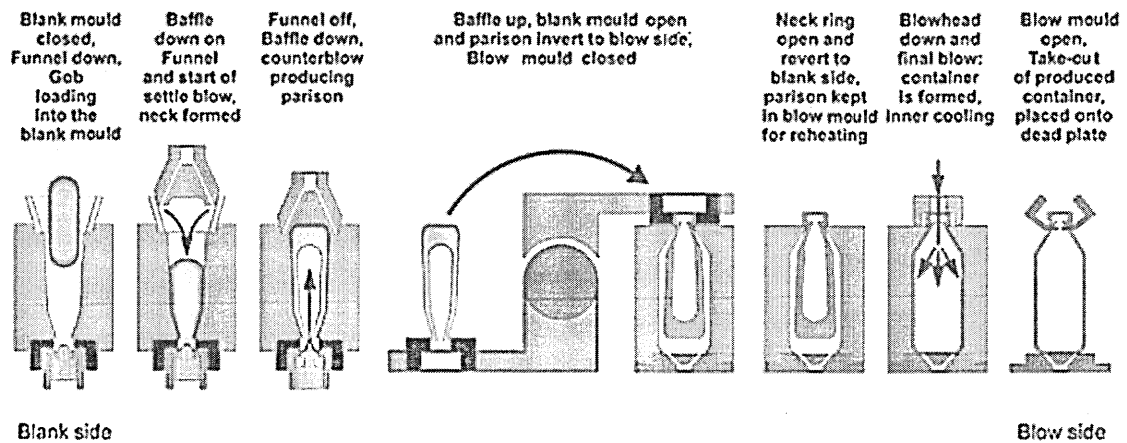
Figure 2-3 Blow and Blow Process (Emhart Glass 2012)

2.4.2 Wide Mouth Press and Blow Process

In the Wide Mouth Press and Blow process, a metal plunger is used to press the cavity into the gob to create the parison in the blank mould. The parison is then inverted and compressed air is blow into the container to form its final shape. This process is used to manufacture containers with wide finish diameters. Figure 2-4 illustrate a Wide Mouth Press and Blow Process.

Gob loading into the blank mould | Baffle down and start of plunger up | Plunger up and pressing finished. parison produced | Baffle up, blank mould open and panson invert to blow side | Neck ring open and revert to blank side. parison kept in blow mould for reheating | Blowhead down and final blow: container is formed | Take out of produced container

Blank side   Blow side
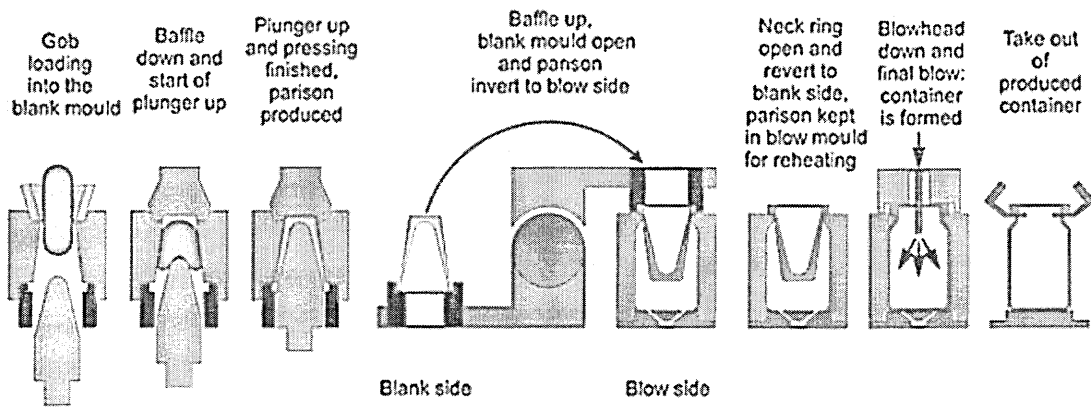
Figure 2-4 Press and Blow Process (Emhart Glass 2012)

2.4.3 Narrow Neck Press and Blow Process

The Narrow Neck Press and Blow process is similar to the Wide Mouth Press and Blow with the exception that the metal plunger in the blank mould is much smaller in diameter. This process is used to manufacture containers with narrow finish diameters. The introduction of this process has enabled glass manufacturers to increase overall productivity and reduce weight and variations in the thickness distribution of beer and beverage bottles. Figure 2-5 illustrate a Narrow Neck Press and Blow Process.

Blank mould closed, Gob loading into the blank mould | Baffle down and start of pressing by plunger up | Plunger up and pressing finished. parison produced | Baffle up, blank mould open and parison invert to blow side, Blow mould closed | Neck ring open and revert to blank side, parison kept in blow mould for reheating | Blowhead down and final blow: container is formed, inner cooling | Blow mould open, Take-out of produced container, placed onto dead plate

Blank side   Blow side

Figure 2-5 Narrow Neck Press and Blow Process (Emhart Glass 2012)

2.5 Current temperature measurement technology

The most common method to retrieve temperature information of the parison is by temperature measurement at the cavity of the blank mould. It is believed that the mould temperature has a direct relationship with the parison temperature as the parison is formed immediately once it leaves the blank mould. However, the exact temperature relationship is complex and difficult to model accurately due to various variables involved. Therefore, this method of mould temperature measurement to infer the parison temperature can be prone to large measurement errors.

The simplest and cheapest device used to measure mould temperature is a handheld pyrometer, as shown in Figure 2-6. With this device, an operator can retrieve temperature information by inserting the tip of the device into the cavity of the mould and probe for temperature reading.
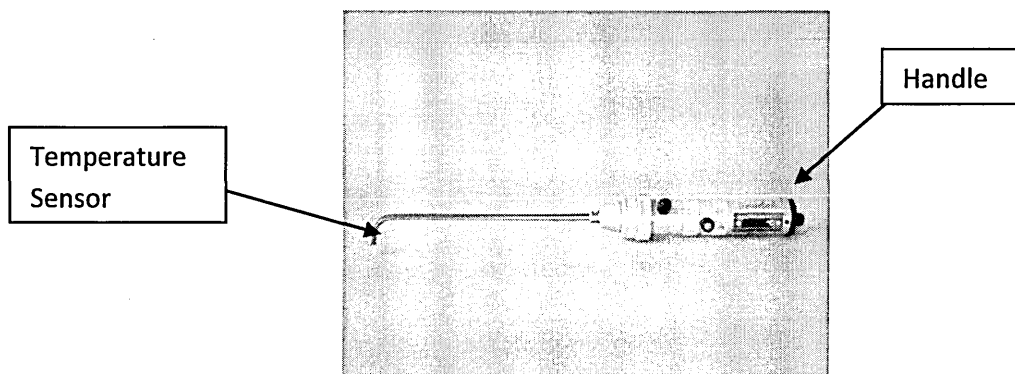
Figure 2-6 Handheld Pyrometer

As mentioned above, this device does not measure the temperature of the parison directly, instead it measures the temperature of the mould cavity, it leads to assumptions about the parison temperature, which can be inaccurate. Apart from that, it is difficult to obtain a consistent set of temperature data, this is because of the large temperature variation across the surface of the blank mould cavity. Hence, a consistent data set is only achievable if the operator manages to "probe" the handheld pyrometer at the exact position of the mould cavity for each measurement. Figure 2-6 (Hyre, 2009) shows a typical temperature profile of the blank mould cavity.

12

3. Baffle End

2. Body of Mould

1. Neckring

NNPB Forming Process

3. Baffle End

2. Body of Mould

1. Neckring
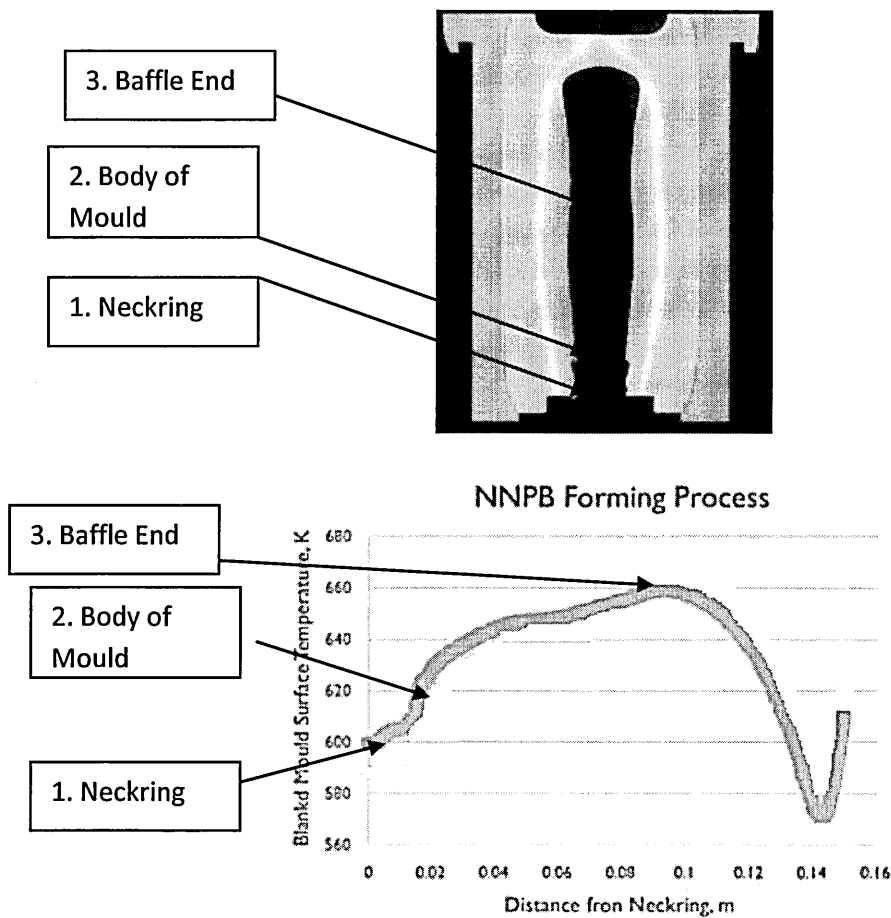
Figure 2-6 Temperature profile of mould cavity (Hyre 2007)

Apart from errors caused by the relative position of the probe, the angle at which the operator probes for temperature could introduce an additional error, as well as the duration of the contact made between the mould cavity and the tip of the probe. These errors are exacerbated when the data set is taken from multiple operators.

As this method of mould temperature measurement is a manual process and performed during the forming process, this can result in operators sustaining serious injuries. Figure 2-7 shows an operator taking measurements using the handheld pyrometer.
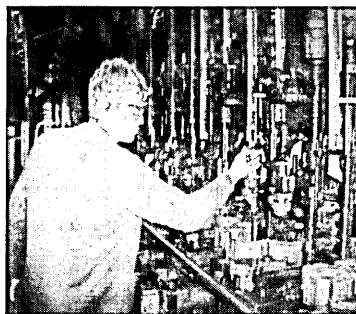
Figure 2-7 Operator taking measurements with a handheld pyrometer

13

There are companies in the glass industry that provide an automated solution for mould temperature measurement. One such company is Yamamura that provide a system where the temperature data are collected by a thermocouple embedded into the mould itself as shown in Figure 2-8. This way, there is no operator intervention which leads to a safer system and less operator related measurement errors. However, such a system requires extensive wiring for the thermocouples to operate. When installed in a harsh environment and with constant mechanical movement of the blank mould, this system is not robust. It is known that the thermocouples and its components need constant replacement. Apart from that, the moulds need additional modification to fit the thermocouples in place.
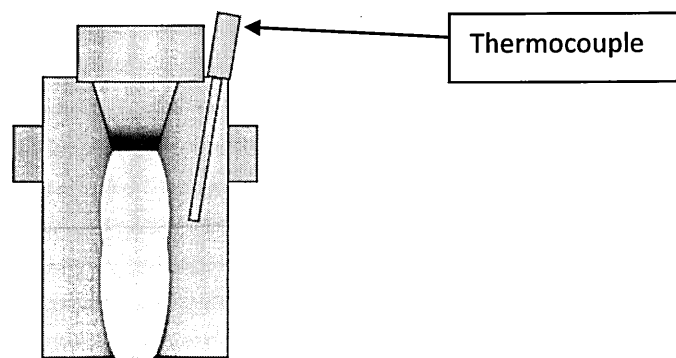
Figure 2-8 Thermocouple embedded into mould

Another system that measures the mould temperature is produced by Emhart Glass. It is a system based on pyrometry measurement where the pyrometer is fixed on a moving rail along the I.S. Machine. The pyrometer sensors at the top of the I.S. machine in Figure 2-9 measures several points of the section including blank moulds and plungers at approximately 2 metres away from the sensors. It moves from section to section along the rail to perform temperature measurements. As it only takes approximately eight seconds for an eight section to complete a machine cycle, the pyrometer moving across sections is not be able to "follow" the machine speed. Therefore, real time temperature data for each section cannot be achieved with this system. The field of view of a pyrometer system does not allow the sensors to be fixed at higher position from the moulds, this is because the region of spot measurement increases as the distance increases. Therefore such a setup could potentially be hazardous to the operator when the pyrometer is moving along the rail. Apart from that, this

14

system requires complex moving mechanical parts that are both difficult and expensive to maintain.
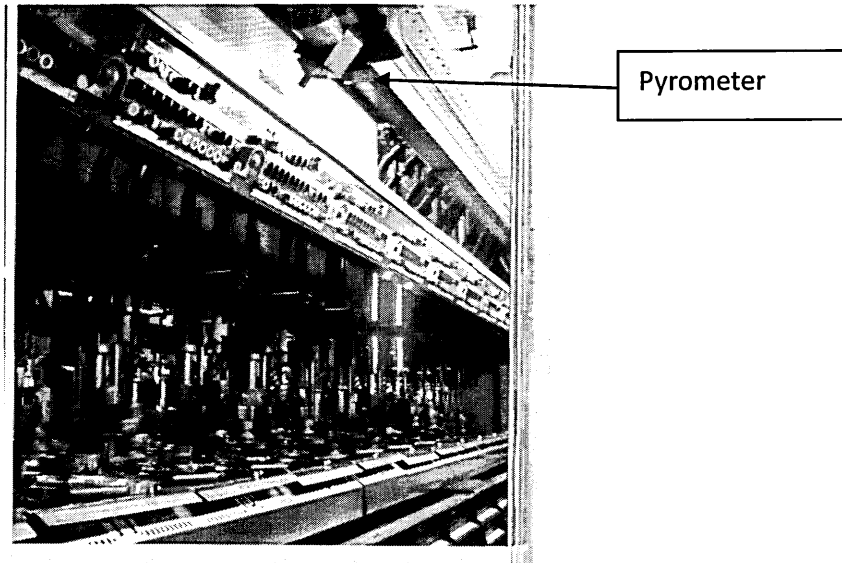
Figure 2-9 Emhart's pyrometry solution (Emhart Glass 2012)

Both systems mentioned above are based on mould temperature measurement; they do not measure the parison's temperature directly. A system produced by Xpar Vision is capable of parison temperature measurement. As shown in Figure 2-10, the mechanical operation is similar to the Emhart's system where the temperature sensor is mounted on a moving rail. Instead of a pyrometer, an infrared imager is used to perform temperature measurement of the parisons. However, due to the similarity of the mechanical design with the Emhart system, this system is not capable of taking temperature measurement of parisons from all sections in real time. Also the system requires expensive mechanical maintenance.
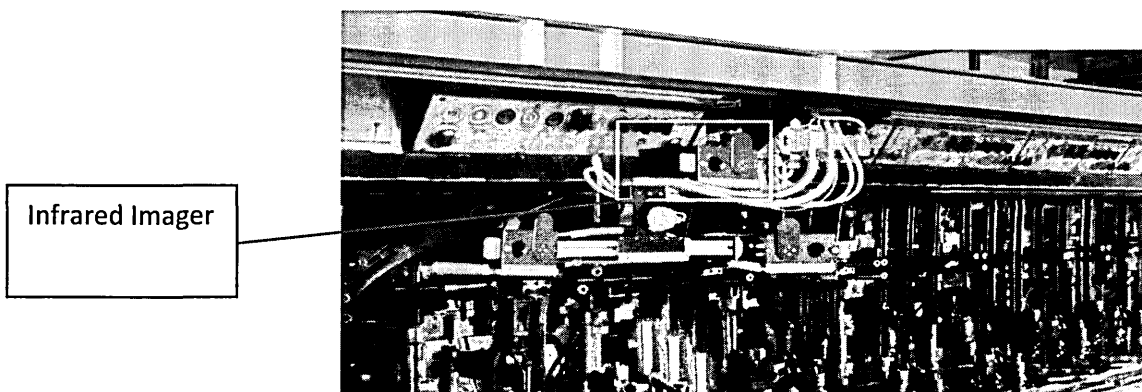
Figure 2-10 XparVision system (Xpar Vision 2012)

2.6 SPC (Statistical Process Control)

SPC is a method of quality control which uses statistical methods. SPC is applied in order to monitor and control a process. Monitoring and controlling the process ensures that it operates at its full potential. Key tools used in SPC include control charts, continuous improvement and design of experiments.

2.6.1 SPC Chart

Control charts are one of the most commonly used methods of Statistical Process Control (SPC) which monitors the stability of a process. The main features of a control chart include the data points, and upper and lower control limits. They visually display the fluctuations of a particular process variable, such as temperature in a way that lets the engineer determine whether these variations fall within the specified process limits.

A process may either be classified as in control or out of control. The boundaries for these classifications are set by calculating the mean, standard deviation and range of a set of process data collected when the process is under stable condition. Then, subsequent data can be compared to this already calculated mean, standard deviation and range to determine whether the new data fall within acceptable bounds. Control charts build on this basic idea of statistical analysis by plotting the mean or range of subsequent data against time.

2.6.2 EWMA Chart

One of the SPC chart is the EWMA (exponentially weighted moving averages) chart. It incorporates all the information in the sequence of sample points by plotting the weighted average of the current and previous observations. This feature makes the EWMA chart more sensitive in detecting small changes in the process parameters. Therefore, the EWMA chart is especially suitable when it is used to detect small shifts. For a conventional control chart technique (which is also known as Shewhart chart (Chris Bauman 2007)), the decision regarding the state of control of the process at any time, t, depends solely on the most recent measurement data from the process. For a EWMA control technique, the

16

decision depends on the EWMA statistic which is an exponentially weighted average of all prior data, including the most recent measurement. By choice of weighting factor α, the EWMA chart can be made sensitive to a small or gradual drift in the process. EWMA averages the data in a way that give less weight to data as they are further removed in time. The statistic that is calculated is:

$$EWMA_t = \alpha Y_t + (1 - \alpha)EWMA_{t-1} \qquad\qquad for\ t = 1,2,3,\ldots\ldots n. \qquad (2\text{-}1)$$

where

- $EWMA_0$ is the mean of historical data
- Y_t is the observation at time t
- n is the number of observations to be monitored including $EWMA_0$
- $0 < \alpha \le 1$ is a constant that determines the depth of memory of the EWMA.

The parameter α determines the rate at which the 'older' data enter into the calculation of the EWMA statistic. A value of $\alpha = 1$ implies that only the most recent measurement influences the EWMA and the statistic degrades to a conventional Shewart chart. Thus a large value of α gives more weight to the recent data and less wieght to the older data, while a small value of α gives more weight to the older data. According to (Hunter 1986), a value of $0.2 \le \alpha \le 0.3$ works well in practice.

2.7 Infrared Thermography

2.7.1 Infrared Spectrum

An infrared imager/camera determines the temperature of an object by measuring the electromagnetic energy it emits. The electromagnetic spectrum contains many different forms of electromagnetic emissions, including infrared light, x-rays, radio waves and several others (Figure 2-11). The only difference between these emissions is their wavelength. For infrared thermography, the typical wavelength is between 2 μm to 13 μm as highlighted in Figure 2-11.

Thermography makes use of the infrared spectral band. At the short wavelength end the boundary lies at the limit of visual perception, in the deep red. At the long wavelength end it merges with the microwave radio wavelengths, in the millimetre range.
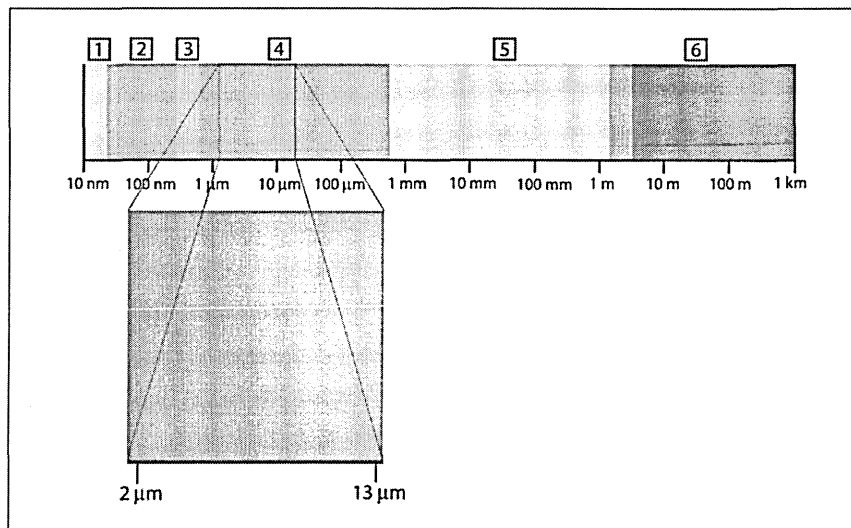
Figure 2-11 Electromagnetic spectrum. 1:X-ray; 2:UV; 3:Visible; 4:IR; 5:Microwave; 6:Radiowaves (FLIR AB 2005)

The spectrum of wavelengths emitted is a probability distribution depending only on an object's temperature. For a blackbody object, the intensity versus wave length is described by the Planck Radiation Law discussed in next section.

18

2.7.2 Radiation Law

The level of thermal radiation within a body can be expressed in the mathematical formula derived by Plank:

$$M_b(\lambda, T) = \frac{2\pi hc^2}{\lambda^5 \left(e^{\frac{hc}{\lambda kT}} - 1 \right)}$$

$$= \frac{c_1}{\lambda^5 \left(e^{\frac{c_2}{\lambda T}} - 1 \right)} \quad (Wm^{-2}\mu m^{-1}) \tag{2.2}$$

Where

M_{bb}	The spectral radiant exitance from a blackbody (an ideal radiator) within a spectral interval 1 µm wide at wavelength λ
c	The velocity of light = $3 \times 10^8 \; m/s$
h	Planck's constant = $6.617 \times 10^{-34} \; joule \; sec$
k	Boltzmann's constant = $1.380 \times 10^{-23} \; joule/K$
T	The absolute temperature (K) of the blackbody
λ	Wavelength(m)
c_1	The first radiation constant = $3.7418 \times 10^{-16} \; W \; m^2$
c_2	The second radiation constant = $1.4388 \times 10^{-2} \; K \; m$

The distribution of energy across the infrared spectrum is shown Figure 2-12. The curves in the graph have been constructed using Planck's Law.
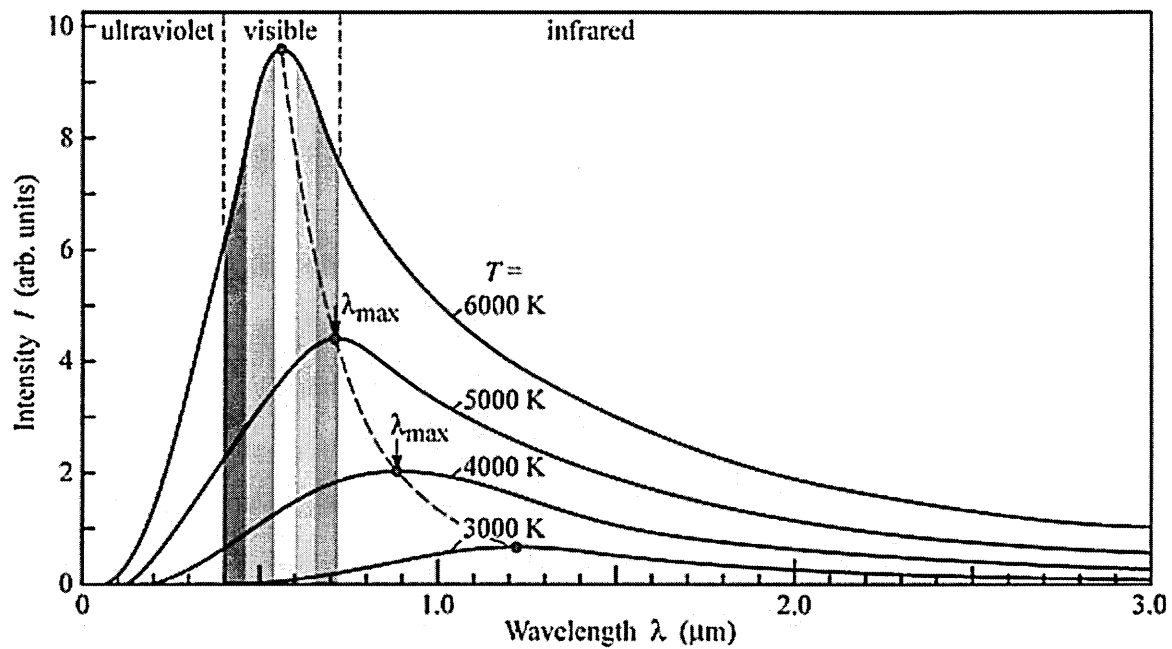
Figure 2-12 Spectral radiant emittance vs. wavelength (Northern Arizona
University 2009)

From the curves in Figure 2-12 (Northern Arizona University, 2009), it can be
seen that as the temperature of the object is increased, the curve increases in
amplitude and the peak value shifts towards the shorter wavelengths. As the
temperature increases, the peak wavelength shifts to the middle of the visible
band and the spread of frequencies makes the object appear white. At
wavelengths shorter than the peak, the rate of rise of the curve is very fast.
However, at wavelengths longer than the peak, the rate of decay of the curve is
quite slow and is roughly linear.

The relationship between the wavelength at which the peak energy occurs for a
given object temperature can be obtained by mathematical manipulation of
Plank's law. It is derived by equating to zero the derivative of the Planck's
function with respect to the wavelength λ .The result of the manipulation is
called Wien's Displacement Law.

$$\frac{dM_b(\lambda, T)}{d\lambda} = \frac{d}{d\lambda}\left\{\frac{c_1}{\lambda^5 \cdot [e^{\frac{c_2}{\lambda \cdot T}} - 1]}\right\} = 0$$

$$\lambda_{max} = \frac{2898}{T} \quad (\mu m)$$

20

This equation determines the wavelength λ_{max}, for which the radiant exitance of a black body at a given temperature T reaches a maximum (Minkina & Dudzik, 2009). This formula can be useful to calculate the wavelength at which peak energy will occur for any given target temperature.

From the Plank's Law, the total radiated energy from a blackbody can be calculated. This is expressed by a formula known as the Stefan–Boltzmann's Law. This total exitance is obtained by integrating Planck's formula from zero to infinity.

$$M_b = \int_{\lambda=0}^{\lambda=\infty} dM_b(\lambda, T) d\lambda = \int_{\lambda=0}^{\lambda=\infty} \frac{c_1}{\lambda^5 \cdot [e^{\frac{c_2}{\lambda \cdot T}} - 1]} d\lambda$$

The final Stefan–Boltzmann formula has the following form:

$$M_b(\lambda, T) = \frac{\pi^4 c_1}{15 c_2^4} \cdot T^4 = \sigma \cdot T^4$$

Where σ is the Stefan Boltzmann's constant ($5.67 \times 10^{-8}\, W/m^2 K^4$)

Wien's Displacement law gives the wavelength of the peak energy of the radiation distribution, while the Stefan-Boltzmann Law gives the total energy emitted at all wavelengths by the blackbody (the area under the Planck's curve). It can be seen from the Wien's Law that peak energy shifts to the shorter wavelengths as temperature increases. From the Stefan- Boltzmann Law, the peak energy level increases with the forth power of the temperature. Studying both these equations explains why the peak shifts to shorter wavelengths as temperate increases, and why peak level increases as the temperature increases.

2.7.3 Emissivity

So far, only blackbody radiation has been discussed. However, real objects almost never comply with these laws over an extended wavelength region since most objects of interest are not perfect blackbodies, this is where the object emissivity property plays an important role.

The ratio of actual radiation to the theoretical maximum blackbody radiation is the *emittance* ε:

$$\varepsilon_\lambda = \frac{M_{actual}(\lambda, T)}{M_{black\,body}(\lambda, T)}$$

Therefore, emittance is a number between 0 to 1. The better the radiative properties of the object, the higher its emittance. According to (FLIR AB 2005), there are three types of radiation sources, distinguished by the ways in which the spectral emittance of each varies with wavelength.

1) A blackbody, for which $\varepsilon_\lambda = \varepsilon = 1$

2) A greybody, for which $\varepsilon_\lambda = \varepsilon = constant\ less\ than\ 1$

3) A selective radiator, for which ε varies with wavelength

A perfect radiator with maximum radiation ability has ε = 1. Such a body is called a blackbody. A body with ε = 0 cannot radiate at all, no matter how hot it might be. An object that has the same emissivity ε for all wavelengths is called a greybody. For a greybody, Stefan Boltzmann's law takes the form of

$$W = \varepsilon \sigma T^4 [Watt/m^2]$$

This states that the total emissive energy of a grey body is the same as that of blackbody of the same temperature reduced in proportion to the value of the ε for the object. Figure 2-13 below shows the spectral radiation and emittances of the three different radiators.

22
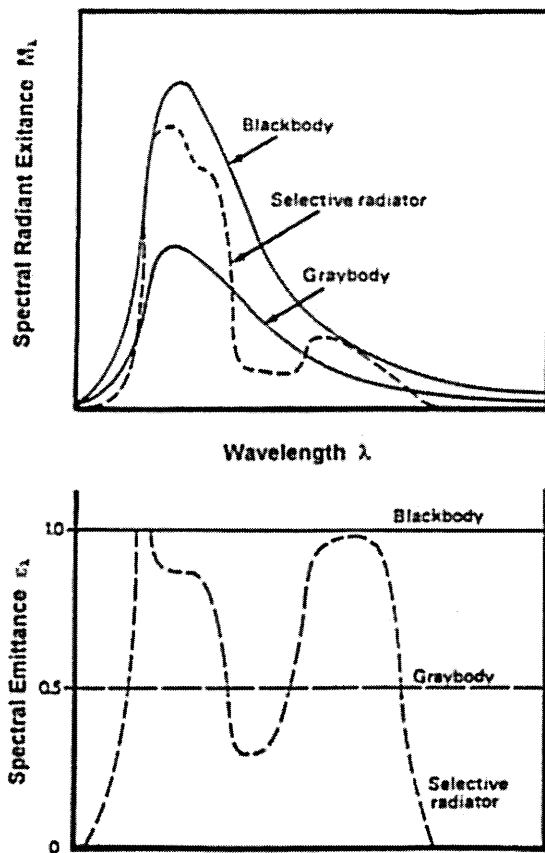
Figure 2-13 Spectral radiation from three different sources and their spectral emittances (FLIR AB 2005)

Still most bodies are neither blackbodies nor greybodies. The emissivity varies with wavelength, this is called a selective radiator and glass is such a radiator. As thermography operates only inside limited spectral ranges, in practice it is often possible to treat objects as greybodies (FLIR AB, 2005).

2.7.4 Mathematical model of temperature measurement with infrared camera

2.7.4.1 Reflection, absorption and transmission

There is a simple relationship between emittance and the other properties of a radiator, its reflectance ρ, absorbtance α, and transmittance τ, a relationship that can be described by means of Figure 2-14. W is the radiation power. Some of the radiation, ρW, is reflected back. Depending on the surface condition, the reflection could be more or less diffused. Another portion of the incident

23

radiation, αW, is absorbed in the plate material when passing through. The remaining part, τW, is transmitted through the material.
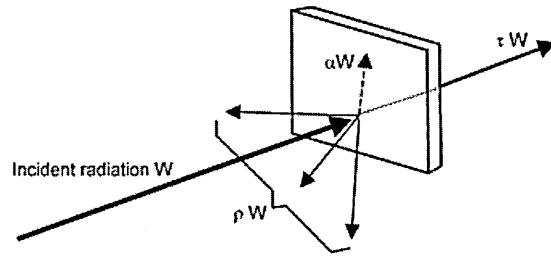
Figure 2-14 Reflection, absorption and transmission of radiation (Minkina and Dudzik 2009)

The relationship among the three radiations is based on the conservation of energy which is the sum of reflected, absorbed and transmitted energies equals the incident energy:

$$\rho W + \alpha W + \tau W = W \qquad (2.3)$$

or, eliminating the power, W from each term, and taking into account spectral variations of all parameters.

$$\rho_\lambda + \alpha_\lambda + \tau_\lambda = 1 \qquad (2.4)$$

All these parameters are dimensionless ratios such as the emittance with values between 0 and 1. According to another fundamental law for infrared radiation, the Kirchhoff's Law, for any material the spectral emittance and the spectral absorbance are equal at any specified temperature and wavelength, that is

$$\varepsilon_\lambda = \alpha_\lambda \qquad (2.5)$$

Using the Kirchhoff's Law, the equation can now be rewritten:

$$\rho_\lambda + \varepsilon_\lambda + \tau_\lambda = 1 \qquad (2.6)$$

This fundamental equation will be used extensively in the derivation of the measurement formula described in the next section.

24

2.7.4.2 Measurement formula
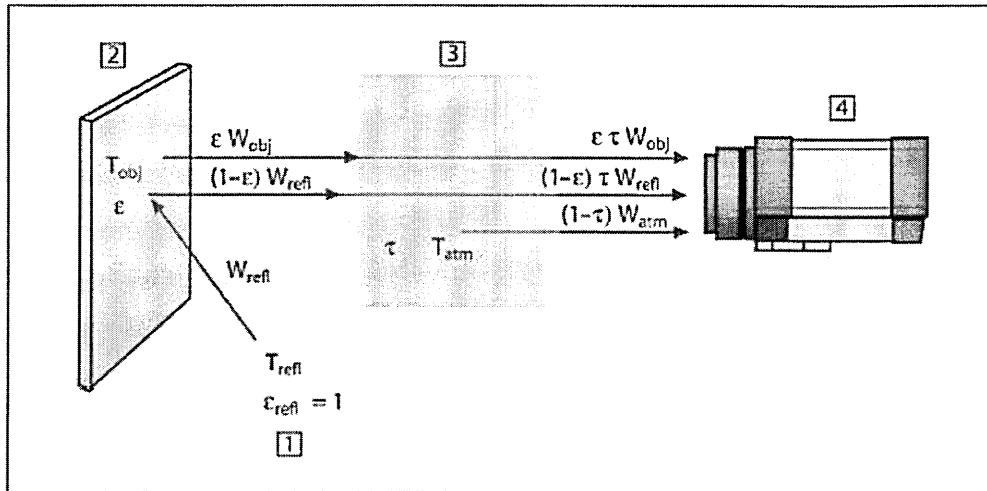
Figure 2-15 Measurement formula (Minkina and Dudzik 2009)

The radiation that impinges on the IR camera lens comes from three different sources according to (Minkina & Dudzik, 2009)(Figure 2-15). The camera receives radiation from the target object, plus radiation from its surroundings that has been reflected onto the object's surface. Both of these radiation components become attenuated when they pass through the atmosphere. Since the atmosphere absorbs part of the radiation, it will also radiate some itself according to Kirchhoff's law.

Given this situation, the formula for the calculation of the object's temperature from a calibrated camera's output can be derived.

1. *Emission from the object* $= \varepsilon \cdot \tau \cdot W_{obj}$

where ε is the emissivity of the object and τ is the transmittance of the atmosphere.

2. *Reflected emission from ambient sources* $= (1 - \varepsilon) \cdot \tau \cdot W_{refl}$

where $(1 - \varepsilon)$ is the reflectance of the object. (It is assumed that the temperature T_{refl} is the same for all emitting surfaces within the half sphere seen from a point on the object's surface.)

3. *Emission from atmosphere* $= (1 - \tau) \cdot W_{atm}$

, where $(1 - \tau)$ is the emissivity of the atmosphere. The total radiation power received by the camera can now be written:

25

$$W_{tot} = \varepsilon \cdot \tau \cdot W_{obj} + (1 - \varepsilon) \cdot \tau \cdot W_{refl} + (1 - \tau) \cdot w_{atm} \qquad (2.7)$$

,where ε is the object emissivity, τ is the transmission through the atmosphere, and T_{atm} is the temperature of the atmosphere.

Assume that the received radiation power W from a blackbody source of temperature T_{Source} on short distance generates a camera output voltage signal U_{Source} that is proportional to the power input (power linear camera). Then this can be related by:

$$U_{Source} = CW(T_{Source})$$

or with simplified notation:

$$U_{Source} = CW_{Source}$$

where C is constant.

Multiply each term by the constant C and replace $C \cdot W$ products by the corresponding U, equation 2.6 becomes:

$$U_{tot} = \varepsilon \cdot \tau \cdot U_{obj} + (1 - \varepsilon) \cdot \tau \cdot U_{refl} + (1 - \tau).U_{atm} \qquad (2.8)$$

Rearranging the equation above, we get:

$$U_{obj} = \frac{1}{\varepsilon \cdot \tau} \cdot U_{tot} - \frac{(1-\varepsilon)}{\varepsilon} \cdot U_{refl} + \frac{(1-\tau)}{\varepsilon \cdot \tau}.U_{atm} \qquad (2.9)$$

(FLIR AB 2005) state that this is the general measurement formula used in the FLIR systems thermographic equipment. The voltages of the formula are:

U_{obj}	Calculated camera output voltage for a blackbody of temperature T_{obj} i.e voltage that can be directly converted into true requested object temperature
U_{tot}	Measured camera output voltage for the actual case
U_{refl}	Theoretical camera output voltage for a blackbody of temperature T_{refl} according to the calibration
U_{atm}	Theoretical camera output voltage for a blackbody of temperature T_{atm} according to the calibration

In order for the camera to calibrate its infrared image, the infrared camera software requires inputs for the emissivity of the object, atmospheric attenuation and temperature, and temperature of the ambient surroundings, as described from the measurement equation 2.9.

2.7.5 Thermal imager

A thermal imaging system (Figure 2-16) creates an electronic picture of a scene. The picture may be converted to colour (pseudo colour or false colour) where red indicates hot areas and blue represents cool objects. When presented with gray-scale values, a bright area indicates hotter objects.

SCENE WITH
TEMPERATURE
GRADIENTS

VISIBLE
IMAGE

THERMAL
IMAGING
SYSTEM
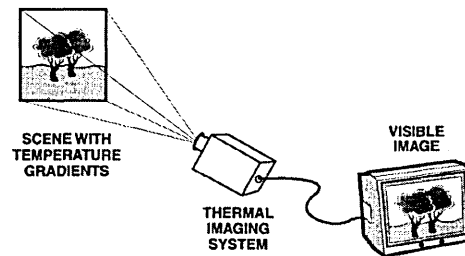
Figure 2-16 Thermal imaging system (L.Williams 2009)

2.7.6 Components of a thermal imaging system

According to (L.Williams, 2009), the essential components that make up a thermal imaging system are:

| Infrared lens system | Scanner mechanism | Detector(s) & associated electronics |

| Display | Video-signal generator |
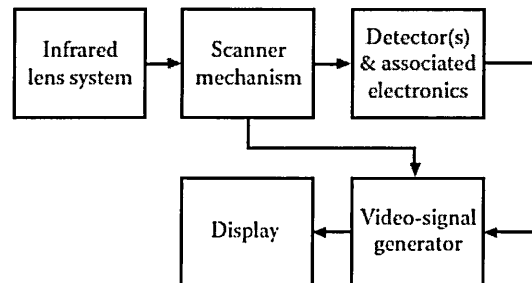
Figure 2-17 Components of an imaging system (L.Williams 2009)

- An optical system that can form an image of an external scene using radiation in the thermal wavelength range.

- One or more detector elements that can convert this radiation into electrical signals proportional to the radiation falling onto them.

- Some systems require a scanning mechanism that scans the thermal image in a regular pattern across the detector element(s), although most modern imagers do not require this, since they use large detector arrays that completely cover the field of view of the imager. This will be discussed in more detail in a later section.

- An electronic processor that can process the detector outputs, in conjunction with the data from the scan mechanism, and can convert them into a video signal.

- A display unit that generates a visual image from the video signal.

2.7.7 Scanning system

The function of a scanning mechanism is to move the image formed by the lens system over the detector element(s) in a well-controlled fashion. Scanner systems normally fall into one of three classes as represented by the one-dimensional (1D) oscillating mirror scanner arrangements illustrated in Figure 2-18 (L.Williams, 2009). In the first of these (Figure 2-18(a)), the scanner occupies the space between the image-forming optical system and the detector. In the next arrangement (Figure 2-18(b)), the scanner is between the external object and the image-forming optical system, and in the third arrangement the scanner is placed between a focal front end and the image-forming back end of the optical system. In this thesis, the focus will be on a system without a scanning system, a starring array.
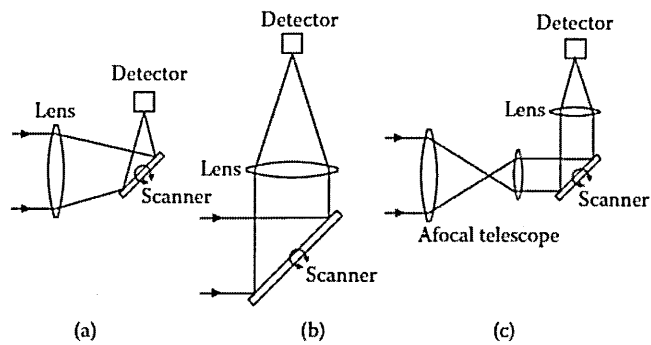
Figure 2-18 Three classes of scanning system: (a) Image space, (b) Object space, and (c) Afocal (L.Williams 2009)

2.7.8 Starring array

The ultimate arrangement is to completely fill the image plane with detector elements and to do away with the scanning mechanism, as illustrated in Figure 2-19. Most modern imagers conform to this arrangement where and when technical and economic considerations allow the construction of large two-dimensional (2D) detector arrays. In this thesis, this arrangement of imaging system is referred to as thermal camera or infrared camera. For a thermal camera the spatial resolution for a given field of view (FOV) will depend on the actual number of detector elements in the image plane.
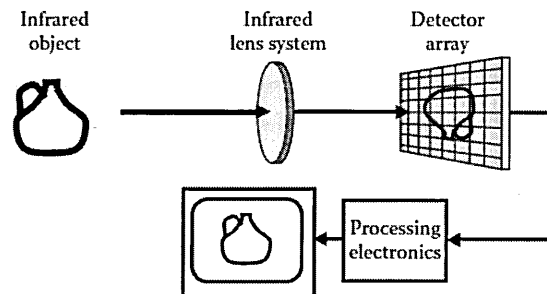
Figure 2-19 Schematic of a starring array system (L.Williams 2009)

2.7.9 Infrared detector

Possibly, the most important part of a thermal camera is the detector or detector array. There are basically two types of thermal infrared (IR) detectors. The first depends on the IR radiation heating the detector element, with the resulting temperature rise then triggering some other physical mechanism that is taken as a measure of the radiation falling onto the element. This type of detector is generally known as a thermal detector (L.Williams 2009).

The second type of detector is one where the photons, which constitute the incident radiation, interact at an atomic or molecular level with the material of the detector to produce charge carriers that generate a voltage across the detector element, or a change in its electrical resistance. The mechanism usually involves an electron absorbing a photon and, as a result, moving from one quantum energy level to another. This type of detector is usually referred to as a photon or quantum detector (L.Williams 2009).

In general, photon detectors provide greater sensitivity than thermal detectors. However, to achieve this better performance they usually need to be cooled in order for the charge carriers to populate the quantum energy levels where they can have the desired interaction with the incident photons. Thermal detectors have the great advantage that they do not normally require cooling, although some types of thermal detectors require their temperature to be controlled to ensure that they operate under optimum conditions (L.Williams, 2009).

2.7.9.1 Photon/quantum detectors

Figure 2-20 Operating principle of photon/quantum detectors (FLIR AB 2012)

In materials used for quantum detectors, at room temperature there are electrons at different energy levels. Some electrons have sufficient thermal energy to be in the conduction band, meaning the electrons are free to move and the material can conduct an electrical current. Most of the electrons, however, are found in the valence band, where they do not carry any current because they cannot move freely. When the material is cooled t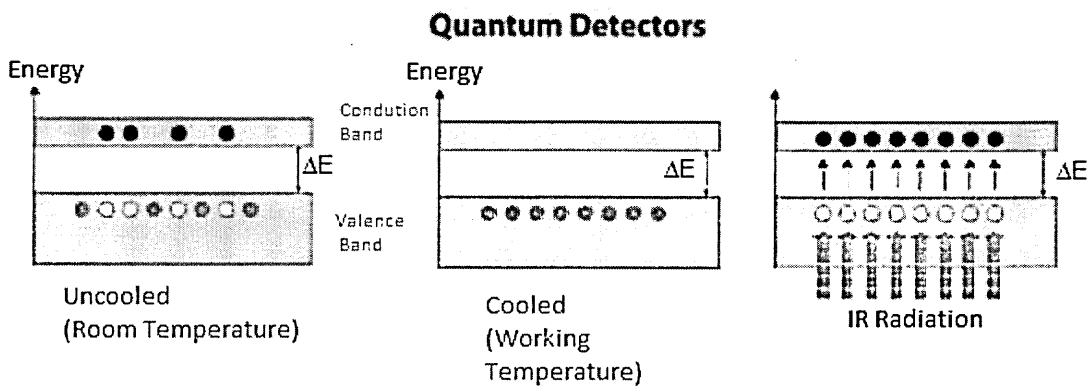o a low enough temperature, which varies with the chosen material, the thermal energy of the electrons may be so low that there are none in the conduction band. Hence, the material cannot carry any current. When these materials are exposed to incident photons, and the photons have sufficient energy, this energy can stimulate an electron in the valence band, causing it to move up into the conduction band. Thus the material (the detector) can carry a photocurrent, which is proportional to the intensity of the incident radiation. There is a very exact lowest energy of the incident photons that will allow an electron to jump from the valence band into the conduction band. This energy is related to a certain wavelength, the cutoff wavelength, λ (FLIR AB, 2012).

$$E_g = \frac{hc}{\lambda}$$ (2.10)

Where E_g= Energy gap corresponding to the quantum level change

h = Planck's constant

c = Velocity of light

Following are some of the photon detectors that are most commonly used:

Cadmium mercury telluride: This is usually referred to as CMT or MCT and can be constructed to operate as a photovoltaic device (i.e., where the incident radiation generates a voltage) or as a photoconductive device (i.e., where the incident radiation alters the effective resistance of the device). By adjusting the composition of the material, CMT detectors can work in either the 3–5μm band or the 8–14 μm. CMT can in fact be optimised to work at wavelengths as high as 16 μm or slightly more.

Indium antimonide (InSb): This material is only useful in the 3–5 μm band and can be constructed to operate as a photovoltaic device or as a photoconductive device. To achieve its full potential, it needs to be cooled to liquid nitrogen

31

temperatures, although it can also be made to have a useful response at the higher temperature of 195K.

Quantum well (QWIP) devices: The basic principle is that the required quantized energy levels and photon absorption is achieved by using certain geometrical structures that include gratings and thin film layers. Different material combinations can be used for making these devices, one of these being aluminum gallium arsenide and gallium arsenide. They can be made to cover various wavelength bands in the range of approximately 3–20μm and can be built as large starring arrays (L.Williams, 2009).

2.7.9.2 Thermal detectors

As temperature sensors, thermal detectors can sense all wavelengths and therefore filters are used to limit the spectral response. Thermal detectors generally have much lower sensitivity than photon detectors. As a result, they probably will not replace photon detectors in critical, low signal-to-noise applications (C.Holst, 2000). Thermal detectors can be classified as thermometers, thermocouples, thermopiles and resistive bolometers.

In this thesis, the thermal camera used is based on bolometers. The operating principle of a bolometer is based on the changes in resistance of the bolometer element due to the temperature changes. Advances in the micromachining of silicon have led to the field of microbolometers. A microbolometer consists of an array of bolometers fabricated directly onto a silicon readout circuit. This technology has demonstrated excellent imagery in the IR. Microbolometers can operate near room temperature and therefore, do not need vacuum evacuated, cryogenically cooled dewars. This advantage brings with it the possibility of producing low cost systems for both military and commercial markets (Sharma, 2004).
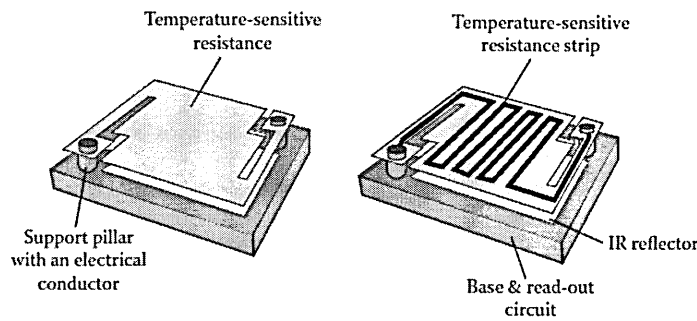
Figure 2-21 Example of construction of a single pixel in a bolometer array
(L.Williams 2009)

The form of construction of this type of array is illustrated in Figure 2-21. Each resistive element is deposited onto a silicon platform that has a very small heat capacity and is thermally isolated by an air gap from the base silicon wafer. Small pillars, or narrow strips of material, support the platforms and provide the electrical connection to the resistive element. The base wafer will have the readout and processing circuits. The viability of such arrays depends on the ability to make elements having a very small heat capacity that are well isolated thermally from their base support. The resistive elements are typically made by depositing materials such as vanadium oxide and titanium oxide on the substrate. However, amorphous silicon has also been used very successfully. An important requirement of these elements is that they should have a high absorption at the operating wavelengths (L.Williams, 2009).

2.7.10 Filter adaptation

Materials that are transparent or opaque to infrared (IR) wavelengths present problems in noncontact temperature measurements with an IR camera. With transparent materials, the camera sees through them and records a temperature that is a combination of the material itself and that which is behind it. In the second case, when an IR camera needs to see through a material to measure the temperature of an object behind it, signal attenuation and ambient reflections can make accurate temperature readings difficult or impossible. In some cases, an IR filter can be placed in the camera's optical path to overcome these problems.

IR cameras inherently measure radiance not temperature. However, the camera's software converts radiance measurements into temperatures by using the known emissivity of a target object and applying internal calibration data for the camera's spectral response. The spectral response is determined primarily by the camera's lens and detector. For many objects, emissivity is a function of their radiance wavelength and is further influenced by their temperature, the angle at which they are viewed by a camera and other factors. An object whose emissivity varies strongly with wavelength is called a selective radiator as discussed in the previous section. Transparent materials, such as glass, tend to be selective radiators. In other words, their degree of transparency varies with the wavelength. There may be IR wavelengths where they are essentially opaque due to absorption. Since, according to Kirchhoff's Law, a good absorber is also a good emitter, this opens the possibility of measuring the temperature by using a filter to cut off IR wavelength where the glass is perceived as transparent to the IR camera.

Inserting a spectral filter into the camera's optical path is called spectral adaptation. Ultimately, an optical (IR) filter must be selected that blocks all wavelengths except the band where the object absorbs. This ensures that the object has high emissivity within that band. Spectral adaptation could also be applied the opposite way, i.e., selection of a spectral band where the transmission through a medium is as high as possible. The purpose would be to enable measurement on an object by seeing through the medium without any interference and this medium could be the ordinary atmosphere. This will be discussed further in Chapter 5 where the effect of the atmosphere absorption on the temperature reading is investigated.
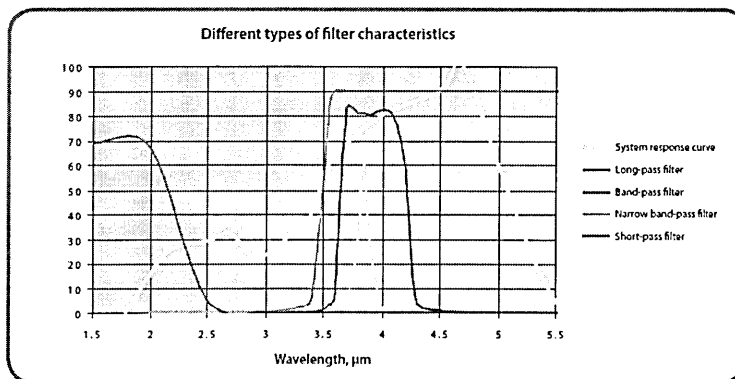
Figure 2-22 Response curves for different types of filters (FLIR AB 2012)

In spectral adaptation, filters are used in order to suppress or transmit certain wavelengths. Filters can be described as short-pass (SP), long-pass (LP), band-pass (BP), and narrow band-pass (NBP). For temperature measurements on transparent materials, the filter selected must provide a band of essentially complete absorption. Incomplete absorption can be used, at least theoretically, provided that both absorptance and reflectance are known and stable at the absorption band (FLIR AB, 2012). Unfortunately, absorption often varies with both temperature and thickness of the material and these will be discussed more in depth in the later section with the focus on glass temperature measurement.

2.7.11 Infrared thermography on glass

Glass is a highly selective material in the infrared region. It progressively passes from a relatively high transmission in the short wavelength band to opacity in the long wavelength band. Soda-lime-silica glass is the most common type of industrial glass for products such as sheet plates and bottles (Bramble, 2012). Figure 2-16 shows a typical example where the transmission factor is approximately 90 % from below 0.5 µm up to 2.3 µm, and close to 0 % above 3.7 µm (Valley Design, 2012).
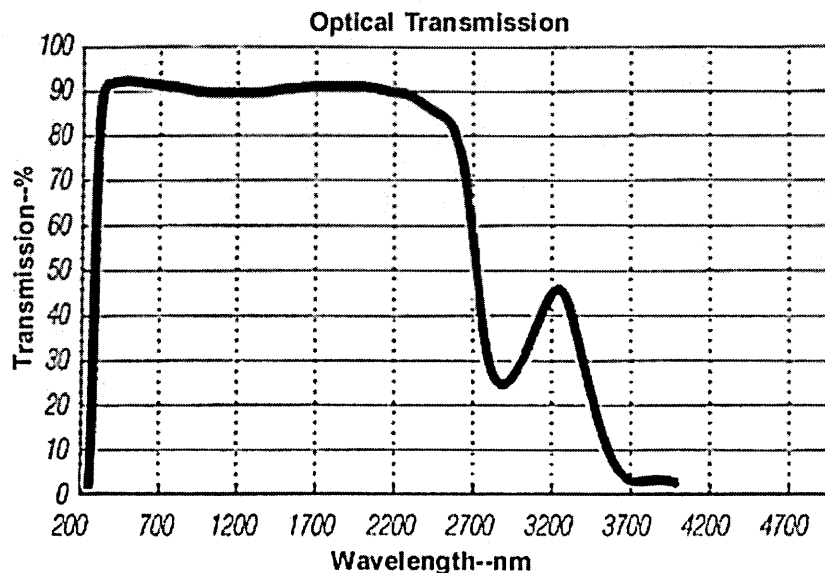
Figure 2-23 Transmission of a typical glass material (Valley Design 2012)

In between, i.e. in the mid wavelength region, glass relative transparency depends on its thickness, additives, and melting techniques. Figure 2-24 shows the influence of the thickness on the transmission factor.
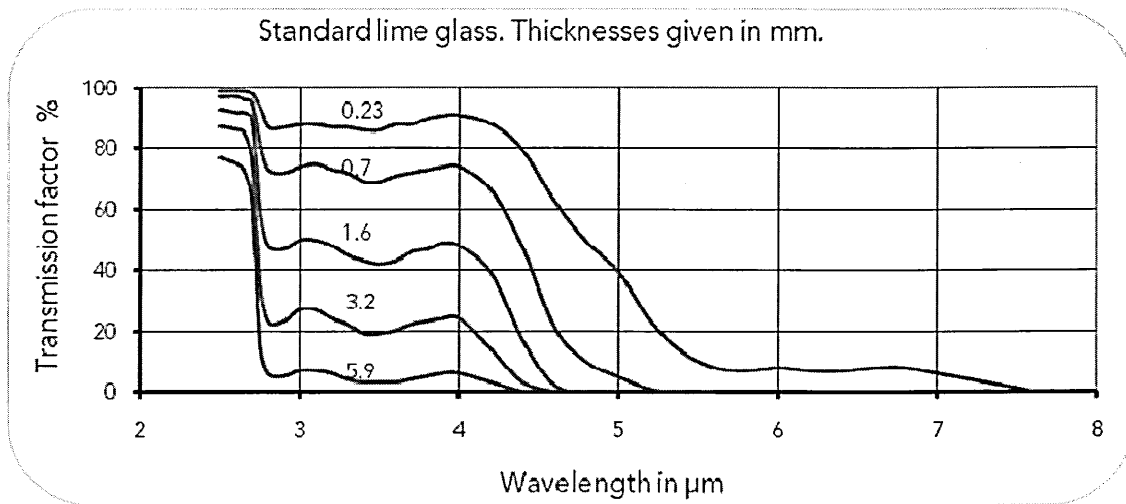
Figure 2-24 Influence of thickness to glass transmission (FLIR AB 2012)

The composition of soda lime silica glasses might vary depending on the intended use and sometimes the glass is coloured, however the spectral characteristics will not change significantly according to (FLIR AB, 2012). From Figure 2-24, for surface temperature measurement, the camera spectral response should be restricted to wavelengths above 4.8µm for thicknesses above 1.6mm. For thinner glass, the wavelength should be higher at approximately 5.4µm for 0.7mm and 7.6µm for 0.23mm. Therefore, for thinner glass, a long wavelength camera should be used, for example in the sheet glass work where glass is too transparent for shorter wavelength measurements. For such applications, 8-14 µm is commonly used when reflectance is not a problem. Table 2-2 from (Calex Electronics Limited, 2012) shows the approximate depth of measurement with different wavelengths used

Wavelength (µm)	Depth of Measurement (mm)
0.7 to 1.0	100 to 125
2.2	50 to 75
3.9	10
5.1	1.5
7.9	Surface
8 to 14	Surface

Table 2-2 Approximate depth of measurement in clear glass vs IR camera wavelength (Calex Electronics Limited 2012)

Spectral adaptation to glass

- Glass transmission curve
- SW/TE MCT spectral response
- 4.7μm LP filter curve
- 5.0μm NBP filter curve

(y-axis: Transmission %, x-axis: Wavelength, μm)

Figure 2-25 Two alternative filters for glass measurement with a short wavelength camera (FLIR AB 2012)

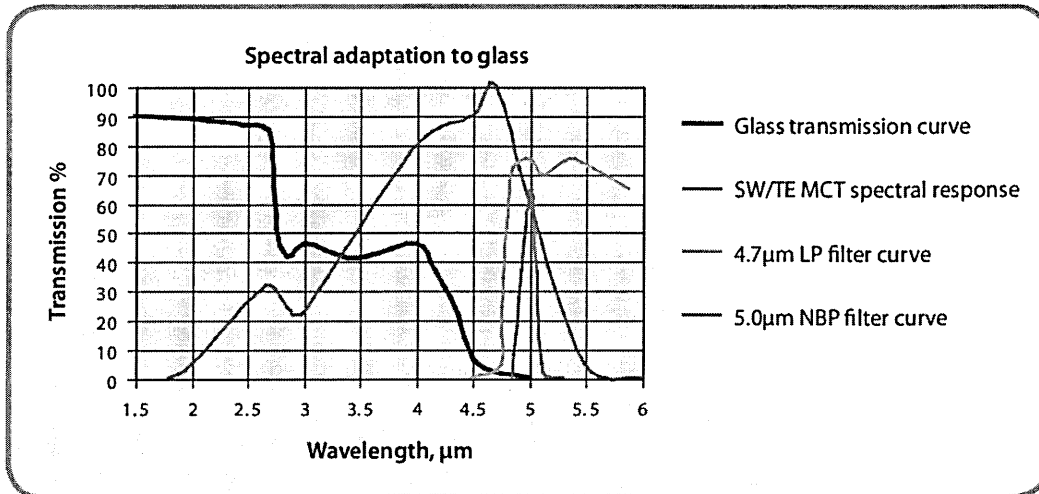For a short wavelength camera, a filter should be used in order to avoid the high transmission region. From Figure 2-25, one could use a cut-on filter (i.e. a long pass filter). Such a filter would cut on wavelength at 4.7 microns as represented by the green line in Figure 2-25. FLIR names such a filter as GLS. There is another filter that could be used, named as GHT which is a narrow band pass filter with its centre wavelength at 5.0 microns where glass will appear opaque. When either filter is used with a short wavelength camera, one could obtain high emissivity value for glass measurement.

As for long wavelength cameras, filter adaption is not always necessary since the uncooled detector spectral response lies between 8-14 μm, where the transmission is almost zero. However, there are other factors to be considered, one of such factor is the reflectance of the glass. From Figure 2-26 (FLIR AB, 2012), it can be seen that the peak of the reflectance occurs between 8-12 μm. From 7.5 μm, it increases, reaches a maximum at around 9.5 μm (up to more than 30%), and then slowly goes down. Therefore, when using a long wavelength camera, reflectance must be taken into consideration for glass temperature measurement. For example, a plate glass annealed between a double rows of heaters, would preclude the use of an instrument with this 8-14 μm spectral range. Instead, an instrument sensitive at 5 μm could read the

temperature without errors due to reflection. (Calex Electronics Limited 2012) state that the 5 μm instrument would read to a depth of about 1 mm, while a 7.9 μm instrument would read the surface only.
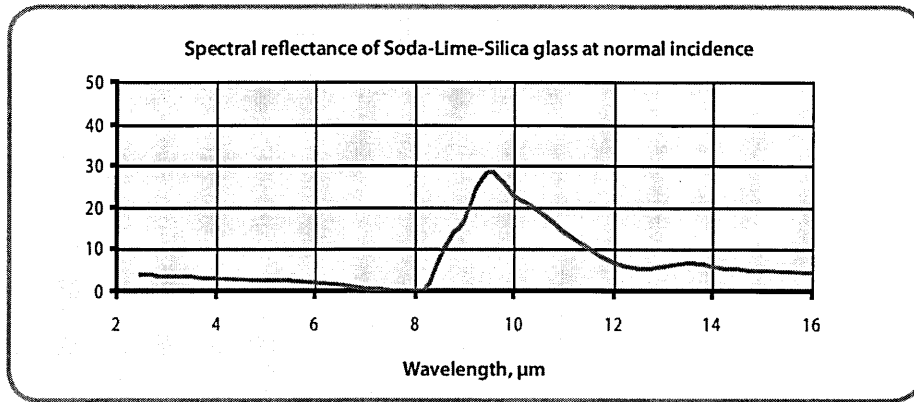
Figure 2-26 Spectral reflectance of soda-lime-silica at normal incidence (FLIR AB 2012)

Figure 2-26 is only valid for normal incidence. Fortunately, the reflectance does not change much with angle of incidence up to approximately 45 degrees, as shown in Figure 2-27. Therefore, it is not advisable to go above an angle of 35° or 40°, otherwise the reflection factor suddenly increases as shown in Figure 2-27 (FLIR AB, 2012).
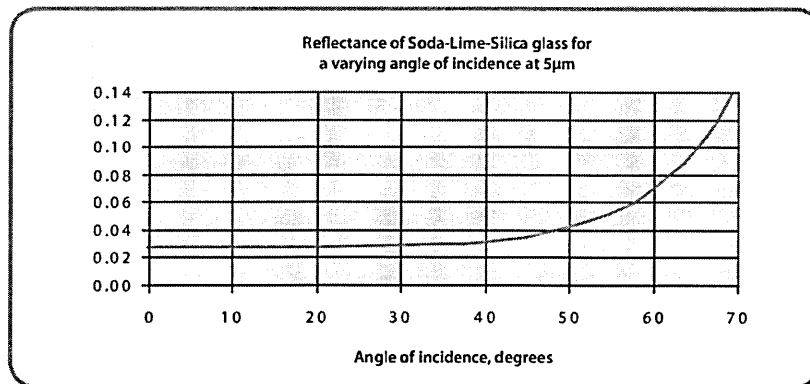
Figure 2-27 Glass Reflectance as a function of the camera viewing angle relative to normal incidence (FLIR AB 2012)

In the long wavelength region, regardless its thickness, glass is opaque. For surface glass temperature measurements with long wavelength cameras, to avoid the peak of reflection as shown in Figure 2-27, wavelengths below 8.1 μm

have to be privileged. Some QWIP cameras have been equipped with a low pass filter having such a cut-off wavelength (Figure 2-28). In this case, most glass materials have a normal (perpendicular) emissivity close to 0.98.
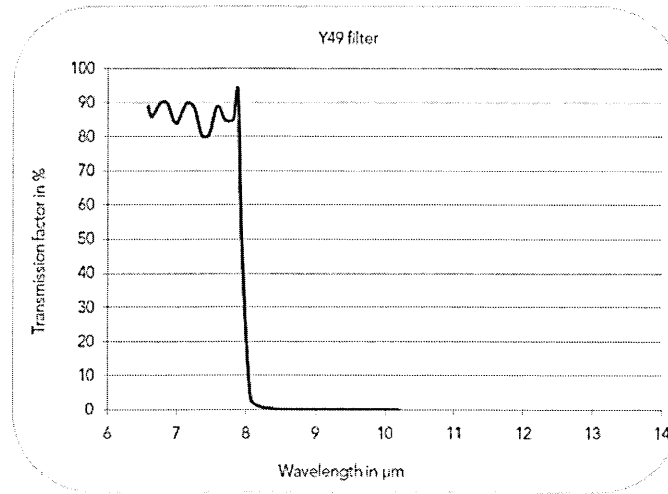
Figure 2-28 Low pass filter for long wavelength camera (FLIR AB 2012)

For glass surface temperature measurement without utilising a filter, the simplest solution is to use an uncooled detector long wavelength camera. It has the temperature range and has less temperature dependence from greybody approximation. The peak of reflection is of low influence, so long as the object is hotter than the surrounding environment. The emissivity for typical soda lime silica is 0.96, assuming an object temperature of 1000°C and a reflected apparent temperature of 400°C. Atmospheric perturbation along the optical path is neglected, therefore the transmittance of the atmosphere can be approximated to 1. The contribution from object emission can then be calculated as below:

$Contribution\ from\ object\ emission$

$$= \frac{object\ emissitvity\ \times\ object\ temperature}{(object\ emissivity\ \times object\ temperature) + (object\ reflectance\ \times ambient\ temperature)}$$

$$= \frac{0.96 \times\ 1000°C}{(0.96\ \times 1000°C) + (0.04 \times 400°C)}$$

$$= 0.998$$

From the calculation above, the emitted part represents more than 99 % of the total, which means that there should be no problem of metrology. Even if the

environment varies and is not correctly accounted for, it is of little importance on the reproducibility of the measurement.

For process monitoring and online quality control, the speed of the camera, that is the response time of the detector is often a more critical topic than radiometric considerations. Because microbolometer (un-cooled detector) cameras do not work like a photon detector, they are limited to applications where the object does not move with high speed. The response time of the camera will be investigate in more detail in the later chapter.

Chapter 3

Proposed System

During the glass forming process, a few degrees variation in the parison temperature can change the glass viscosity and affect the moulding process and the quality of the glass bottle. In an ideal condition, the parison should be maintained at a constant temperature at which good quality bottles are produced. However, in reality, the temperature can vary due to a number of factors such as the quality of the delivery system, the mould condition, the plunger condition, the ambient temperature, the mould cooling or the glass condition itself. Therefore, knowledge of the parison temperature is vital in the optimisation of the forming process to produce good quality glass containers.

Also, to be practical for production applications, the temperature measuring technique must not interfere with the process or disturb the product. Infrared thermography or thermal imaging is ideally suited for such demanding requirements. Long wavelength infrared cameras are non-contacting sensors that measure the surface temperature or some weighted average of the surface and internal temperatures of semi-transparent glass objects without affecting the product or its heat exchange with the environment. Together with a machine vision and image processing algorithm, the temperature measurement process can be automated and real time data can be logged and displayed on the user interface.

3.1 The proposed system

The proposed system is a machine vision based system to acquire and process images in real time to produce real time temperature data. The system utilises a high speed infrared camera with a microbolometer detector looking across the machine as shown in Figure 3-1.
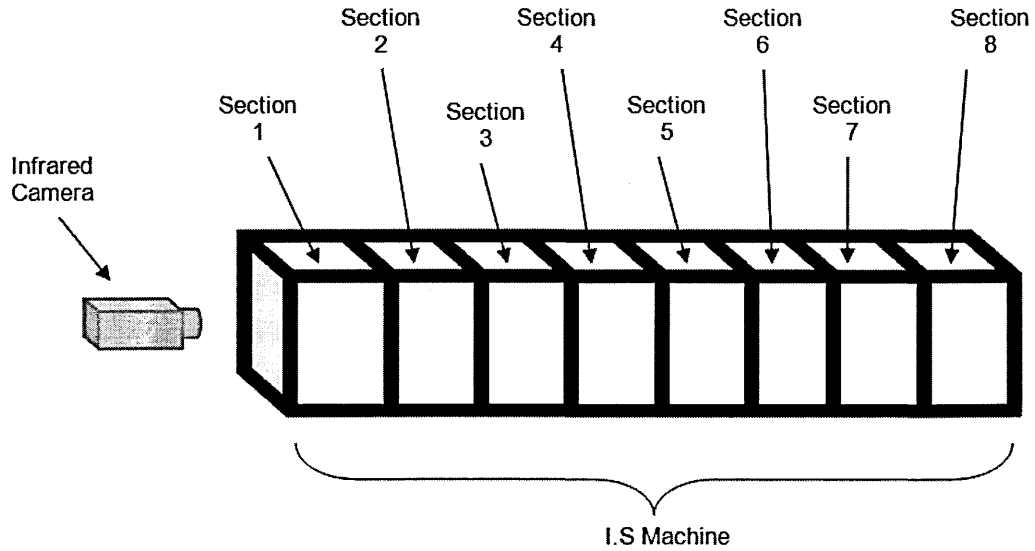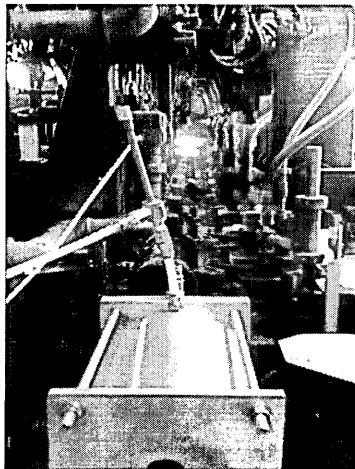

Figure 3-1 Proposed system

Figure 3-2 Front view of the I.S. machine

3.2 Overview of the system

```
        ┌─────────────────────┐
        │    Acquire image    │
        └─────────────────────┘
                   │
                   ▼
        ┌─────────────────────┐
        │     Select valid    │
        │    image for each   │
        │       Section       │
        └─────────────────────┘
                   │
                   ▼
        ┌─────────────────────┐
        │ Perform image processing │
        │ and temperature analysis │
        │     on valid image  │
        └─────────────────────┘
                   │
                   ▼
        ┌─────────────────────┐
        │  Display data on user │
        │       interface     │
        └─────────────────────┘
```
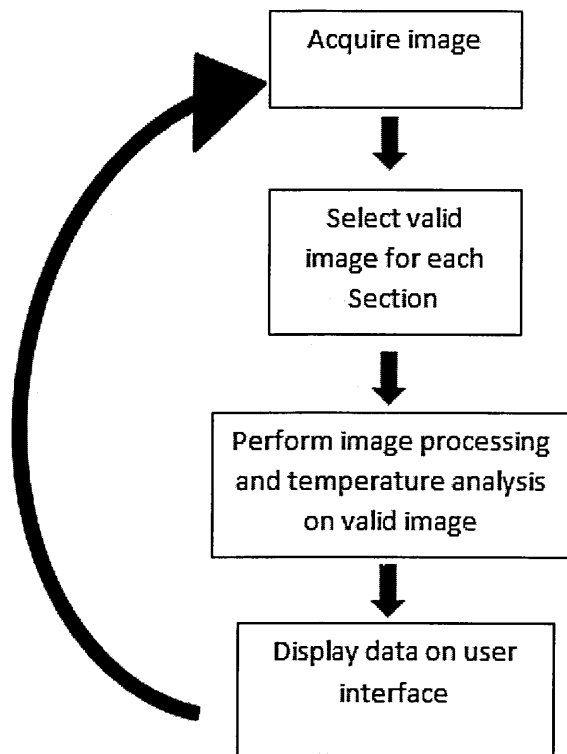
Figure 3-3 System overview

Each parison is inverted from the blank mould to the finish mould sequentially, the system automatically selects images that are clear of any obstruction from the invert arm mechanism or the I.S. machine structure itself. Generally, the unobstructed images are images when the parison is at the middle of the inversion from blank mould to the finish mould. These images are termed as "valid" images in this thesis.

Once an unobstructed image with clear view of the parison is selected, temperature analysis is performed on it to produce a temperature reading. This routine will be repeated continuously. The temperature data for each section of the I.S machine is displayed on the PC user interface allowing the operator to monitor the current parison's temperature. When the temperature data shown deviates from the pre-defined temperature range, the operator could either perform root cause analysis to the machine or make adjustments to the machine such as alterating of the cooling system to compensate for the temperature deviation.

3.3 Benefits of the system

Assumed data

- Most of the current solutions involve mould temperature measurement to infer the temperature of the parison. This leads to assumptions about the parison temperature, which can be inaccurate. The proposed system will measure the actual parison temperature in real time, minimising these inaccuracies.

Sampling speed

- The system will sample temperature data in real time and will provide feedback immediately to the operator to carry out adjustments to the machine to ensure optimum parison temperatures.

Health and Safety

- The existing system for mould temperature measurement is a manual process that can potentially put operators at risk of injuries. The system is automated, so there is no need for any operator intervention.

Chapter 4

Image Validation

4.1 Parison movement

As described in the literature review, a partly form container referred to as "parison" is formed when the gob is released from the blank mould. These parisons are inverted by an invert mechanism and transferred to another mould referred to as finish mould where these parisons will be blown into their final shape.

The infrared camera is placed at the side of the I.S machine and continuously acquires images for every section. Figure 4-1 shows a sequence of images from section 1 (section nearest to the camera).
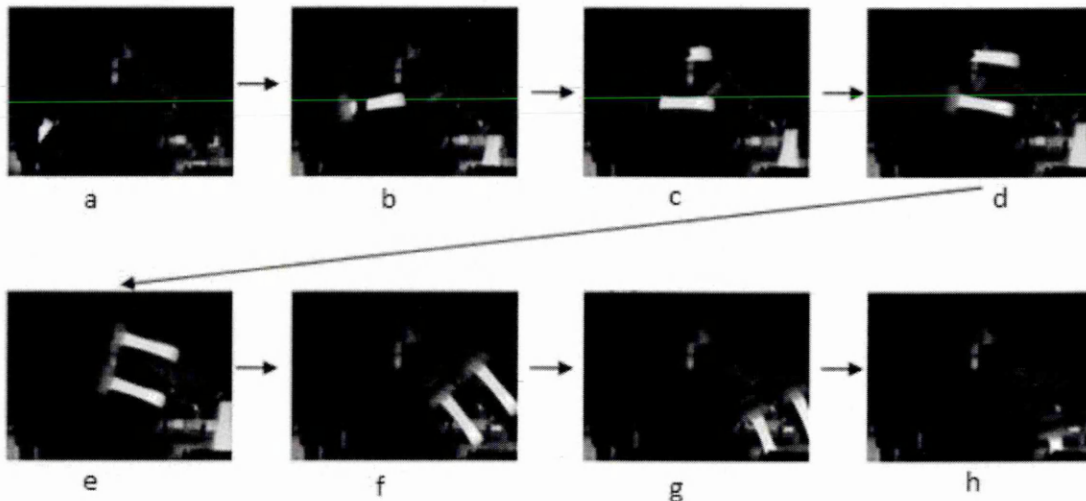
Figure 4-1 A sequence of images from section 1

In order to perform temperature analysis on the parisons, the images taken must have a clear view of the parison. That is, an image where the parison is not obstructed by the I.S. machine structure. From the sequence of images, a single image will be selected automatically with a machine vision algorithm, this valid image (image "e" from Figure 4-1) will be used for temperature analysis.

Generally, a valid image is usually where the parison is at the middle of the inversion process where parison would be approximately at the centre of the image. However, the image captured where the parison is at the middle of the image does not always guarantee an unobstructed view of the parison. This is because at the end of each forming cycle, the invert mechanism returns to its original position at the blank mould, whilst it is moving towards the blank mould, it could obstruct the view of the parison behind, as shown in Figure 4-2.
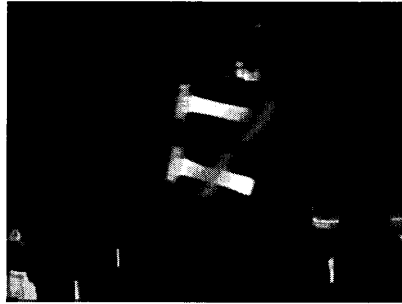
Figure 4-2 Invert Mechanism obstructing the view of the parison

A machine vision algorithm was developed to select the images where there is a clear parison in the view with no obstruction from the machine structure or its invert arm. Figures 4.3 and 4.4 show some of the valid images and invalid images respectively.
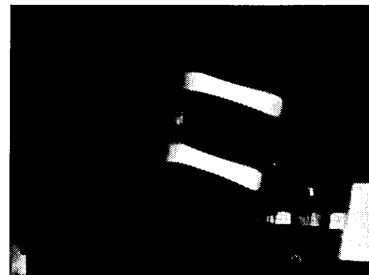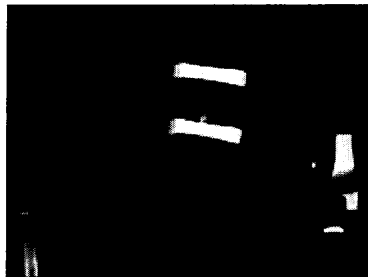

Figure 4-3 Valid images

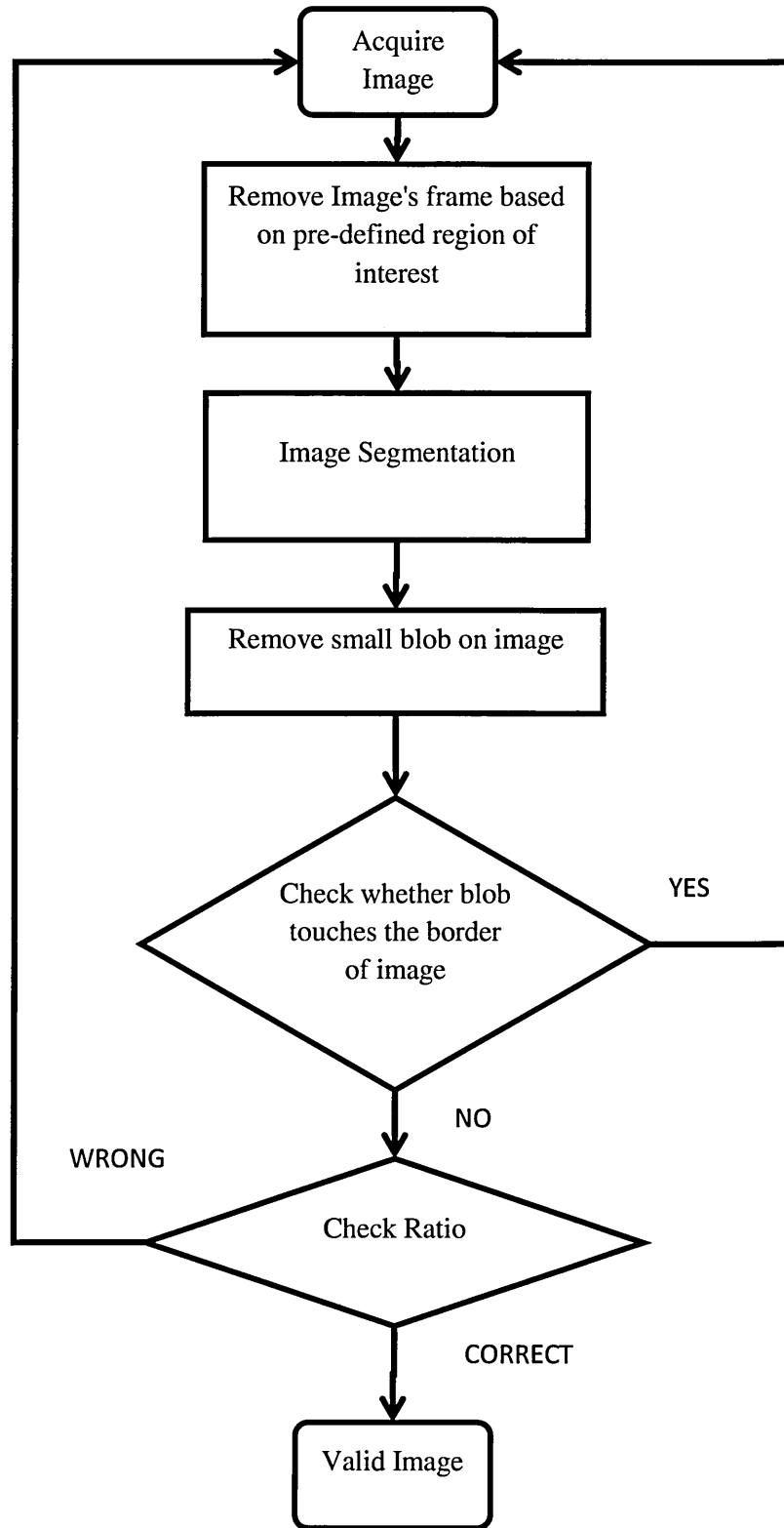Figure 4-4 Invalid images

46

4.2 The Algorithm

Figure 4-5 Flow-chart to select a valid image

The algorithm to detect valid images was designed to be efficient in order to maintain or achieve the frame rate of the camera which is 60Hz.This implies that the vision algorithm to determine a valid image must be executed in less than 16.67ms to avoid a decrease in the frame rate.

The algorithm begins by first defining a region of interest based on user input. This region will remove unwanted hot blobs on the image which are caused by the machine structure or component at border of the images. This defined region of interest will be the only region where the subsequent vision algorithm will be performed on. The image frame which is the region outside of the predefined area will be "cropped" or removed, effectively reducing the image size. This increases the execution speed of the remaining algorithm since it is dealing with fewer pixels.

The next step involves image segmentation, a basic image segmentation technique such as image thresholding could easily segment the background against object of interest since the object of interest, ie, the parison, has significantly larger pixel values compared to the background. The result after image thresholding will be a binary image with pixel value of 0 representing the background and 1 representing the object. Each blob in the image is then calculated for its area to determine whether it is indeed a parison or unwanted hot area from the machine component. Since these unwanted hot components are usually represented in the image as small blobs, the next step would be to remove these small blobs by comparing each blob in the image against a predefined size. The size refers to the total number of pixels contained in a particular blob. The small blob is removed by converting its pixel values to the background pixel value, i.e. 0.

Once the image has been converted into binary image, the next process is to check whether the remaining blobs (parisons) touch the border of the image. If the parison touches the border, the image will be rejected since this is the cropped image where the border was removed in the first stage described earlier. This will ensure that the chosen image will have a clear view of the parison and is unobstructed by the machine structure.

At this stage, the algorithm would be able to select an image which has a complete view of the parison. However, as stated earlier, if the parison is not

from the first section, there is a possibility that the invert arm that is travelling back to the blank mould position might obstruct the view of the parison. With the current algorithm, the image with invert arm obstructing the view of the parison might wrongly be interpreted as a valid image. To avoid this, a direct method to solve the problem is to calculate the size of the parison (number of pixels) and compare it against a predefined size to determine whether the image has been blocked or obstructed by the invert arm. An obstructed parison will have a smaller size compared to an unobstructed one. The limitation of this method is that it needs a predefined parison size for each section, different sections will have a different parison size due the perspective effect of the camera system with the object at different distances relative to the camera (objects appear smaller as distance increases).

In order to reduce the number of predefined input parameters required for the detection algorithm, the ratio of the parisons is used instead. The ratio is the vertical number of pixels divided by the horizontal number of pixels of the parison. Assuming that the camera lens and camera are distortion free and the actual parison size is exactly the same, then the ratio of the parison in the image would be the same for every section. Theoretically, a single pre-define ratio value could be used to determine whether a parison has been obstructed by an invert mechanism. However, in practice, a +/- tolerance of 10% from ratio should be used as each parison dimensions is slightly different and camera system and lens is not perfect. A parison that has a ratio which is outside of this range would be considered as an obstructed image and it would be rejected.

Once the images gone through all the stages of the algorithm, only the image which is not obstructed by the machine structure and its invert arm mechanism will be chosen as a valid image and used for temperature analysis.

Chapter 5

Effects of Object Distance

As discussed in Chapter 3, the camera is positioned at the side of the I.S. machine, parisons from different sections are at different distances relative to the camera (Figure 5-1).The distance between any two adjacent sections is 0.533m.   Due to the perspective effect of the camera system, the parisons further away from the camera will be perceived as being smaller, that is the number of pixels per unit area reduces as a function of the distance, which results in reduced temperature measurement accuracy (Madding, L.Orlove and Lyon 2006). Apart from a decrease in the number pixels or decrease in spatial resolution, the atmospheric absorption effect and the camera focus, both of which are also distance dependent, would contribute to the measurement error.
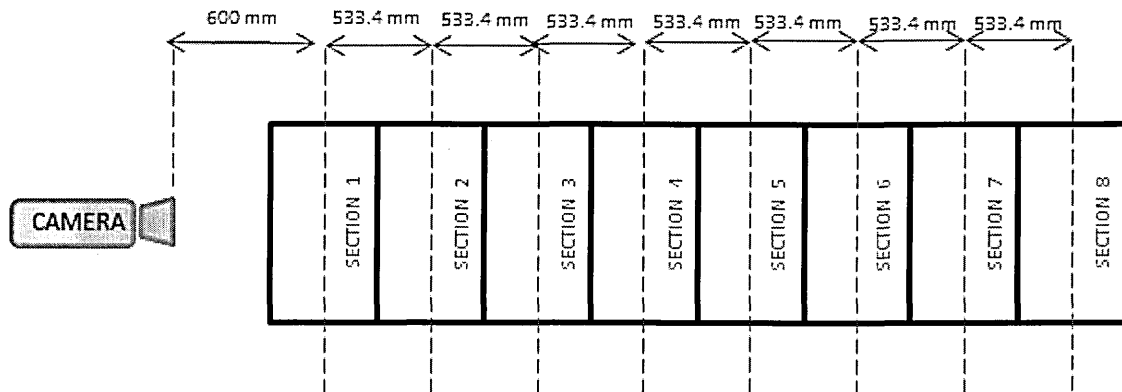
Figure 5-1 Camera position and I.S machine dimension

5.1 Atmospheric absorption

The atmosphere between the source of radiation and the detector causes perturbations in measurement. The emitted infrared energy is attenuated by the atmosphere (C.Holst 2000) and it is a particular problem in the course of a measurement, because it introduces an error that depends on the working wavelength, the spectral band used, the distance and the ambient temperature.

The spectral transmittance of the atmosphere in the IR region is a very complex function as shown Figure 5-2 below:

50

Figure 5-2 Atmospheric transmittance (L.Williams 2009)

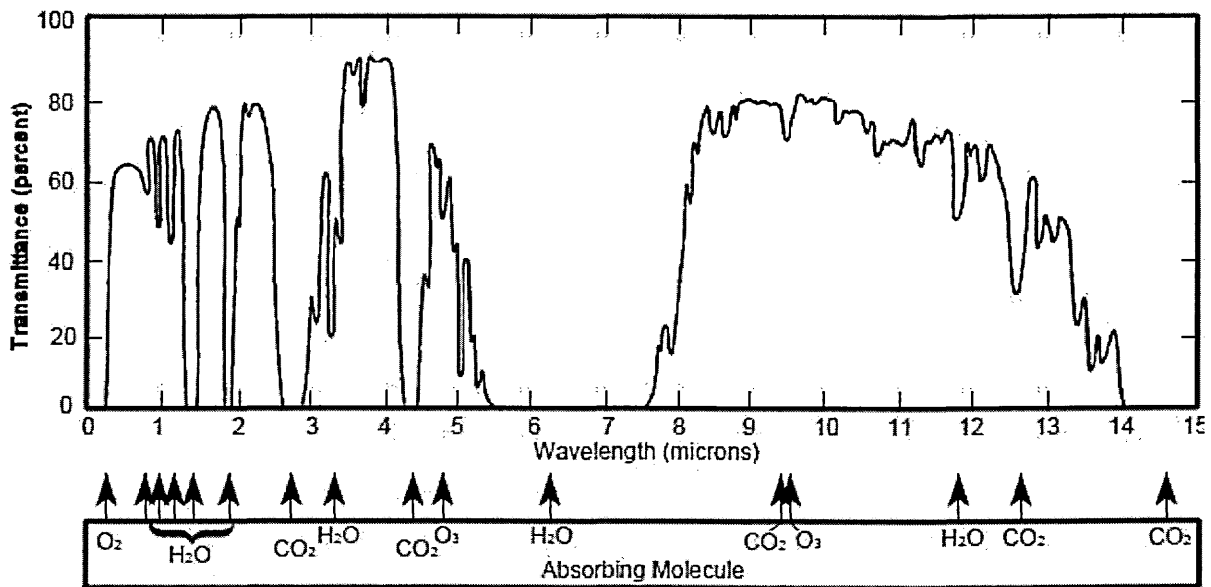The spectral transmittance depends very much on the length of the measurement path, but also on some gas constituents of the atmosphere, gases that have absorption bands in the infrared region. The most important of those are water vapour and carbon dioxide. From Figure 5-2, it can be seen that the co_2 absorption band at 4.2 - 4.4 μm, and the water absorption from about 4.8μm onwards, both effect the SW (short wavelength) spectrum. Usually, for temperature measurement, the percentage of carbon dioxide is rather constant while the amount of water vapour varies significantly with temperature and relative humidity of the atmosphere (L.Williams 2009). It is important that the camera does not operate at wavelengths where there is an absorption band. If no correction for attenuation is applied, the measured apparent temperature will be lower with increased distance.

Infrared cameras are usually designed to operate at in what is known as atmospheric windows, where transmission is very high. As can be seen from Figure 5-2, they can be found between 2 and 5μm, the (MW) mid-wave window, and 7.5–13.5μm, the (LW) long-wave window. Typically, LW cameras in the 7.5–13.5μm range work well because the atmosphere tends to act as a high-pass filter above 7.5μm. The MW band of 3–5μm tends to be employed with highly sensitive detectors for high-end R&D and military applications. When acquiring a signal through the atmosphere with MW cameras, selected transmission bands must be used where less attenuation takes place (FLIR AB

2012). It is common for IR cameras to have a filter in front of the detector to ensure the spectral response is matched to an Infrared Windows.

Since the atmosphere contains many different particles and behaves in a dynamic way, it is not very easy to predict the extinction coefficient and transmittance. An accurate atmospheric transmission calculation requires that all molecular, aerosol, and precipitation effects be taken into account. When exact results are required, a detailed model must be used. In infrared technology, computer models such as the LOWTRAN, MODTRAN, FASCODE and the SEARAD Radiance are used to compute the extinction coefficient and transmittance (Yildirim 2000).

With a FLIR camera, the atmospheric attenuation can be compensated for by built-in atmospheric models that compute the atmospheric transmission as a function of object distance, relative humidity and atmospheric temperature.
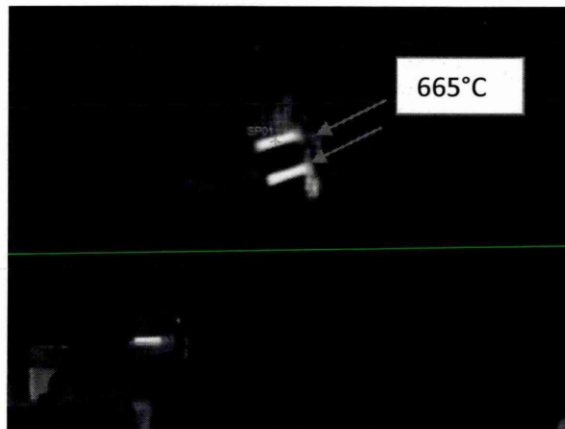

Figure 5-3 Uncompensated image

Figure 5-4 Compensated image

Figure 5-3 and 5-4 shows the uncompensated and compensated image for atmospheric attenuation. Both images are the same and taken from the last section, i.e. section furthest away from the camera. Compensation was performed using the built-in model of the FLIR camera. It can be seen that a temperature increase of 6^0C occurs when the image is compensated. This means that an increase of approximately 0.8^0C per section can be accounted for. In order to reduce the inaccuracy due to the atmospheric absorption, this offset values are applied accordingly to the temperature data.

5.2 Focus distance

As with visual photography, a good focus will bring out the images details, when the image is out of focus, an object will become blurred. This is true for thermal images as well, even more importantly, an infrared thermal image that is out of focus will display incorrect temperature data.

Figure 5-5 Incorrect temperature reading due to out of focus effect

Parisons from different sections will have different distances from the camera, producing a measurement error due to "out of focus" effect. The measurement error can be reduced by increasing the depth of field of the camera system. Depth of field (DoF) is an optical property of lenses which means that only objects within a certain distance range from the camera will be in focus, as shown in Figures 5-6 and 5-7. For images such as landscapes, a large depth of field is usually desirable, however for portraits, a very shallow depth of field is often preferred to make the subject stand out against an out-of-focus background (Cambridge in Colour 2012).
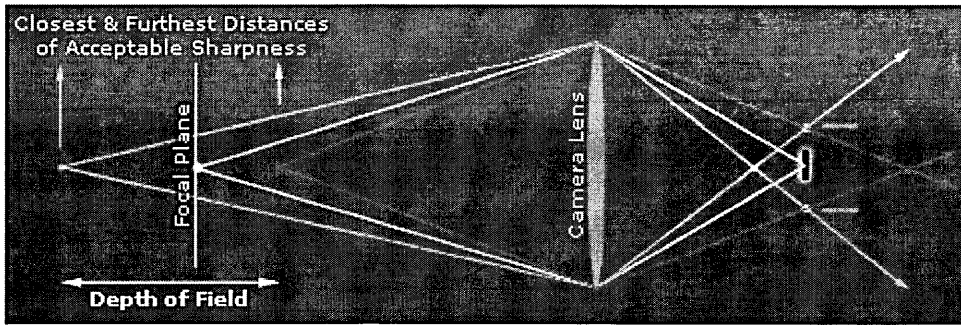
Figure 5-6 Depth of field (Cambridge in Colour 2012)
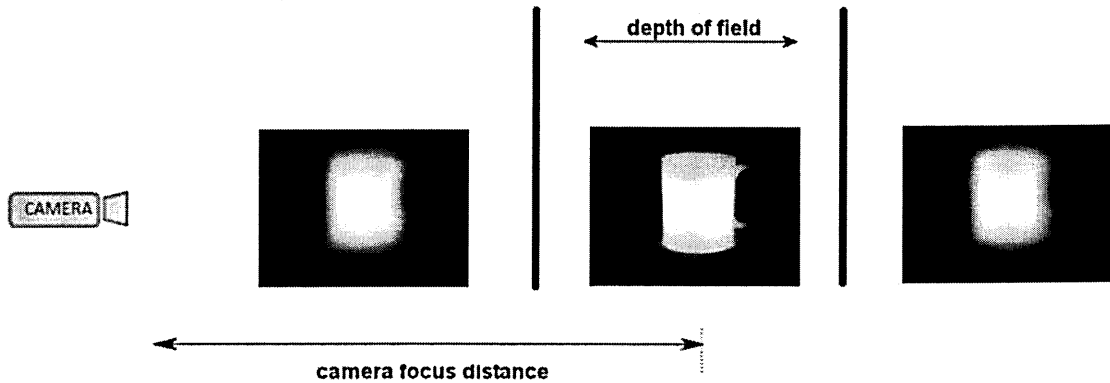
Figure 5-7 Depth of field effect

The depth of field can be controlled by either changing the aperture of the lens or the focus distance of the camera.

5.2.1 The aperture of the lens and the focal length of the lens

As a general rule, at any given focal length the smaller the aperture the greater the depth of field. Larger apertures correspond with smaller f-numbers, such as f/2.8 and f/4, while smaller apertures correspond with larger numbers. An aperture of f/4 will provide a substantially shallower depth of field than an aperture of f/16, providing all other conditions remain the same.

5.2.2 The focus distance

In general, focussing further into the distance results in greater depth of field than focussing close-up. However, as the focus point moves further away, the ratios of acceptable focus in front of and behind the subject also change. Whereas the two are roughly equal when shooting close up, as the point of focus moves further into the distance, depth of field increases behind the subject to a greater degree than it does in front of it.

For a FLIR camera, the aperture and the focal length of the lens is non-adjustable, therefore the only option to increase the DoF is to adjust the focus distance of the camera. To achieve the maximum DoF, the camera's focus distance is set to a hyperfocal distance, which is the distance beyond which all objects can be brought into an "acceptable" focus. The hyperfocal distance for this particular camera is 20.55m with a near focus of 25cm to maximum focus of infinity (Murray 2012). Thus, the camera focus is fixed to this particular setting to minimize the measurement error due to "out of focus" effect.

5.3 Spatial resolution

Spatial resolution is usually specified as an angle (in milliRadians or mRad) referred to as Instantaneous Field of View (IFOV).

IFOV could be described from the Field of View (FOV) of the camera. The FOV of the camera depends on the camera lens and focal plane dimensions, and is expressed in degrees, such as 35.5° × 28.7° or 18.2 × 14.6°. For a given viewing distance, this determines the dimensions of the total surface area "seen" by the camera (Figure 5-8).
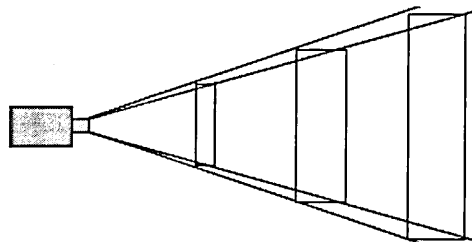
Figure 5-8 FOV of a camera

When FOV dimension is divided by the number of pixels in a line and row respectively, then it is equivalent to a pixel's IFOV as shown in Figure 5-9:
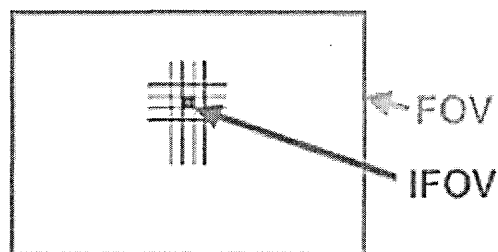

Figure 5-9 FOV and IFOV (FLIR AB 2012)

Generally, the smaller the IFOV figure, then the better the camera is for a given total field of view. It is clear that the distance factor in this relationship becomes very important when determining if a camera will resolve the image of a small object at a relatively large distance. Figure 5-10 illustrates this point, in the left view of Figure 5-10, the area of the object to be measured covers the IFOV completely. Therefore, the pixel will receive radiation only from the object, and its temperature can be measured correctly. In the right view of Figure 5-10, the pixel covers more than the target object area and will pick up radiation from extraneous objects. If the object is hotter than the objects beside or behind it, the temperature reading will be too low, and vice versa. Therefore, it is important to estimate the size of the target object compared to the IFOV in each measurement situation.
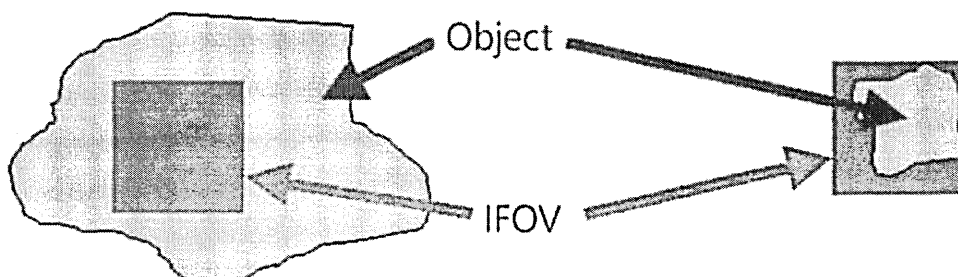

Figure 5-10 Object and IFOV (FLIR AB 2012)

IFOV describes the resolution and not the accuracy. The IFOV capabilities of an infrared camera may well find a small hot or cold spot but not necessarily measure its temperature accurately (Hockings 2001). It is only a geometric

value calculated from the focal length of the optics, the system resolution is additionally influenced by the diffraction of the optics. The image of the object is affected by the optical diffraction and aberration blur and by the bandwidth of the detector and electronics. Therefore, the image of the small object must be much larger than the detector, in order not to affect the measurement (Vollmer and Mollmann 2010).

The accuracy of the measurement is described by the Slit Response Function (SRF). This is defined as a normalised dependence of the system response to a slit size object with a variable slit width. Figure 5-11 shows a typical test configuration adapted from (Möllmann et al. 2006). The IFOV calculated is 1.1mrad and the θ is the observable slit angle at the given slit width seen from the detector.
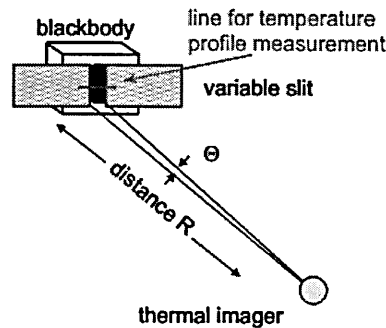
Figure 5-11 Test configurations to obtain the SRF and the temperature output for different object sizes (Möllmann et al. 2006)

The blackbody temperature should be high enough (70 -90 degree Celsius) to give a noise free video signal of high contrast. The signal (temperature) from a selected scan line across the slit is studied as the slit is varied from large width (30mm) to small width (1mm). With decreasing object size, i.e. slit width, the peak output becomes smaller as shown in Figure 5-12.
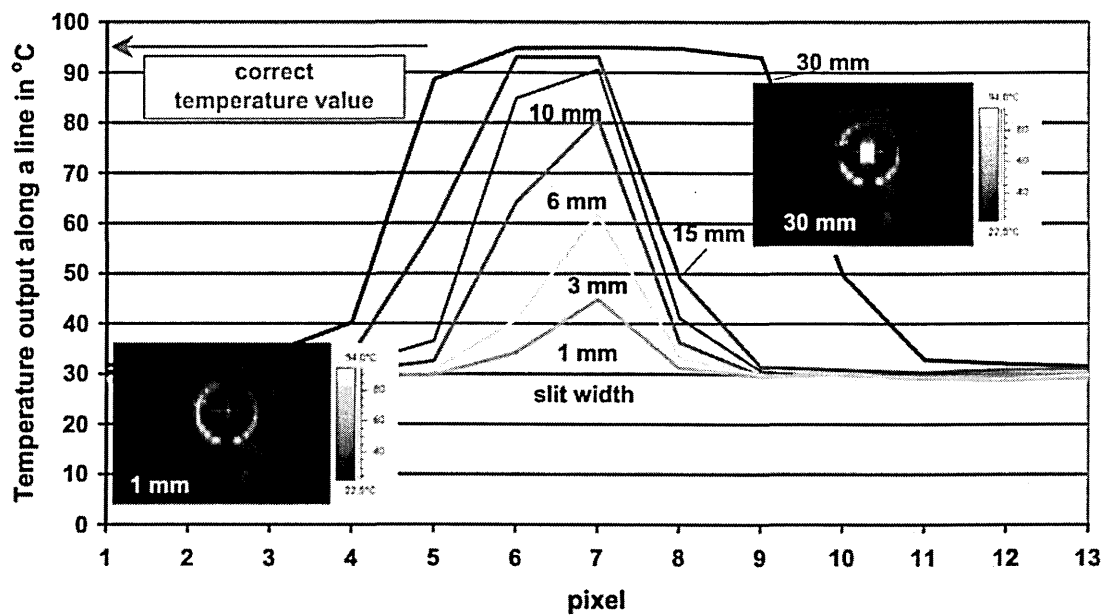
Figure 5-12 Measured temperature of the object viewed through a slit with variable width along a line (Möllmann et al. 2006)

The SRF graph (Figure 5-13 and Figure 5-14) represents a function of the measured object signal at a defined slit width normalised to that measured with a very wide slit(correct object signal of the slit size target). The signal from the very wide slit, is defined as 100% modulation or modulation = 1. At the narrower slit width, the pulse height starts to decrease (m<1) down to zero for zero slit width. From the peak output for each slit width, the SRF can be calculated and plotted such as the Graph in Figure 5-13. This function provides both the imaging and the measurement resolution. Figure 5-13 shows the SRF for temperature versus slit angle and Figure 5-14 shows the SRF which has been normalised to show signal modulation versus slit angle.
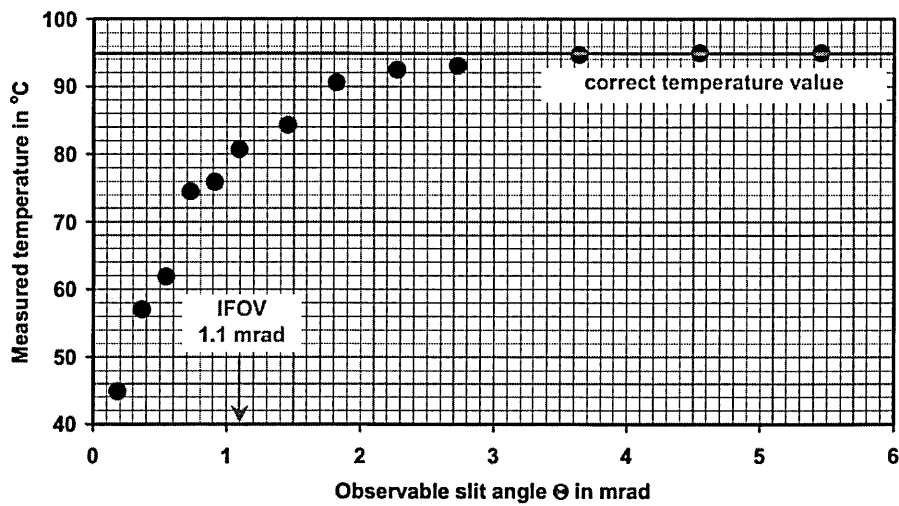
Figure 5-13 Measured peak output at different slit widths (Möllmann et al. 2006)
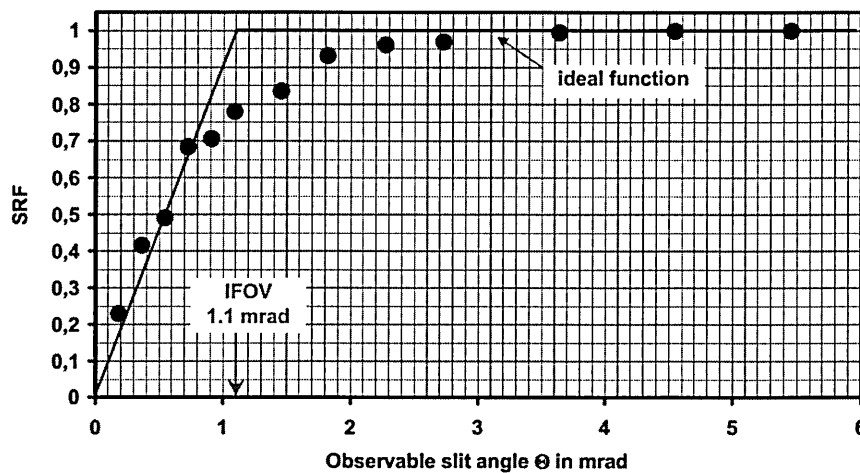
Figure 5-14 Measured modulation signal at different slit widths (Möllmann et al. 2006)

The imaging resolution is usually defined as that angular width of the object seen from the camera that gives a 50% modulation. But for accurate temperature measurement, it should be twice or three-fold the IFOV to reach 95% or 99% modulation, respectively. From these results, the minimum necessary object size for accurate temperature measurements can easily be calculated using the formula for the actual measurement distance, multiplying the object size by a factor of two or three (Möllmann et al. 2006).

The Slit Response Function could potentially be used to compensate for the difference in object distance for a constant temperature object (uniformly distributed temperature intensity). However, the object of interest discussed in

this thesis (i.e. the parison) does not have an uniform temperature distribution. The Slit Response Function is difficult to be modelled according to the method just discussed.

In order to investigate the effect of the spatial resolution on a parison's temperature reading, a metal plate cut to the dimension of a real parison is heated by a heating element to replicate the actual parison's temperature distribution as closely as possible. Other variables, such as the focus position and atmospheric absorption that could affect the signal at different distances were compensated in order to investigate solely the effect of spatial resolution on the signal received.

The temperature was taken at different positions according to the same distance as an I.S. machine by moving the camera position. At each distance, the focus is re-adjusted and atmospheric absorption is compensated for to eliminate the error contribution of these two factors. The test was taken a several times and the results were averaged. The results are shown below.
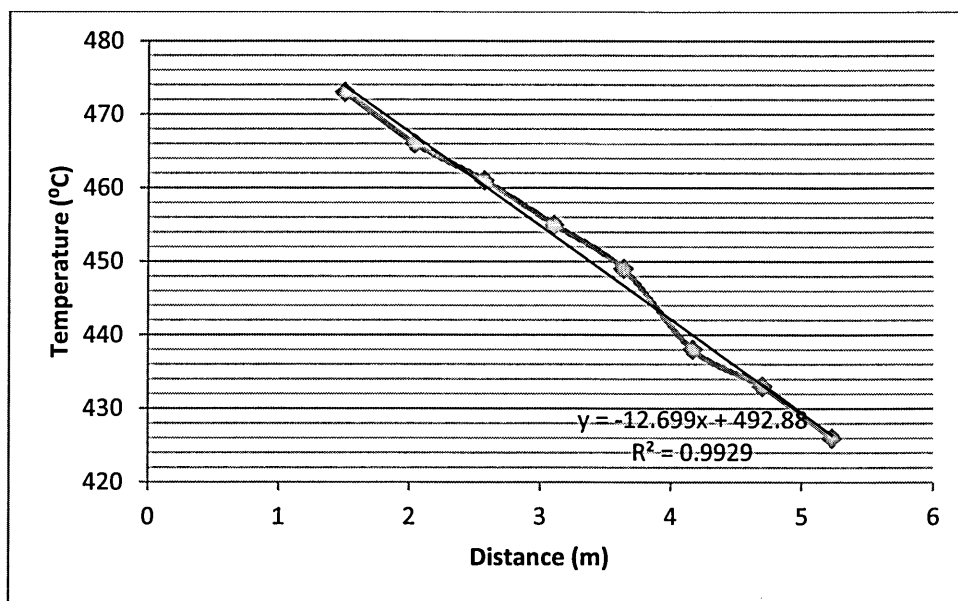
Figure 5-15 Temperature reading as a function of distance

It can be seen from the experiment results, that there is a near linear temperature drop as the distance increases. At the furthest section at a distance of 5.2338m, there is a 9.9% drop in temperature relative to the temperature reading from the nearest distance. Table 5-1 below shows the temperature drop in percentage at each distance.

Distance(m)	Temperature drop (%)
1.5	0
2.0334	1.5
2.5668	2.5
3.1002	3.8
3.6336	5.1
4.167	7.4
4.7004	8.5
5.2338	9.9

Table 5-1 Percentage of temperature drop with distance

The experiment was repeated using a different lens, instead of a 25^0 standard lens, a 15^0 telephoto lens was used. The results are shown below:

Figure 5-16 Temperature reading with a telephoto lens

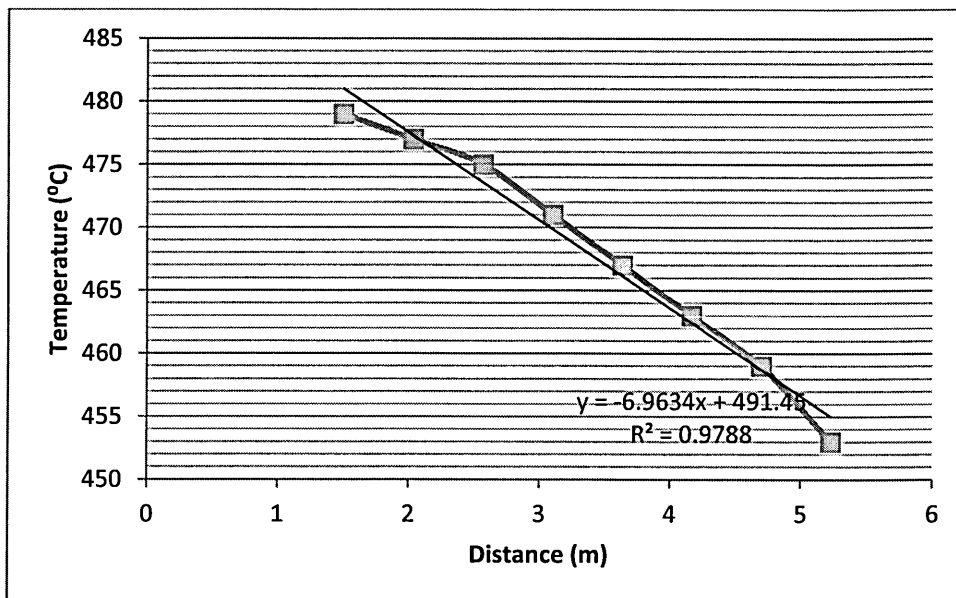| Distance(m)	Temperature drop(%)
1.5	0
2.0334	0.4
2.5668	0.8
3.1002	1.7
3.6336	2.5
4.167	3.3
4.7004	4.2
5.2338	5.4

Table 5-2 Temperature drop with a telephoto lens

As shown in Figure 5-16, the temperature drops linearly as the distance increases. However, the drop in temperature is less drastic compared to a standard lens configuration, as shown in Table 5-1. Fitting the data with a linear fit by least square method, the slope for the linear fit function is -12.7 and -6.96 for a standard lens and telephoto lens configuration, respectively.

These results show the effects of spatial resolution on the temperature data. The object temperature reduces as the number of pixels representing the object reduces. With a telephoto lens, the drop in temperature is less severe compared to a standard lens configuration. The drop in temperature for a short distance (i.e. 1.5m to 5.2 m) can be approximated to be a linear temperature drop, as shown from the data from both the telephoto and the standard lens system. When the system is deployed for real temperature measurement in the factory, it is expected that there would be a similar behaviour where the linear temperature drops across the machine's sections due to the effect of spatial resolution.

Chapter 6

Image Blurring

As the parison is being transferred from the blank mould to the finish mould, the inner parison re-heat its surface causing the viscosity to decrease. Therefore, parisons are inverted at a high speed by the I.S. machine's invert arm so that their viscosity does not decrease to the state of causing defects or even loss of shape while the parisons are being inverted. Due to the speed of the parison movement, blurring artefact may be seen on the IR image. This happens because the camera's detector response time is not fast enough relative to the speed of the motion. A parison moving with respect to the camera will look blurred or smeared along the direction of relative motion.

Figure 6-1 Blurred parisons

As discussed in the literature review, infrared detectors can be classified into photon/quantum detectors and thermal detectors. Photon detectors are fast compared to thermal detectors. The next section discusses the basic principle of thermal detection and photon detector in order to understand why thermal detectors are slower.

6.1 Photon detectors versus bolometer cameras

Most of the IR cameras in the consumer market are equipped with microbolometer FPA's which are thermal detectors. These thermal imagers

meet the demands of most practical applications and are much less expensive than photon detector FPA cameras. Microbolometers are characterised by relatively low sensitivities/detectivities, broad/flat spectral response curves and slow response times of the order of 10 milliseconds.

For more demanding applications requiring higher sensitivity and time resolutions such as in R&D, photon detector FPA cameras are preferable. For the MW and the LW spectral regions, FPA cameras are cooled down to liquid nitrogen temperature. For the SW region, the detectors are cooled by multistage Peltier elements. Photon detector offer time constants down to about 1 μs. Therefore, photon detector cameras offer much higher frame rates than microbolometer cameras.

In photon detectors, a single-step transduction leads to changes of concentration or mobility of the free charge carriers in the detector element upon absorption of photons from the infrared radiation. If the incident radiation generates charge carriers, the electrical resistance of the detector element is changed. The direct conversion of the photon flux into an electrical signal (photocurrent) and the small time constants allow for a very fast camera operation .

Thermal detectors can be treated as two-step transducers. First, the incident radiation is absorbed to change the temperature of a material. Second, the electrical output of the thermal sensor is produced by a respective change in some physical property of a material. In the case of a microbolometer, electrical resistance will change depending on the temperature of the microbolometer (Vollmer and Mollmann 2010).

Because of their operation as thermal detectors, microbolometers do not offer the possibility to change the integration time. Rather, the integration time is given by the thermal time constant of the microbolometer detectors. Unlike a rolling shutter camera, they have no integration time adjustment. A microbolometer detector is constantly open to incoming radiation and responds to changes with the time constant. The pixels in the camera register integrated signal via their temperature (get hotter when more signals arrive, and cooler when less signal arrives).

Because the integration of the signal is a physical rather than an electronic mechanism, such in the case of a typical rolling shutter camera, in a microbolometer camera there is no way to reset the integrated signal from an earlier frame. As a result, a microbolometer pixel will have memory of the signal that was collected in previous frames. Due to the pixel's cooling mechanism, the contribution from past frames decays over time. The heating and cooling occur at a rate that is defined by the pixel's time constant. Image artefacts such as tails on hot moving objects are a result of this property of the camera (FLIR Cores and Components 2012).
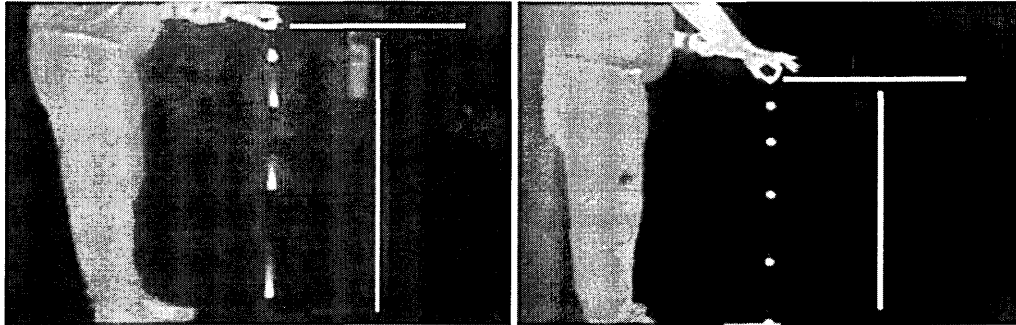

Figure 6-2 Images taken from a photon camera (right) and a thermal camera (left) (Vollmer and Mollmann 2010)

Figure 6-2 (Vollmer and Mollmann 2010) shows the effect of the response time for both a microbolometer camera (FLIR SC2000) and a photon camera (FLIR SC6000). As stated previously, bolometer cameras do not offer the possibility of a selectable integration or exposure time in contrast to a photon detector. With increasing velocity of the ball during the free fall motion, the FLIR SC2000 image of the ball becomes blurred due to the increasing speed of the ball.

For InSb photon detectors of the FLIR SC6000, the detector time constants are much lower and, therefore, these detectors respond much faster. For the FLIR SC6000, an integration time of 1 ms was used. No blurring of the image of the ball is observed and the temperature of the ball can be correctly determined over the whole falling distance as opposed to a microbolometer camera where the infrared image will not reflect the real spatial temperature distribution.

6.2 Image blurring

Image blurring occurs in a variety of situations such as imperfections in optical systems, atmospheric interference, and movement of camera/object. The blurring of images can be modelled as in Figure 6-3 as the convolution of an ideal image with a 2-D point-spread function (PSF). The interpretation of Figure 6-3 is that if the ideal image $f(x, y)$ consisted of a single intensity point or point source, this point would be recorded as a spread-out intensity pattern, hence the name point-spread function.
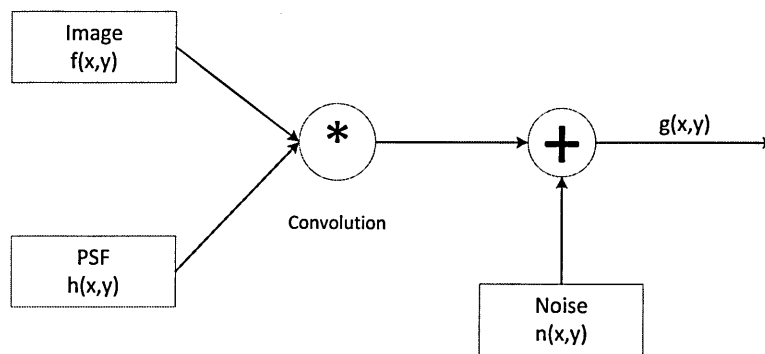

Figure 6-3 Graphical representation of image blurring model

It is assumed that this blurring function acts as a convolution kernel or point-spread function $h(x, y)$ that does not vary spatially. It is also assumed that the statistical properties of the image and noise do not change spatially. Under these conditions, the restoration process can be carried out by means of a linear filter. These modelling assumptions can be mathematically formulated as follows. If $f(x, y)$ is the desired ideal spatially discrete image that does not contain any blurring or noise, then the recorded image $g(x, y)$ is modelled as:

$$g(x, y) = h(x, y) * f(x, y) + n(x, y) \qquad (6.1)$$

$n(x, y)$ is the noise that is added to the blurred image. The objective of image restoration is to make an estimate $\hat{f}(x, y)$ of the ideal image $f(x, y)$, given only the degraded image $g(x, y)$, the blurring function $h(x, y)$ and some information about the statistical properties of the ideal image and the noise.
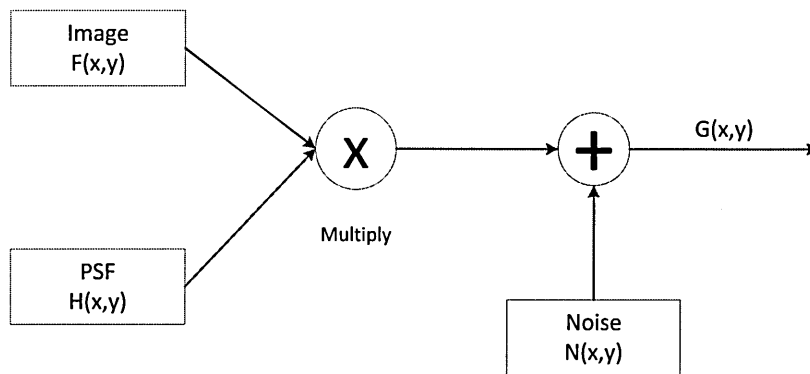
66

Figure 6-4 Graphical representation of image blur model in spectral domain

An alternative way of describing (6.1) is through its spectral equivalence. By applying the discrete Fourier transform to the Equation (6.1):

$$G(u, v) = F(u, v) \cdot H(u, v) + N(u, v) \qquad (6.2)$$

where (u, v) are the spatial frequency coordinates, and G,F,H,N represent the Fourier transforms of the corresponding functions in the spatial domain. Both spatial and frequency domains can be used to develop restoration algorithms. In practice, the spectral representation is more often used since it leads to efficient implementations of restoration filters in the (discrete) Fourier domain.

The Fourier transform provides a very useful mathematical tool that transforms convolution in time/space domain to multiplication in the frequency domain.

6.3 Point-spread function

When an image is captured by a camera, it is projected from the object space to the image plane. In the ideal case, one point in the object plane projects into one point in the image-plane but this is often not the case. Instead, one point in the object plane spreads out over several points in the image plane. This is because each point in the object scene is blurred by a number of phenomena, before finally being projected onto the image plane. How the point is spread over the image plane is described by the PSF (point spread function). Figure 6-5 illustrates a basic PSF; points are spread out according to a Gaussian function.
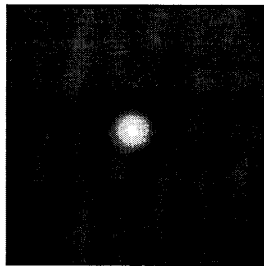
Figure 6-5 PSF caused by atmospheric effects

This particular PSF is caused by the atmospheric effects, i.e. temperature differences or turbulence in the air. Temperature differences lead to the light passing through volumes of air with different refractive index thus deviating it from its path. However, such effects are not considered in this report as this effect would not significantly influence the temperature reading.

Another type of PSF is shown in Figure 6-6. If the camera is not held still during exposure, a given point in the scene. Object is swept over several points in the image plane resulting in the blurring of the point. A similar effect arises when an object in the scene being captured is moving; the points of that particular object are blurred. Figure 6-6 illustrates the PSF corresponding to a linear sweeping horizontal motion.
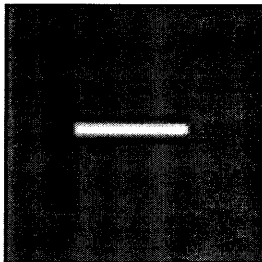

Figure 6-6 PSF caused by horizontal motion blur

6.3 Shift Variant Blurring and Shift Invariant

There are two types of image blurring, shift-variant and shift-invariant. The main difference between the two lies in how the blurring affects different parts of the image. The latter affects the whole image in the same way whereas the former affects different parts of the image in different ways.

Figure 6-7 shows an example of an image blurred by a shift-variant rotation. Another example of shift variant blurring (Figure 6-8) is when an object (hand) is moving at high speed causing blurring on the image while the background stays still.
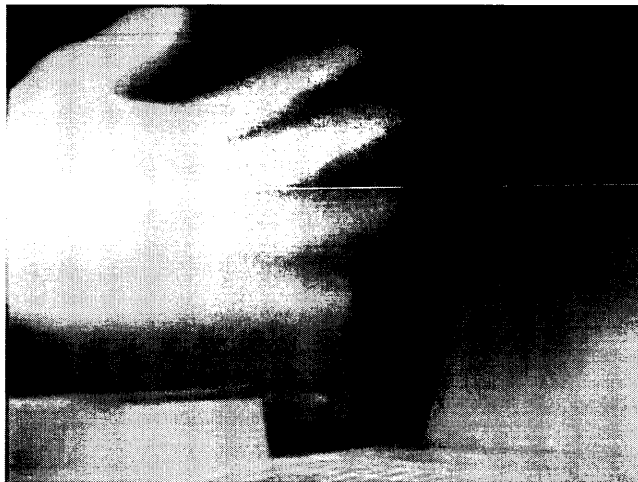

Figure 6-7 Rotational blur

Figure 6-8 Static(un-blurred) background and blurred object

As for shift invariant blurring, the blurring effect is present uniformly on the whole image. A camera that is moving at a constant speed taking a picture of a static object would induce a shift invariant blur. Figure 8-9 shows such an example, where the whole view is blurred. In this example though, the whole image would be blurred the same way, by the same sideways motion.
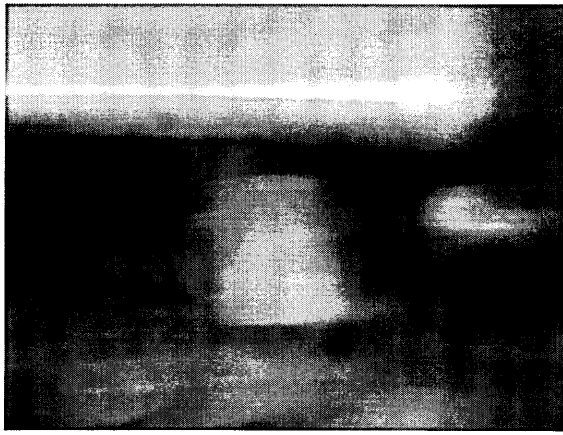
Figure 8-9 Horizontal motion blurring

The restoration of a shift-invariant blur can be achieved with inverse methods such as the Wiener filter. In some cases of shift-variant blurring, for instance rotational blurring, the direct inverse methods can be used by performing a transformation of the image to polar coordinates. In polar coordinates, rotation blurring can be seen as shift-invariant, thus the direct inverse methods can be applied (Kang 2011). This method will be discussed in more details later in the chapter.

According to (Gonzalez and Woods 2008), there are three principal ways to estimate the degradation function/PSF for the purpose of image restoration:

Estimation by Image Observation

The idea here is to look at the small rectangular section of the image containing sample structures, this sub-image usually has high signal content ,i.e. areas with high contrast. Then, the next step would be to process the sub image to arrive at a result that is as un-blurred as possible. Once the sub-image is un-blurred, the blurring function can be constructed to a larger scale with the same basic shape to deblur the full image.

Estimation by Experimentation

If equipment similar to the equipment used to acquire the degraded image is available, it is possible to obtain an accurate estimate of the degradation. Images similar to the degraded image can be acquired with various system settings until they are degraded as closely as possible to the image we wish to

restore. Then, the idea is to obtain the impulse response of the degradation by imaging an impulse using the same system settings.

Estimation by modelling

In some cases, the PSF can be described analytically and thus the PSF can be constructed from a function, rather than from an experiment. In this thesis, this approach was used to derive the PSF to represent the blurring function of a microbolometer. In order to derive the mathematical model to describe the blurring function, it is important to understand the fundamental operation of a microbolometer which will be discussed in the following section.

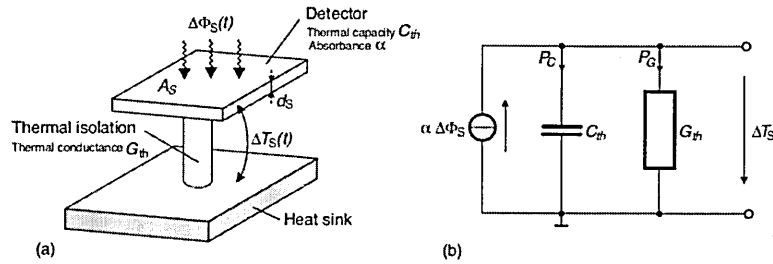## 6.5 Thermal Models of a Microbolometer

Figure 8-10 Model of a microbolometer sensor (Vollmer and Mollmann 2010)

Calculating the temperature change ΔT_s of the detector element due to the absorption of a radiant flux $\Delta \Phi_s$ is the key problem of the theoretical analysis and simulation of thermal sensors. In this thesis, this is used to derive the PSF required for image restoration.

The heat energy Q of the incident radiant flux $\Delta \Phi_s$ heats the sensor element with its heat capacitance C_{th}. Here a cuboid detector element (thin chip) with area A_s and thickness d_s has the heat capacitance

$$C_{th} = \acute{c}_s \rho_s A_s d_s \qquad (6.3)$$

71

with specific heat capacity $\acute{c}_S$ and mass density ρ_S. At the same time, heat energy is dissipated via several heat conduction mechanisms to the environment. The heat conduction to the surroundings can be represented as a thermal resistance R_{th} or thermal conductance $G_{th} = \frac{1}{R_{th}}$. The energy balance or power balance thus results in

$$\alpha \Delta \Phi_S(t) = P_c(t) + P_G(t) \tag{6.4}$$

with power flow P_c through the heat capacitance of the sensor element and power flow P_G through the thermal resistances to the thermal ground. With $P_c = \frac{dQ_c}{dt}$, it follows for the time domain that

$$\alpha \Delta \Phi_S(t) = C_{th} \frac{d[\Delta T_S(t)]}{dt} + G_{th} \Delta T_S(t) \tag{6.5}$$

Modulating the amplitude of the radiant flux with a chopper, it results in a periodic time function of the radiant flux. This periodic time functions can be mathematically expressed by sinusoidal processes, such as Fourier series. Harmonic analysis lends itself particularly well to this calculation, equation below shows the frequency domain representation.

$$\alpha \underline{\Delta \Phi_S} = (j\omega C_{th} + G_{th}) \underline{\Delta T_S} \tag{6.6}$$

In the frequency or image domain, respectively, the Laplace transform can be used to simply express any time function by complex frequencies $s = \sigma + j\omega$.

$$\alpha \underline{\Delta \Phi_S} = (\underline{s} C_{th} + G_{th}) \underline{\Delta T_S} \tag{6.7}$$

For a harmonic excitation, radiant flux $\Delta \Phi(t)$ has a sinusoidal time function with modulation or chopper frequency $\omega_{Ch} = 2\pi f_{Ch}$ and amplitude $\Delta \hat{\Phi}_S$:

$$\Delta \Phi_S(t) = \Delta \hat{\Phi}_S \cos \omega_{Ch} t \tag{6.8}$$

It then applies in the frequency domain that

$$\underline{\Delta \Phi_S}(\omega_{Ch}) = \Delta \Phi_S e^{j\omega_{Ch} t} \tag{6.9}$$

with effective value

$$\Delta \Phi_S = \frac{\Delta \hat{\Phi}_S}{\sqrt{2}} \tag{6.10}$$

The network model equation becomes:

$$\alpha \Delta \Phi_S(\omega_{Ch}) = (j\omega_{Ch}C_{th} + G_{th})\Delta T_s(\omega_{Ch}) \qquad (6.11)$$

Rearranging the equation above will show the temperature change in the detector element :

$$\Delta T_s(\omega_{Ch}) = \frac{\alpha \Delta \Phi_S}{G_{th}} \frac{1}{1+j\omega_{Ch}\tau_{th}} \qquad (6.12)$$

with thermal time constant

$$\tau_{th} = \frac{C_{th}}{G_{th}} \qquad (6.13)$$

Only the effective value of the temperature change, that is the absolute value, is of interest:

$$\left| \Delta T_s(\omega_{Ch}) \right| = \Delta T_s(\omega_{Ch}) = \frac{\alpha \Delta \Phi_S}{G_{th}} \frac{1}{\sqrt{1+j\omega^2_{Ch}\tau^2_{th}}} \qquad (6.14)$$

That means that a detector element behaves like a first-order low-pass filter. It applies to un-modulated radiant flux, that is $\omega_{Ch} = 0$ that:

$$\Delta T_s(\omega_{Ch} = 0) = \frac{\alpha \Delta \Phi_s}{G_{th}} \qquad (6.15)$$

For a step change of the incident radiant flux:

$$\Delta \Phi_s(t) = 0 \qquad\qquad for\ t \leq 0$$

$$\Delta \Phi_s(t) = \Delta \Phi_{Son} \qquad for\ t > 0$$

73

By applying the complex frequencies s instead of the harmonic frequencies $j\omega$, the thermal model equation becomes

$$\underline{\Delta T_s}(s) = \frac{\alpha \Delta \Phi_s(s)}{G_{th}} \frac{1}{1+s\tau_{th}} \tag{6.16}$$

According to the Laplace transform, it results for the step function that

$$\Delta \Phi_s(s) = \frac{\Delta \Phi_{Son}}{s} \tag{6.17}$$

It follows that

$$\underline{\Delta T_s}(s) = \frac{\alpha}{G_{th}} \frac{1}{s+s^2\tau_{th}} \Delta \Phi_{Son} \tag{6.18}$$

and the Laplace inverse transform results in

$$\Delta T_s(t) = \frac{\alpha \Delta \Phi_{Son}}{G_{th}} \left(1 - e^{\frac{t}{\tau_{th}}}\right) \tag{6.19}$$

For $t-> \infty$, the steady-state final value becomes

$$\Delta T_s(t) = \frac{\alpha \Delta \Phi_{Son}}{G_{th}} \tag{6.20}$$

If radiant flux $\Delta \Phi_{Son}$ is interrupted at time $= t_0$, it results with the following conditions

$$\Delta \Phi_s(t) = \Delta \Phi_{Son} \qquad\qquad for\ t \leq t_0$$

$$\Delta \Phi_s(t) = 0 \qquad\qquad for\ t > t_0$$

analogously

$$\Delta T_S(t \geq t_0) = \Delta T_{Son} e^{-\frac{t-t_0}{\tau_{th}}} \tag{6.21}$$

For $t -> \infty$,we arrive at steady-state final value $\Delta T_{Soff} = 0$. Figures 6-11and 6-12 show the time functions for step radiant flux changes.
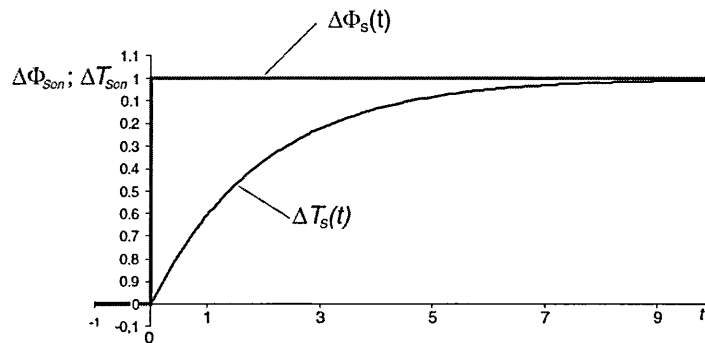

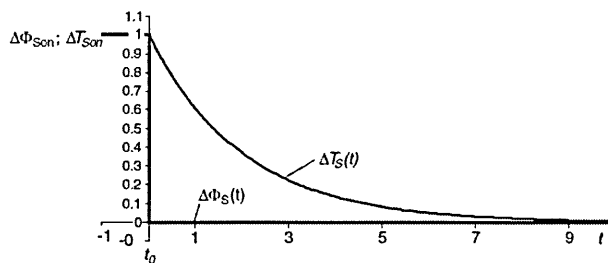Figure 6-11 Temperature change for radiant flux step (switching on)

Figure 6-12 Temperature change for radiant flux step (switching off)

From the figures above, it be can concluded that the response of a microbolometer sensor behaves like a first order low pass system with exponential rise and decay with the same time constant of τ.Hence, the PSF or the degradation function will have the same exponential characteristics.

The time constant τ for thermal detectors is a measure of the detector's speed of response and from the previous equation:

$$\tau_{th} = \frac{C_{th}}{G_{th}}$$

(6.22)

It is determined by the ratio of the heat capacitance and the heat conductance of the sensor. Obviously, a fast and sensitive thermal detector requires low heat

conductance for an optimum temperature increase and, as a consequence, also low heat capacitance (or mass) to exhibit a small time constant (Vollmer and Mollmann 2010).Two of the most widely used materials for microbolometer detectors are the Vanadium Oxide and Amorphous Silicon with typical time constants of 7ms and 15ms, respectively.
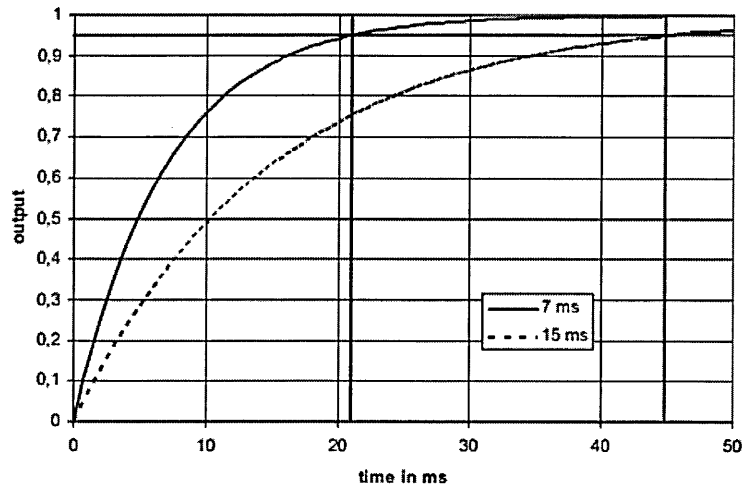

Figure 6-13 Output signal after an input step (Budzier and Gerlach 2011)

Figure 6-13 (Budzier et al. 2006) shows the a typical graph for both Vanadium Oxide (VOx) and Amorphous Silicon (a:Si) based camera responses to an input step. It can be seen that since the a:Si has a lower time constant, it rises more rapidly compared to the VOx. For both materials, after a time $> 3\tau$ the output becomes 95 % of its final value. This time is usually called response time (Table 6-1). The response time is the minimum time to be waited for after the object temperature is changed. After t $> 6\tau$ 99 % of the final value is reached. Table 6-1 below summarises the time constants and response times of both detectors.

Material	Time constant in ms	Response time in ms
Vanadium oxide VO_x	15	45
Amorphous silicon a:Si	7	21

Table 6-1 Typical values for thermal time constant

76

6.6 Decay constant estimation

As discussed in the previous section, the behaviour of a microbolometer camera can be characterised by an exponential point spread function, the one dimension normalised exponential PSF is:

$$h = \frac{1}{\tau} e^{-\frac{x}{\tau}}$$ (6.23)

The decay constant in the PSF equation above is not the decay constant of the camera but rather the decay constant of the blurred image, it can be calculated by the formula:

$$\tau_{image} = \tau_{camera} vr$$ (6.24)

Where τ_{camera} is the decay constant of the exponential time function of the electrical signal of the microbolometer detector, v is the speed of the moving object, r is the image resolution and τ_{image} is the decay constant of the exponential point spread function. From this equation, it can be seen that τ_{image} is proportional to τ_{camera} through v and r. In other words, the image is blurred more severely if the time constant of the camera is greater (slower camera response), if the object is moving faster or the resolution of the camera is higher.

This relationship is further investigated by a setup in Figure 6-14 to simulate an horizontal motion blur, a blackbody furnace was installed on a conveyer that was moved at a velocity of 1.5 m/s. The camera was located 1 metre away from the furnace and the camera detector was an Amorphous Silicon with a camera time constant of 8ms.
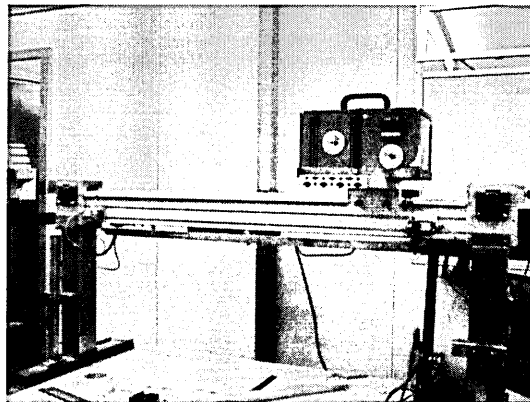

Figure 6-14 Experimental setup to simulate an horizontal motion blur

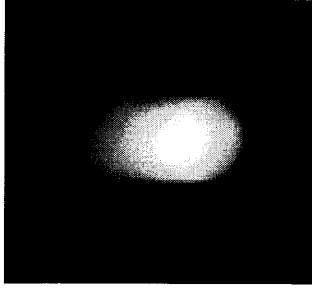Figure 6-15 shows the blurred image taken with the setup above

Figure 6-15 Captured blurred image

There are two methods to estimate the decay constant, τ_{image} of the blurred image. The first method is to use the formula as discussed previously:

$$\tau_{image} = \tau_{camera} vr$$

$$\tau_{image} = \tau_{camera} v \left(\frac{X_{resolution}}{X_{FOV} \cdot D}\right) \tag{6.26}$$

where

$$r = \left(\frac{X_{resolution}}{X_{FOV} \cdot D}\right)$$

where D is the distance of the camera to the object, $X_{resolution}$ is the horizontal camera resolution and X_{FOV} is the camera horizontal field of view. Both X_{FOV} and $X_{resolution}$ could be retrieved from the camera datasheet which are 25° and 640 pixels, respectively.

Substituting the parameters:

$$\tau_{camera} = 8 \times 10^{-3} s$$
$$v = 1.5\, m/s$$
$$D = 1\, m$$
$$X_{FOV} = 25°$$

into equation 6.26, obtain:

$$\tau_{image} = \tau_{camera} v \left(\frac{X_{resolution}}{X_{FOV} \cdot D}\right)$$

$$\tau_{image} = (8m)(1.5) \left(\frac{640}{tan25 \cdot 1}\right)$$

$$\tau_{image} = 16.47\ pixels$$

Alternatively, τ_{camera} could also be measured by fitting an exponential curve to the measured data. Figure 6-16 shows a line profile is placed at the centre of the blurred target.
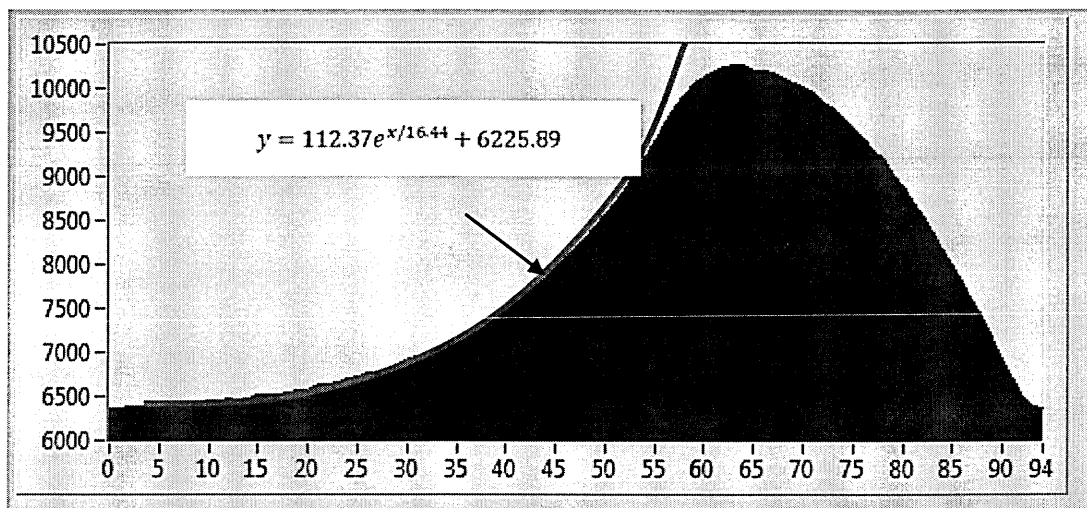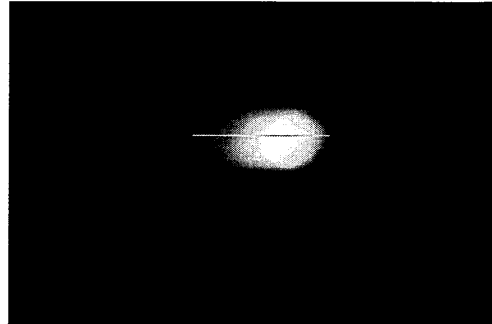

Figure 6-16 Exponential curve fitted to the blur profile

The red line on the intensity graph is the exponential curve fitted to the rising part of the blur profile. This exponential curve (red line) can be described by the equation:

$$y = 112.37e^{x/16.44} + 6225.89$$

The decay constant from the equation is essentially the τ_{image} which is 16.44. The measured value is very close to the theoretical value of 16.47. However, for a real image taken from the glass plant, the exponential curve is difficult to be fitted to the blur profile of the parison. This is because the parison does not have a uniform pixel intensity, the decay constant in the real case would need to

79

be calculated from the equation, therefore knowledge of the parameters i.e. τ_{camera}, v, r is important for an accurate estimation of the decay constant.

Once the τ_{image} is known, the PSF of the blur can be computed from equation 6.24:

$$h = \frac{1}{\tau} e^{-\frac{x}{\tau}}$$

$$h = \frac{1}{16.47} e^{-\frac{x}{16.47}}$$

Alternatively, the PSF from the experimental setup could be represented graphically in Figure 6-17:
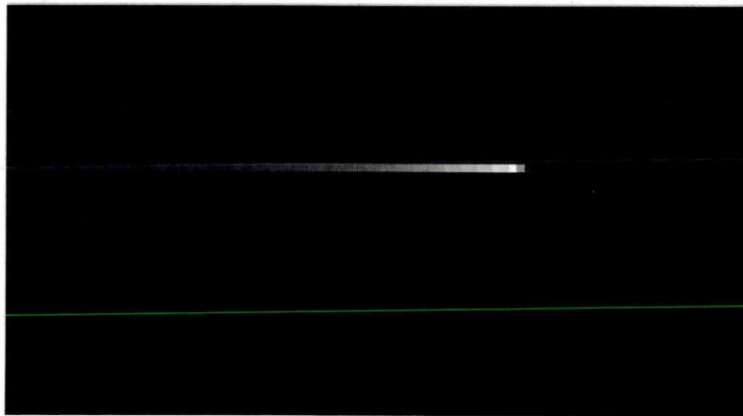

Figure 6-17 PSF of the experimental setup

Finding the PSF of the blur is the first step to image restoration/image deblurring. The next section discusses the image restoration technique in detail.

6.7 Image restoration

Image restoration can be defined as the estimation of the original image or ideal image from the observed one by the effective inversion of the degradation process through which the scene was imaged. This technique requires the knowledge of the degradation process or the PSF (Chanda and Majumder 2006).

In other words, the objective of image restoration is to calculate an estimate $\hat{f}(x,y)$ of the ideal image $f(x,y)$, given only the degraded image $g(x,y)$, the blurring function $h(x,y)$ and some information about the statistical properties of the ideal image and the noise. Three widely known restoration filters are discussed in the following section.

6.7.1 Inverse filtering

The simplest approach to restoration is direct inverse filtering, where an estimate, $\hat{F}(u,v)$ of the transform of the original image is calculated simply by dividing the transform of the degraded image, $G(u,v)$, by the blurring function $H(u,v)$:

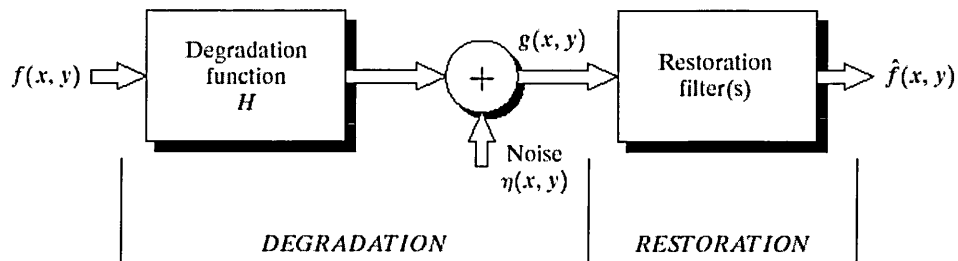$$\hat{F}(u,v) = \frac{G(u,v)}{H(u,v)} \qquad (6.27)$$

Figure 6-18 Model of the image degradation and restoration processes

In addition to the blurring effect, an adding noise term has to be considered in the process, as shown in Figure 6-18. There can be several noise terms in a microbolometer camera system:

Photon noise: Also known as Poisson noise, it is a basic form of uncertainty associated with the measurement of light, inherent to the quantised nature of light and the independence of photon detections (Hansinoff 2012).

81

Johnson noise: This form of noise is always present in any resistive material and arises from the random motion of the carriers. It is proportional to the square root of the temperature and the square root of the frequency bandwidth.

Readout amplifier noise: The amplifier that is used to amplify the output signal from a detector will itself introduce noise. How significant this noise is will depend on the level of the signal from the detector (L.Williams 2009).

Adding a noise term to the equation 6.28 yields:

$$\hat{F}(u,v) = F(u,v) + \frac{N(u,v)}{H(u,v)} \qquad (6.29)$$

This equation describes that even if the PSF or blurring function is known, it is not possible to recover the un-blurred image exactly because $N(u,v)$ is not known. If the blurring function has zero or very small values, then the ratio $\frac{N(u,v)}{H(u,v)}$ could easily dominate the estimate $F(u,v)$.

In practice, the straight inverse filter rarely works satisfactorily and should only ever be used with extreme caution (Solomon and Breckon 2011).

6.7.2 Minimum mean square error (Wiener) filter

The inverse filtering approach discussed in the previous section makes no explicit provision for handling the noise term. In this section, a filter is presented that incorporates both the blurring function and the statistical characteristics of noise into the restoration process. The method is based on considering images and noise as random variables and the objective is to find an estimate $\hat{f}$ of the uncorrupted image f such that the mean square error between them is minimised. This error measure is given by

$$e^2 = E\{(f - \hat{f})^2\} \qquad (6.29)$$

Where $E\{.\}$ is the mean expected value of the argument. It is assumed that the noise and the image are uncorrelated; that one or the other has zero mean. Based on these conditions, the minimum of the error function is given in the frequency domain by the expression 6.30. A full derivation of the Wiener filter can be found on (Hoggar 2006).

$$\hat{F}(u,v) = \left[\frac{H^*(u,v)S_f(u,v)}{S_f(u,v)|H(u,v)|^2 + S_n(u,v)}\right]G(u,v)$$

$$= \left[\frac{H^*(u,v)}{|H(u,v)|^2 + \frac{S_n(u,v)}{S_f(u,v)}}\right]G(u,v)$$

$$= \left[\frac{1}{H(u,v)}\frac{|H(u,v)|^2}{|H(u,v)|^2 + \frac{S_n(u,v)}{S_f(u,v)}}\right]G(u,v) \tag{6.30}$$

Where:

$H(u,v) = Degradation\ function$

$H^*(u,v) = Complex\ Conjugate\ of\ H(u,v)$

$|H(u,v)|^2 = H^*(u,v)H(u,v)$

$S_n(u,v) = |N(u,v)|^2 = Power\ Spectrum\ of\ noise$

$S_f(u,v) = |F(u,v)|^2 = Power\ Spectrum\ of\ undegraded\ image$

This result is known as the Wiener Filter. The filter, which consists of the terms inside the brackets, is also commonly referred to as the minimum mean square error filter or the least square error filter. The Weiner filter does not have the same problem as the inverse filter with zeros in the blurring function (Gonzalez and Woods 2008).

The restored image in the spatial domain is given by the inverse Fourier transform of the frequency domain estimate $\hat{F}(u,v)$. Note that if the noise is zero then the noise power term vanishes and the Wiener filter reduces to the inverse filter.

A number of useful measures are based on the power spectra of noise and of the undegraded image. One of the most important measure is the signal to noise ratio, approximated using frequency domain quantities such as

$$SNR = \frac{\sum_{u=0}^{M-1}\sum_{v=0}^{N-1}|F(u,v)|^2}{\sum_{u=0}^{M-1}\sum_{v=0}^{N-1}|N(u,v)|^2} \tag{6.32}$$

This ratio gives a measure of the level of information bearing signal power(ie of original, un-degraded image) to the level of noise power. Images with low noise tend to have a high SNR and, conversely the same image with a higher level of noise has a lower SNR. This ratio by itself is of limited value, but it is an

important metrics used in characterising the performance of a restoration algorithm.

When dealing with spectrally white noise, the spectrum $|N(u,v)|^2$ is a constant, which simplifies things considerably. However, the power spectrum of the un-degraded image is rarely known. An approach used frequently when these quantities are not known or cannot be estimated is to approximate by the term K (Gonzalez and Woods 2008). The estimation of the K is left to the user of the Weiner filter as if it were a tuneable parameter. Small values of K will yield a result close to the inverse filter, while large values will over smooth the restored image. In this thesis, the K parameter is selected based on the performance of the PSNR of the deblurred image. PSNR which (Peak Signal to Noise Ratio) is a popular parameter used to evaluate the quality of an image and is discussed in more detail in Section 6.9.
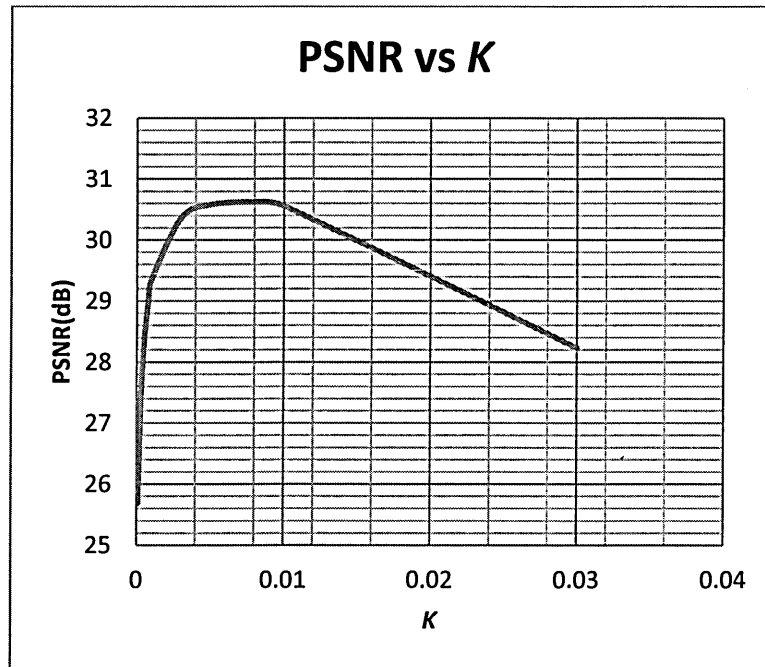

Figure 6-19 PSNR vs K

In order to select an optimum K value, an image was deblurred using different K values and the results are shown in Figure 6-19. It can be seen that the best results (highest PSNR) are obtained by using $K \approx 0.005$. The Weiner Filter equation could then be represented by:

$$\hat{F}(u,v) = \left[\frac{1}{H(u,v)} \frac{|H(u,v)|^2}{|H(u,v)|^2 + K}\right] G(u,v) \qquad (6.33)$$

84

6.7.3 Lucy Richardson filter

The Lucy Richardson (LR) method is an iterative algorithm which attempts to find the maximum-likelihood solution given knowledge of the PSF and the assumption of Poisson noise. Therefore, like the Wiener Filter, it could handle image noise better than a direct inverse filter. Let the ith pixel in the input distribution have value f_i. This is related to the observed value of the ith pixel in the output g_i by

$$g_i = \sum_j h_{ij} f_j \tag{6.33}$$

where the summation over index j provides the contribution of each input pixel, as expressed by the PSF h_{ij}, to the observed output pixel. It is customary to normalise the discrete PSF so that $\sum_i \sum_j h_{ij} f_j = 1$.

The iterative LR formula is given by

$$f_j = f_i \sum_i \left(\frac{h_{ij} g_i}{\sum_k h_{ik} f_k} \right) \tag{6.34}$$

where the kernel in Equation 6.34 approaches unity as the iterations progress. Full derivation of the Lucy Richardson filter can be obtained from (Solomon and Breckon 2011).

6.8 Comparison of filters

As mentioned, it is often more efficient to implement image restoration algorithms in the frequency domain. The spatial PSF representation from Section 6.6 can be converted to the frequency domain by applying the Fourier transform to equation 6.23.

$$h = \frac{1}{\tau} e^{-\frac{x}{\tau}}$$

$$H = \int_{-\infty}^{\infty} h \cdot e^{-i\omega x} dx$$

$$H = \frac{1}{\tau} \int_0^{\infty} e^{-\frac{x}{\tau}} \cdot e^{-i\omega x} dx$$

$$H = \frac{1}{\tau} \int_0^{\infty} e^{-x(i\omega + \frac{1}{\tau})} dx$$

$$H = \frac{1}{\tau} \left| \frac{e^{-x(i\omega+\frac{1}{\tau})}}{-(\frac{1}{\tau}+i\omega)} \right|_0^\infty$$

$$H = \frac{1}{\tau} \left(\frac{1}{\frac{1}{\tau}+i\omega} \right)$$

$$H = \frac{1}{1+i\tau\omega} \tag{6.45}$$

With the blur function or the PSF function in the spectral domain, the three filters, namely inverse filter, Wiener filter and Lucy Richardson filter can be applied to the blurred image to restore the approximated original image or the ideal image. The blurred image is taken from the experiment discussed in Section 6.6.

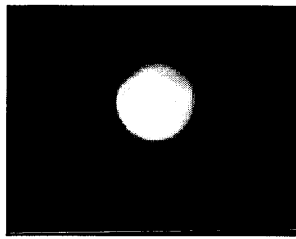The results of the restoration based on the discussion above are shown in Figure 6-21.

Figure 6-20 Original un-blurred image

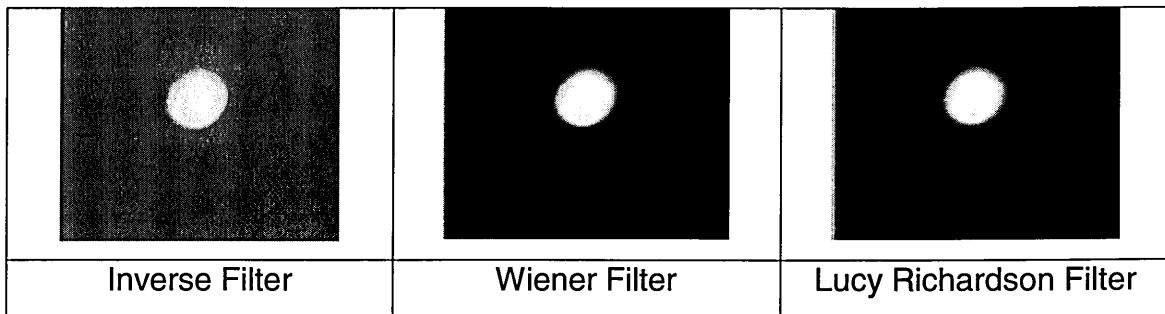| Inverse Filter	Wiener Filter	Lucy Richardson Filter

Figure 6-21 Deblurred images

Visually, the Weiner filter and the LR filter perform much better than the inverse filter, this is to be expected as these two filters can handle image noise. Apart from visual perception, the quality of the restoration filter can be determined quantitatively by using the PSNR (Peak Signal to Noise Ratio). It is chosen because of its simplicity and it is the most popular evaluation of the quality

difference among pictures. It is a ratio between the maximum possible power of a signal and the power of corrupting noise that affects the fidelity of its representation.

However, it is well-known that the PSNR does not necessarily accurately model perceptual quality (Wang 2006). The PSNR is derived by setting the mean squared error (MSE) in relation to the maximum possible value of the luminance (for a typical 8-bit value this is 255) as follows:

$$MSE = \frac{\sum_{i=1}^{M} \sum_{j=1}^{N} [f(i,j) - F(i,j)]^2}{M \cdot N}$$
(6.46)

$$PSNR = 20 \cdot log_{10} \left(\frac{255}{\sqrt{MSE}} \right)$$
(6.47)

Where $f(i,j)$ is the original signal at pixel (i,j), $F(i,j)$ is the reconstructed signal, and M x N is the picture size. The result is a single number in decibels, ranging from 30 to 40 for medium to high quality video.

The Table below shows the PSNR for each filter:

Filter	PSNR(dB)
Inverse	23.00
Wiener	30.58
Lucy Richardson	31.30

Table 6-2 PSNR for three restoration filters

As expected from the inverse filter, the noise dominated the results as explained. Whenever noise is present, the use of an inverse filter will have unpredictable and often disastrous effects. The Wiener filter gives much improved results with a PNSR of 30.58dB as it has the capability to "damp" frequency components that are dominated by noise. The Lucy Richardson filter with iteration of 50 gives slightly better results than the Wiener filter with PSNR of 31.30dB. However, the Lucy Richardson algorithm required several iterations in order to converge to the maximum likelihood solution. Since it is an iterations based filter, speed of execution is much slower than the Wiener filter. For this reason, a Wiener filter is preferred and chosen as the system needs to perform analysis in real time.

6.9 Radon Transform

In Section 6.6, an experiment was setup to simulate a linear motion blur using a shift invariant deblurring method. It has to be noted that the motion blur simulated is actually a shift variant blur. Although the target/furnace is moving in a linear motion, the background remains static relative to the camera and only the furnace is blurred by its motion. Thus, the blur model in Section 6.7 should not be used; however, since the background is not of interest in temperature analysis, it does not matter if the background is not being restored successfully by the shift-invariant deblurring technique. This shift variant blur could be used to restore the target object with the technique as discussed.

However, there is another issue with the shift invariant deblurring model in the real IR images taken from the glass plant. The object/parison is moving in a rotational motion, therefore it is shift variant blur. The first method to deal with this issue is to assume that the rotational blur can be approximated by a linear blur, this is discussed in this section. The other method which transforms the rotational motion shift variant blur to a linear motion shift invariant blur which will be discussed in Section 6.10.

The method described in this section requires the assumption that the rotational blur can be approximated to a linear motion blur. The image needs to be segmented into the individual parison/objects, then the direction of the motion blur for each individual parison is determined by a combination of two image transform algorithms, namely the Fourier Transform and the Radon Transform. The image is then rotated horizontally according to the direction of the motion. Finally, a linear deblurring algorithm described in the previous section is applied to restore the image. Figure 6-22 shows the overview of the technique:
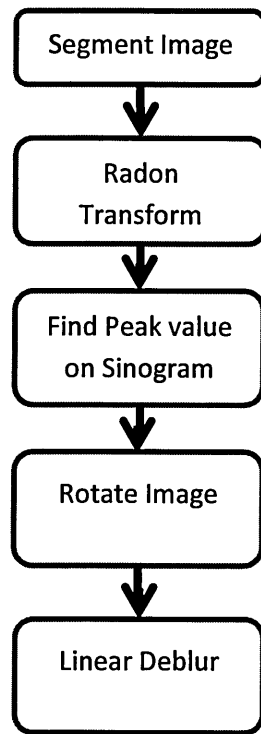
```
┌─────────────────────┐
│   Segment Image     │
└─────────────────────┘
           │
           ▼
┌─────────────────────┐
│      Radon          │
│    Transform        │
└─────────────────────┘
           │
           ▼
┌─────────────────────┐
│   Find Peak value   │
│    on Sinogram      │
└─────────────────────┘
           │
           ▼
┌─────────────────────┐
│    Rotate Image     │
│                     │
└─────────────────────┘
           │
           ▼
┌─────────────────────┐
│    Linear Deblur    │
│                     │
└─────────────────────┘
```

Figure 6-22 Overview of image deblurring technique with Radon Transform

6.9.1 Blur direction identification

In this technique, the rotational motion blur of the parison is approximated to a linear motion blur, it is therefore necessary to find the direction of the approximated linear motion blur in order to apply the shift invariant linear deblurring algorithm. This section will describe the blur direction identification as proposed by (Moghaddam and Jamzad 2004).

In an ideal image with no noise contamination, a shift invariant linear motion blur would cause parallel dark lines appear in the frequency response. The image below has been degraded with a diagonal blur. A careful investigation on its frequency spectrum reveals these parallel dark lines. A cross section of these lines reveals that the power spectrum of the blur function resembles a SINC form.
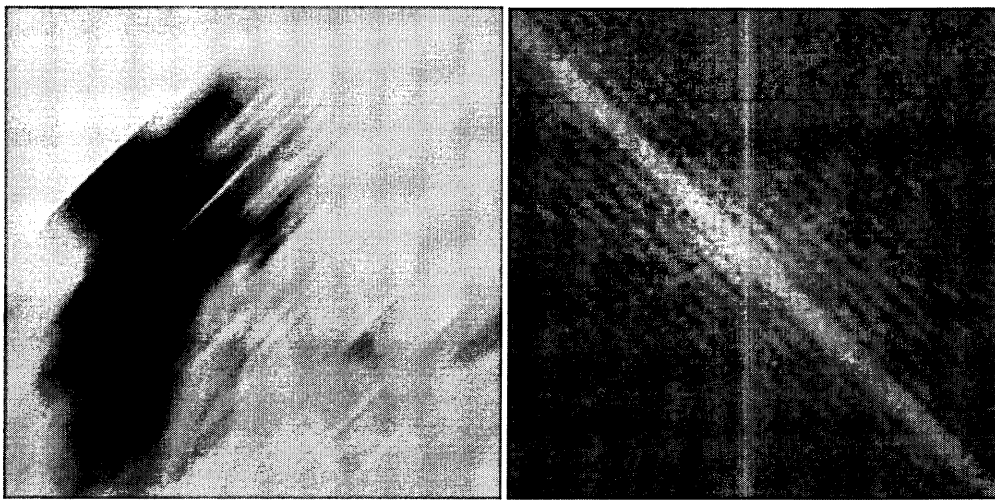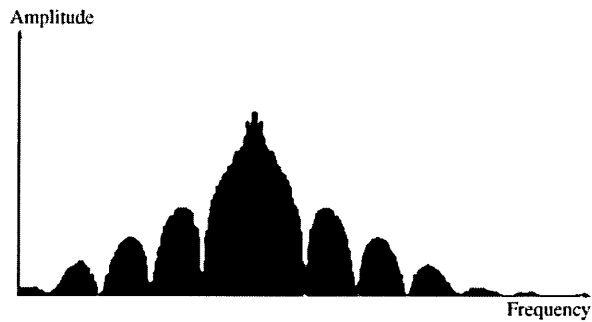
Figure 6-23 a) Noiseless blur image b) Frequency spectrum of image c) SINC function from cross section of (b)

The direction of these parallel dark lines can be used to determine the direction of the linear motion blur because the direction of the motion blur is perpendicular to the parallel dark lines. The discussion above was based on an ideal noise-free image. For a real image, when noise (Gaussian noise) is added to a blurred image, the parallel dark lines in the frequency response of the degraded image will become weak and some lines will disappear. If noise variance increases, then more such dark lines will disappear.
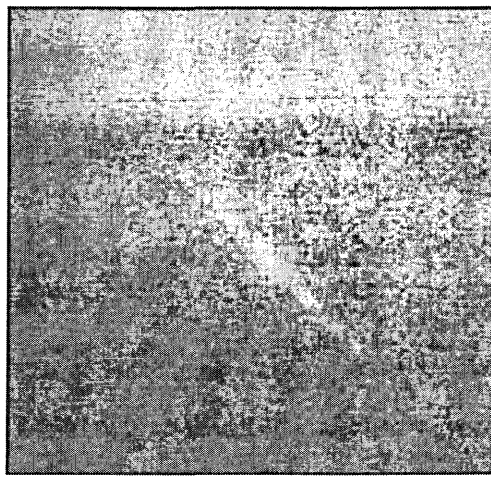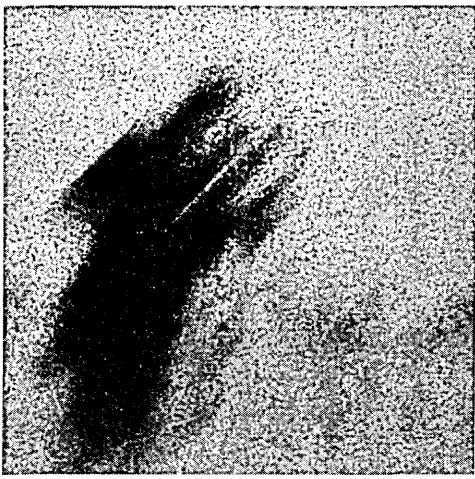
Figure 6-24 Noisy image and its frequency response

The white bound shown in Figure 6-24 is created because of the power spectrum structure of the degradation function. As shown in Figure 6-23, the power spectrum of a linear motion blur function has a SINC form. The white bound in the image frequency response is created because of the main lobe of the degradation function power spectrum. This lobe direction is the same as the parallel dark lines, therefore in practice, this white bound can be used to estimate the motion blur direction instead of using parallel dark lines.

To find these line directions, any line fitting method such as the Hough transform can be used. However, such a method needs to have appropriate candidate points to fit a line over them. To distinguish such points, it is required to perform a threshold operation to identify points on a line. This threshold is different for each image and a small error in finding the exact threshold produces a large number of wrong candidate points. To overcome this limitation, a Radon transform is used instead (Moghaddam and Jamzad 2006).
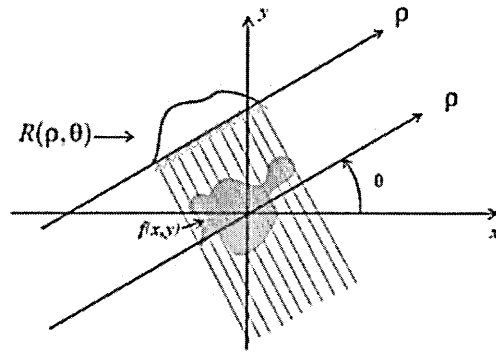
6.9.2 Radon transform

Figure 6-25 Radon transform (Hayden 2005)

The Radon transform of an image represented by the function $f(x,y)$ can be defined as a series of line integrals through $f(x,y)$ at different offsets from the origin. (Hayden 2005)

Applying the Radon transform on an image $f(x,y)$ for a given set of angles can be thought of as computing the projection of the image along the given angles. The resulting projection is the sum of the intensities of the pixels in each direction, i.e. a line integral. The result is a new image $R(\rho, \theta)$ (Hoilund 2007).

This can be written mathematically:

$$R(\rho, \theta) = \int_{-\infty}^{\infty} \int_{-\infty}^{\infty} f(x,y)\, \delta(\rho - x\cos\theta - y\sin\theta)\, dx\, dy \qquad (6.48)$$

This equation describes the integral along the lines through the image, where ρ is the distance of the line from the origin and θ is the angle from the horizontal.
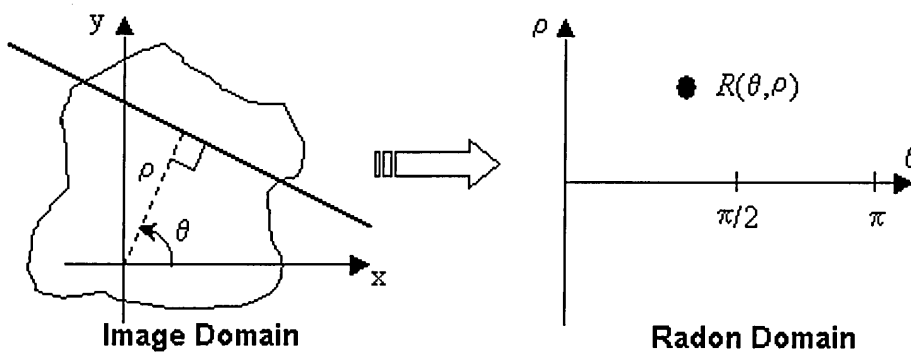

Figure 6-26 Image domain to radon domain (Hayden 2005)

In medical imaging, each point $R(\theta, \rho)$ is called a ray-sum, while the resulting image is called a Sinogram. Figure 2-27 shows the Radon transform of the frequency spectrum of Figure 6-26 (b), the peak occurs at 135 degrees, which is perpendicular to the direction of the linear motion blur at 45 degrees.
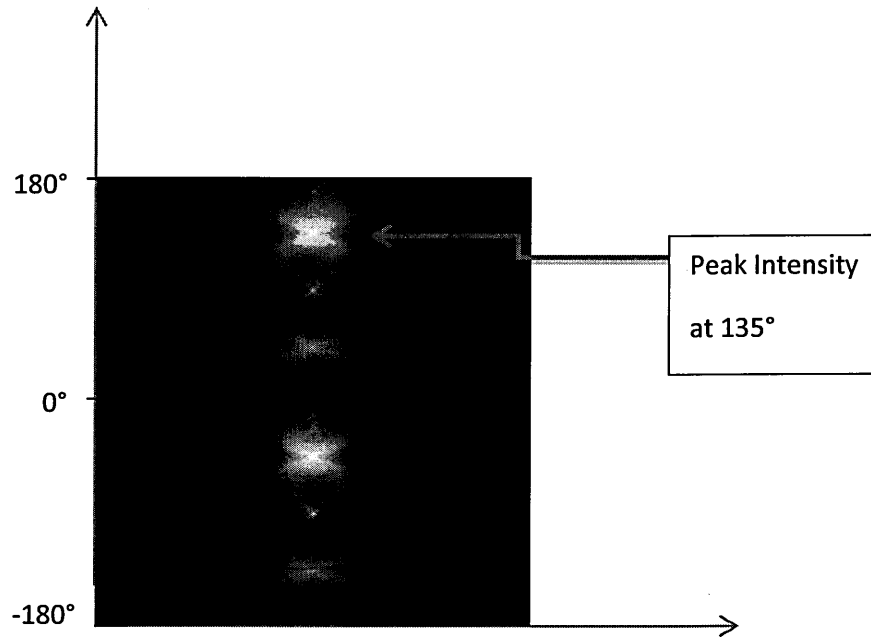

Figure 6-27 Radon transform of a synthetic image

The same technique can be applied to the images from the glass plant. The segmented image (Figure 6-28) is transformed to spectral domain as in Figure 2-29.
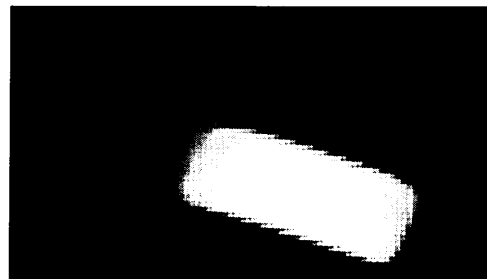

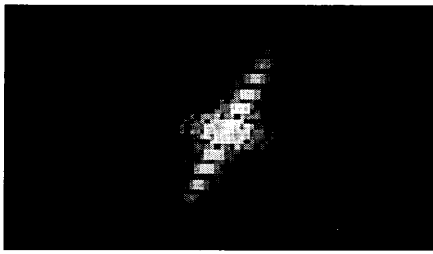Figure 6-28 Segmented Image

Figure 6-29 Fourier transform of the segmented image

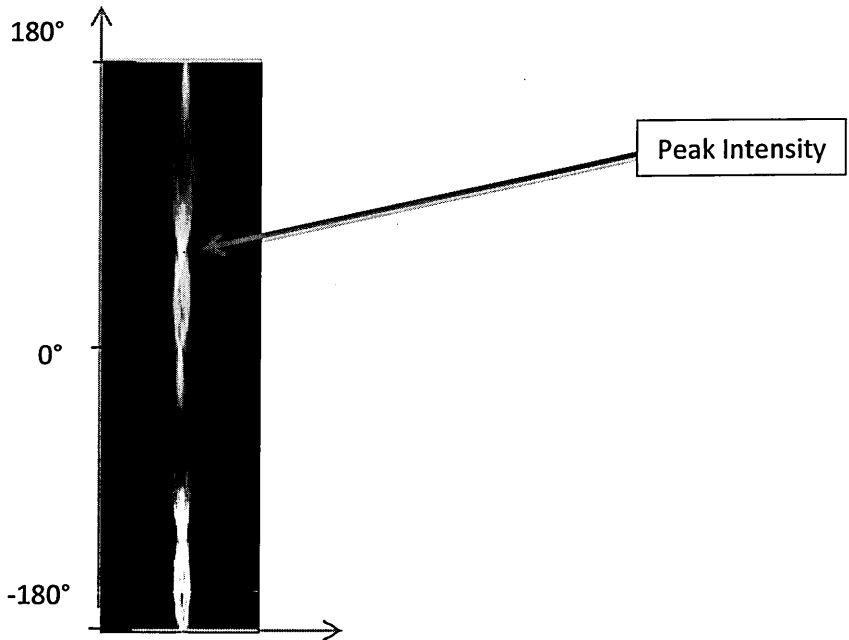Image in Figure 6-29 is then applied with Radon transform to determine the blur direction.

Figure 6-30 Radon transform

From the Sinogram, the peak intensity occurs at 62° and the blur direction is 62°+90°=152°. As can be seen, this technique is able to approximate the direction of the linear blur. Once the direction of the blur is known, the images can be easily rotated so that the blur direction can be approximated to a horizontal blur, then the linear motion deblurring algorithm described in the previous section can be used to deblur the images. Figure 6-31 shows the results.
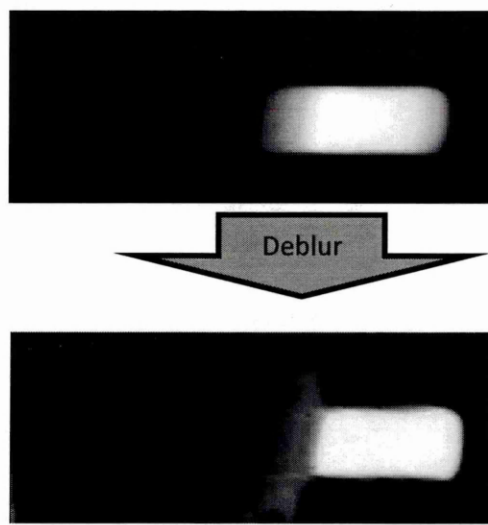
Figure 6-31 Result of deblurring technique utilising Radon transform

However, as mentioned at the beginning of this section, this technique is based on the assumption that the rotational blur of the parison could be approximated to a linear blur. Such assumption causes the algorithm to be less robust. This is apparent in Figure 6-32 where the artefacts can be seen.
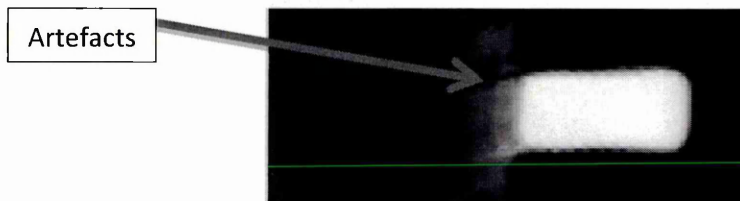

Figure 6-32 Artefacts on the deblurred image

In the next section, this assumption is removed and it will be discussed how the rotational motion can be converted to a shift invariant linear motion blur.

6.10 Image warping/mapping

In this section, conversion from rotational shift variant blur to linear motion shift invariant blur will be discussed in details. This conversion can be done by geometric mapping which is also known as image warping.
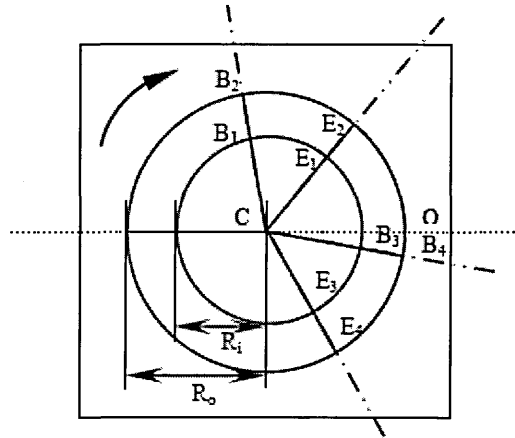

Figure 6-33 Illustration of rotational shift variant PSF (Ribaric, Milani and Kalafatic 2000)

When an object rotates in a plane on an axis, the PSFs or degradation function pertinent to all locations are different from each other. Take a clockwise rotation, as an example, as shown in Figure 6-33. First, consider points $B1$ and $B2$ that rotate to $E1$ and $E2$, respectively, during the exposure time. Their central angles are identical, namely, $\theta = \angle OCE_2 - \angle OCB_2 = \angle OCE_1 - \angle OCB_1$ but the radii are different, $R_o > R_i$. The blurring paths (the arc lengths) are

$$B_2E_2 = \frac{\theta R_o \pi}{180} \tag{6.49}$$

$$B_1E_1 = \frac{\theta R_i \pi}{180} \tag{6.50}$$

$$B_2E_2 > B_1E_1 \tag{6.51}$$

From this aspect, the rotary kernel of each position can be estimated as a series of length-varied arc motion blur, as demonstrated in Figure 6-34.
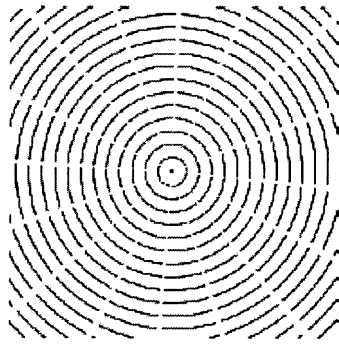
Figure 6-34 Synthetic graph for demonstrating rotary blur
kernels (Ribaric, Milani and Kalafatic 2000)

For visualization, Figure 6-35 shows a discretized image with a large snacing,
an arc sector in Cartesian corrdinate systems corresponding to a rectangular
one in polar systems. If those matrices are a set of blur kernels instead of the
entire image, then for each shift invariant PSF (a function of (ρ,θ)) in polar
coordinate systems, its corresponding shift variant PSF (a function of (x, y)) in
Cartesian coordinate systems is attainable. In such a way, blur kernels for all
the pixels of the captured image will be available for implementing a global
pixel-wise restoration/shift invariant deblurring approach in Cartesian systems.
Due to this transformation, the deblurring is analogous to the restoration of
images blurred by uniform linear motion parallel to one of the coordinate axes
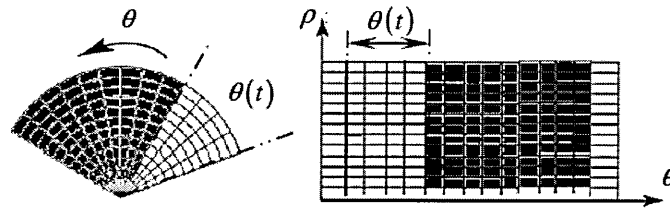(Ribaric, Milani and Kalafatic 2000).

Figure 6-35 Shift variant and corresponding shift invariant PSF (Ribaric, Milani
and Kalafatic 2000)

Mathematically, the mapping can be described as follows:

$$\rho = \sqrt{(x - x_o)^2 + (y - y_o)^2} \qquad (6.52)$$

$$\theta = \arctan\left(\frac{y - y_o}{x - x_o}\right) \qquad (6.53)$$

97

with ρ and θ being the radius and the angle, respectively, and (x_o, y_o) are the coordinates of the rotating centre. Accordingly, the inverse mapping equations are:

$$x = x_0 + \rho cos\theta \qquad (6.54)$$

$$y = y_o + \rho sin\theta \qquad (6.55)$$

Images below show the results of the mapping using the equations above. (x_o, y_o) are the centre coordinates of the image, with angle $\theta = 360°$.

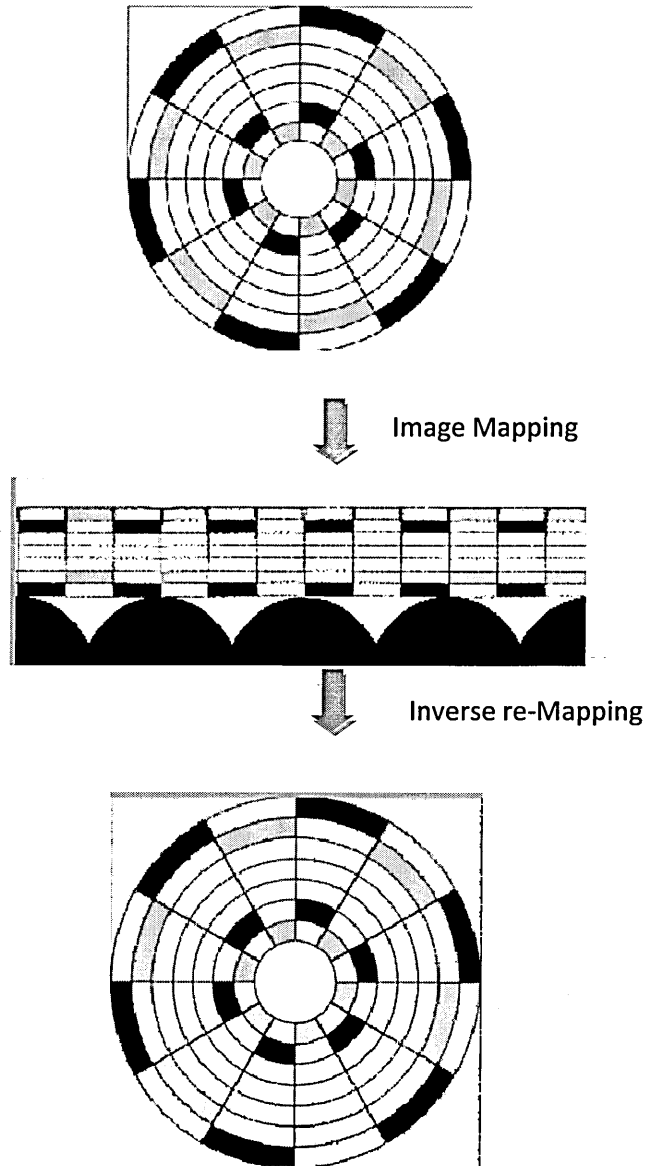Image Mapping

Inverse re-Mapping

Figure 6-36 Results from image mapping

An algorithm was developed based on equations 6.52 to 6.55 to implement the mapping function. As shown in Figure 6-37, there are some artefacts that

degrade the quality of the output image. These artefacts are due to the fact that digital images are sampled discretely. This is called aliasing artefact leading to staircasing or "jaggies" in the output.
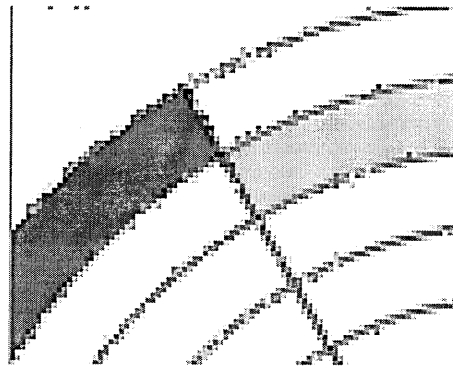

Figure 6-37 Aliasing Artefact

The artefacts can be minimised by using a technique known as super-sampling, which is basically performing interpolation among the nearest input pixels to determine the intensity of the output pixel value. In this thesis, bilinear interpolation is used to perform the super-sampling operation. If a coordinate system in which the four points where f is known are $[i,j], [Ii, j+1], [i+1,j], [i+1,j+1]$, the mathematics of the bilinear interpolation is shown below:

$$f(x,y) = (1-a)(1-b)f[i,j] + a(1-b)f[i+1,j] + ab\,f[i+1,j+1] + (1-a)b\,f[i,j+1] \tag{6.56}$$

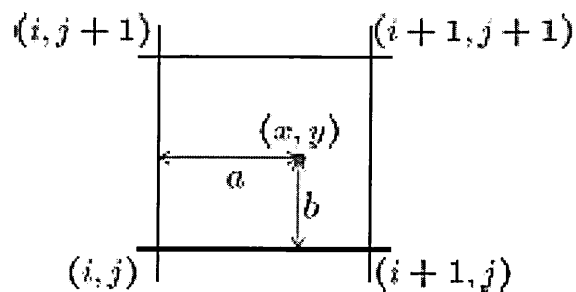which corresponds to Figure 6-38:

Figure 6-38 Bilinear interpolation

Figure 6-39 shows the improvement on the image after applying the super-sampling technique
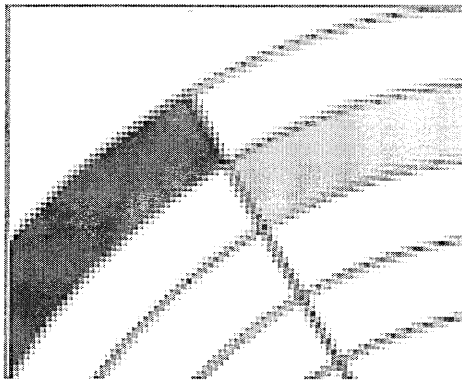
Figure 6-39 Results from super sampling using bilinear interpolation

6.10.1 Partial mapping

In the application described in this thesis, it is not necessary to map the full image since the background is not of interest for temperature analysis. To improve the algorithm's efficiency, only the selected portion of the image (i.e. the parison) is mapped to perform the linear shift invariant deblurring and re-mapping back to the original image coordinates system. Figure 8-8 shows only the selected region(red region) that was chosen to perform the mapping function.

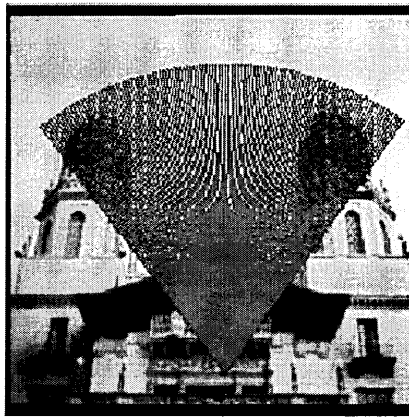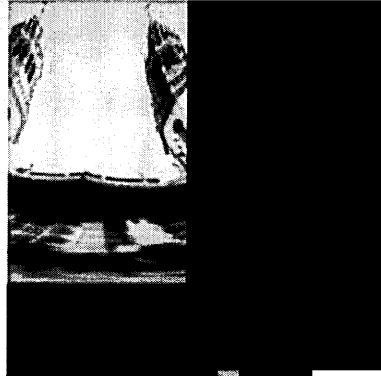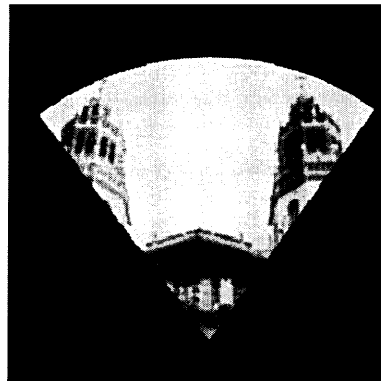Figure 6-40 Only the red portion of the image is mapped to the polar coordinate system and re-mapped to the original Cartesian coordinate system

6.10.2 Image warp on lab setup

In this section, the mapping algorithm with the linear shift invariant deblurring will be discussed. A test was setup to investigate the performance of both the mapping algorithm and the deblurring algorithm performance. The setup is shown below:
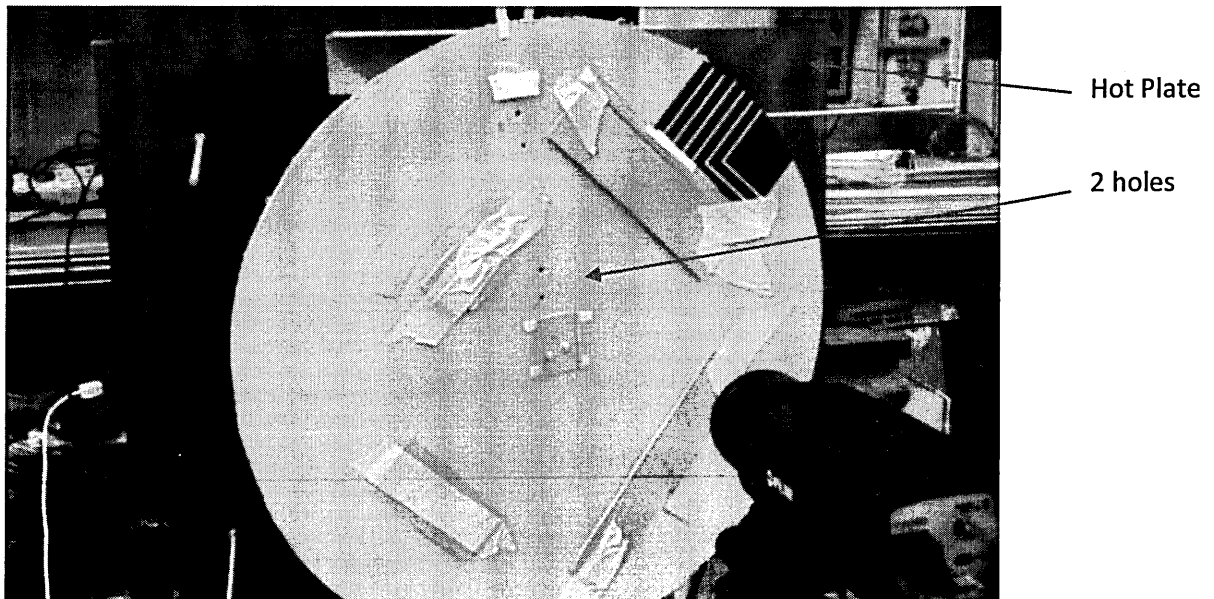
Figure 6-41 Experiment setup to test mapping and deblurring algorithm

The hot plate was heated to a temperature of approximately 150°C and the wheel was rotating at a constant speed of 75rpm. Images were taken when the wheel was rotating to simulate a rotational blur. Figure 8-9 shows the blurred image captured.
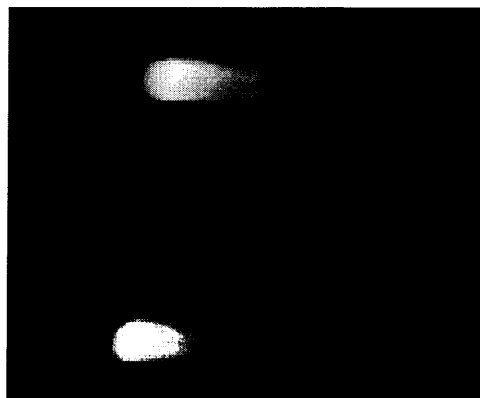
Figure 6-42 Captured blurred image

It can be noted that the object/hole at the top has a longer blurring artefact because it is moving faster due to the further distance from the centre of rotation. This rotational shift variant blur can be restored by using a combination of image mapping and linear shift invariant deblurring. The first step is to perform the image mapping to convert a rotational shift variant blur to a linear shift invariant blur. Figure 6-43 shows the results.
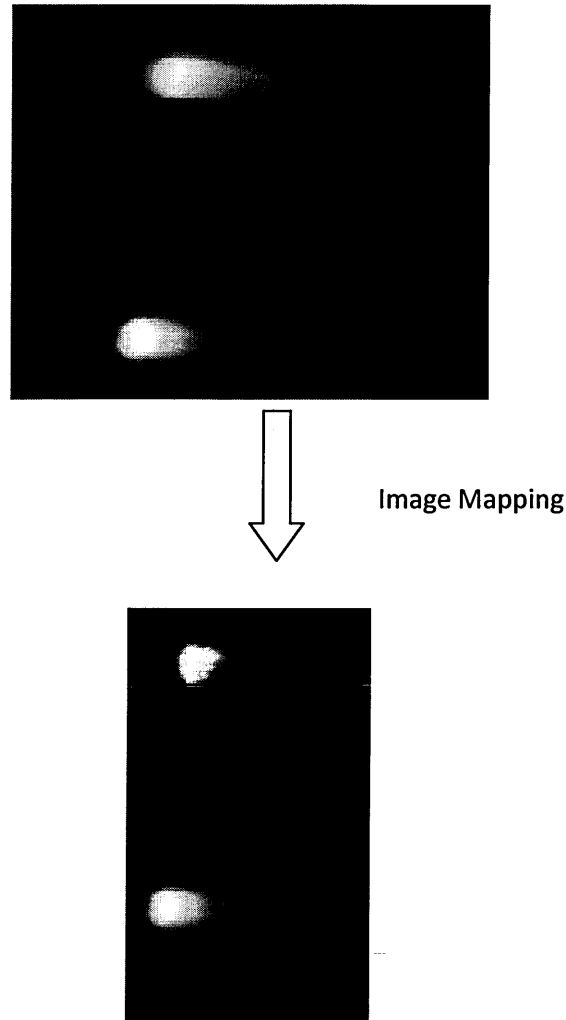
Figure 6-43 Result from image mapping

Once this process is completed, the image rotational blur is converted to a shift invariant linear blur. In order to deblur this image, the Wiener algorithm discussed in Section 6.7.2 is applied.
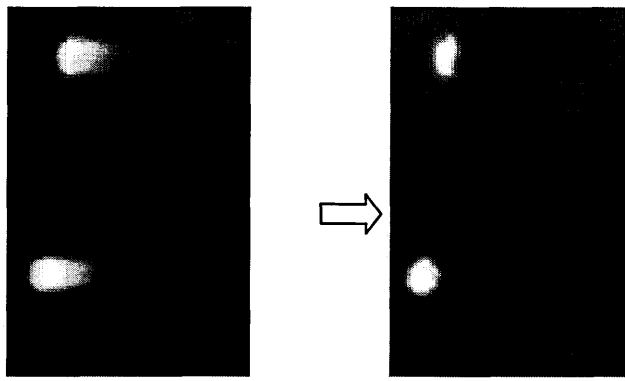
Figure 6-44 Deblurred mapped image

Finally, the image is re-mapped to restore the image to the original Cartesian coordinate system.
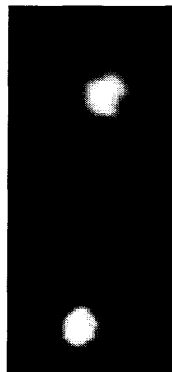
Figure 6-45 Re-mapping to restore image coordinates system

As can be seen, from the picture the image has been improved; the blurring artefact has been minimised significantly. Compared to the Radon transform method, this method does not show the artefacts from image restoration since the image blurring has been converted to a shift invariant blurring prior to the deblurring operation. Hence, this method provides a much better result.

Once image has been deblurred, temperature analysis can be performed on hot spots by taking the average pixels value. Figure 6-46 compares the temperature analysis results between a blurred image and a deblurred image.

| Blur image | Static image |

| Deblurred image |
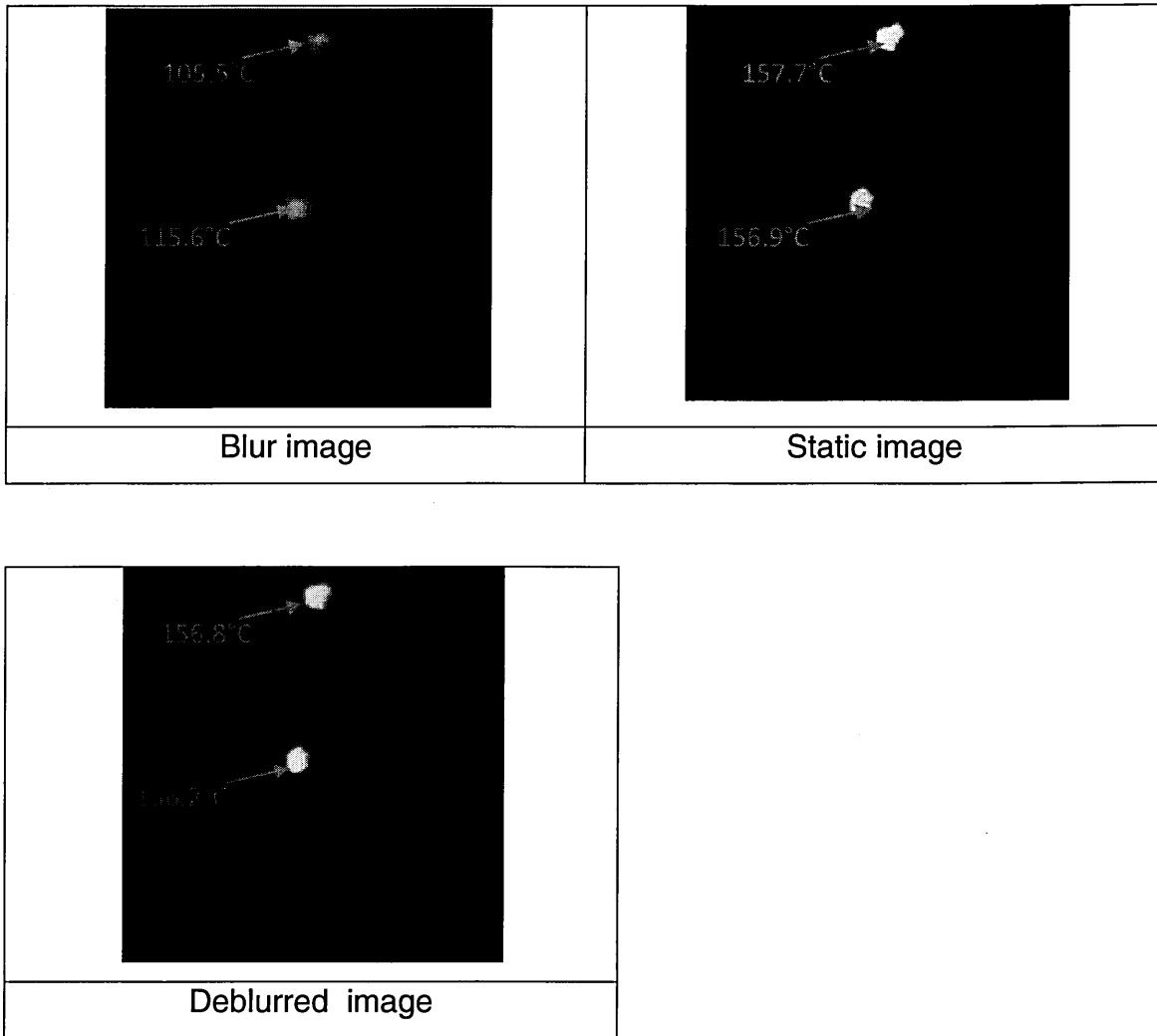
Figure 6-46 Comparison of a blurred image, a deblurred image and the original static image

As shown in Figure 6-46, there is a significant improvement in the precision of the temperature analysis. After the image has been successfully deblurred, the temperature reading is much closer to the original static image.

6.10.3 Centre point identification

As discussed in the previous section, it is necessary to provide a centre point as a reference point to perform the image mapping. From the IR images taken in the glass plant, it is not a straight forward task to retrieve this centre point. This is essentially the centre of rotation of the invert arm mechanism of each section.

In order for the image mapping algorithm to work on these images, the image coordinates of the centre of rotation for each section's invert arm mechanism is required.

A technique has been developed to retrieve this centre point. It starts by finding the centre of gravity of each parison on a sequence of images. A summation of these coordinates would give an array of points which represent the path of the parison's motion. From these points, finding the centre of the rotation could be done by fitting a circle on these points. This is essentially a minimisation of the following function:

$$f(r, x_o, y_o) = \sum_{i=1}^{i=n}[(x_i - x_o)^2 + (y_i - y_o)^2 - r^2]^2 \qquad (6.57)$$

Where

$$r = unknown\ radius$$
$$x_i and\ y_i = given\ points$$
$$x_o and\ y_o = unknown\ midpoint$$

The equation above shows that another variable, r , the radius of the invert arm is needed to solve the equation. This information can be obtained from the machine manual. Solving the linear equation would provide the x_o and y_o coordinates of the centre of rotation for the invert arm. Figure 6-47 shows this technique.
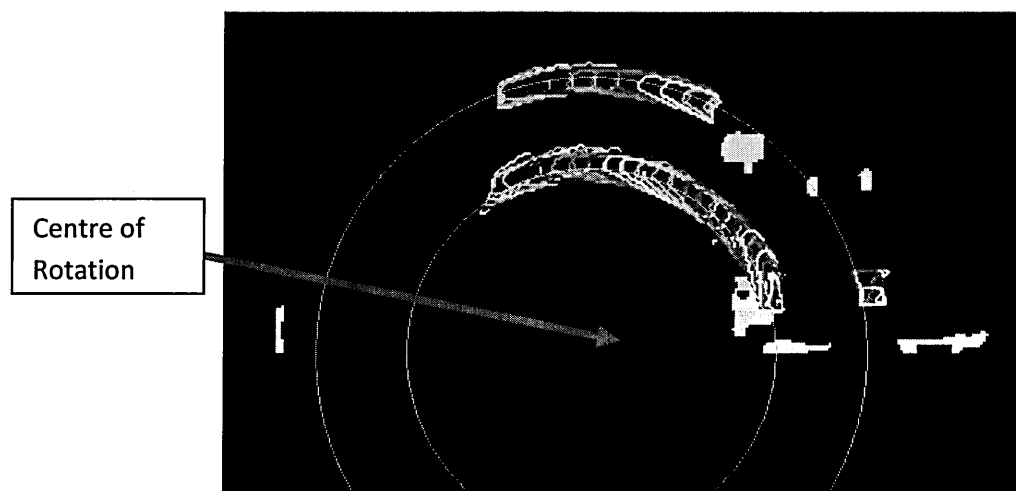
Figure 6-47 Sequence of images stacked together to fit a circle in order to find the centre of rotation

6.10.4 Warp and deblur IR image from glass plant

Once the centre point is calculated, its coordinates are then fed to the mapping algorithm. Figure 6-48 shows the result of the mapping algorithm on an image from the glass plant.
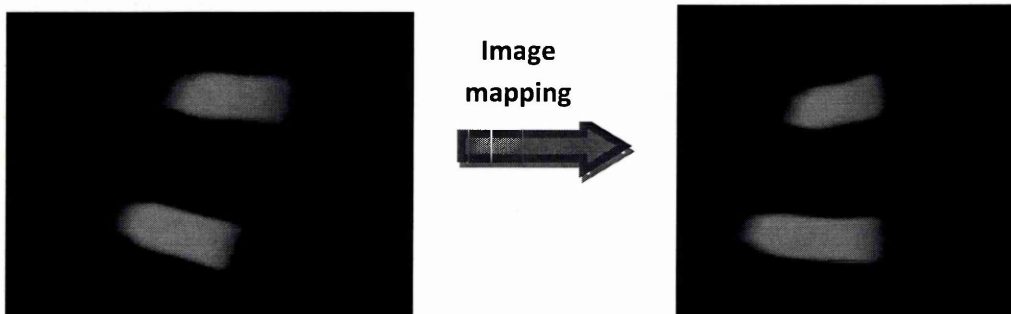
Figure 6-48 Image mapping on an image from the glass plant

Once the image is mapped, the blurring has become a shift invariant blurring as discussed previously; the image now can be restored with a linear shift invariant deblurring algorithm. Applying the linear Wiener deblurring algorithm to the mapped image gives the result below:
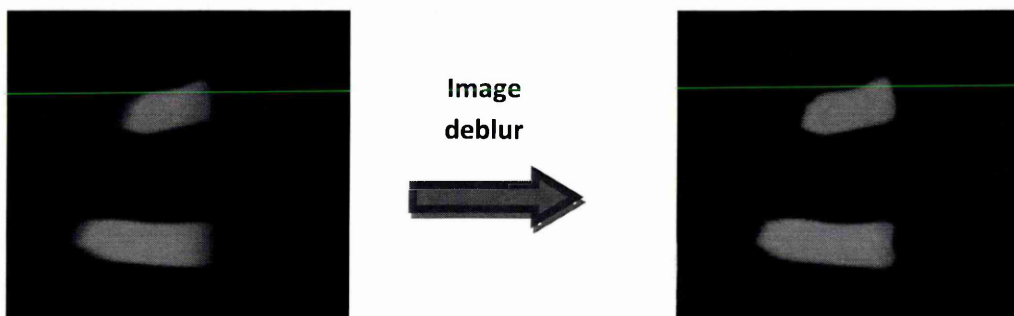
Figure 6-49 Image deblurring on image from the glass plant

Finally, similarly to the previous section, the image is un-warped and restored to the Cartesian coordinates.
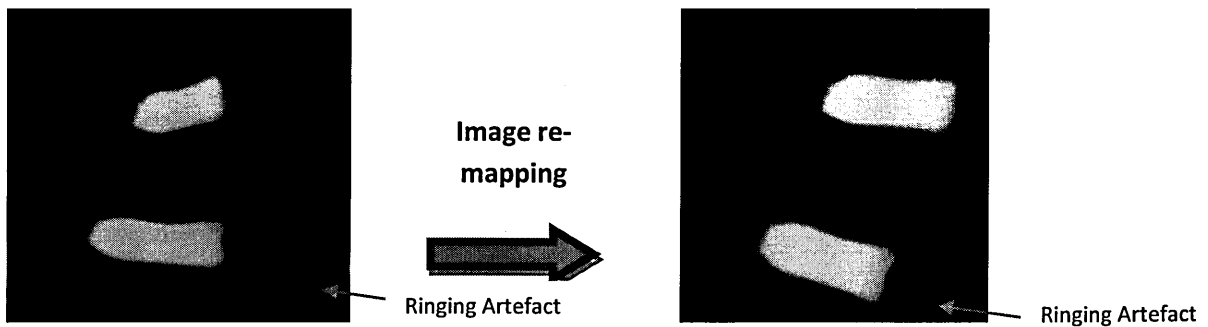
Figure 6-50 Re-mapping of the image from the glass plant

From the images above, it can be seen that the image has some "ringing" artefact due to its static background. The background does not move in the same direction and same speed as the parison. In other words, the background is static (not degraded by motion blur) and the parison is moving (degraded by motion blur). As the deblurring algorithm is a shift invariant i.e. debluring all points in the image with the same PSF, the deblurring algorithm has been applied unnecessarily to the background which is not corrupted by the motion blur. This causes the background to have the ringging artefacts from the deblurring algorithm. This can be solved by first segmenting the background against the moving object with its blur artefact prior to the procedure described in this chapter. Once the moving object is deblurred, this image portion is combined with the unaltered background portion to produce a complete image.

However, for this particular application this is not necessary since visual perception of the image is not important, the main objective of image deblurring is to restore the pixels intensity value of the parison in order to have a more accurate temperature reading. The pixel value of the background is not of concern. Once the parison has been deblurred, temperature analysis can be performed on the image. Figure 6-51 below compares the image and temperature values of a blurred and deblurred image.

767.10 °C

790.95 °C
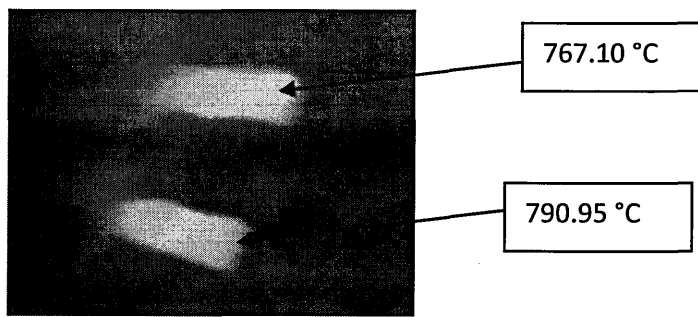
Original blurred image

784.22 °C

797.74 °C
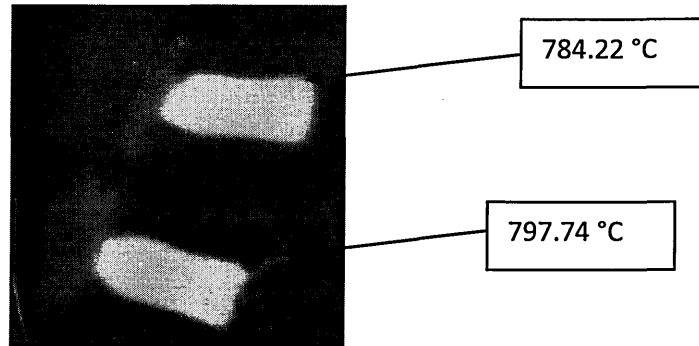
Deblurred image

Figure 6-51 Temperature reading before and after image deblurring

As expected, the temperature value increases when an image has been deblurred. This implies that for the system to be able to produce accurate temperature measurements of the parison, the image captured must be deblurred based on the techniques described in this chapter prior to conduct temperature analysis.

Chapter 7

System Implementation
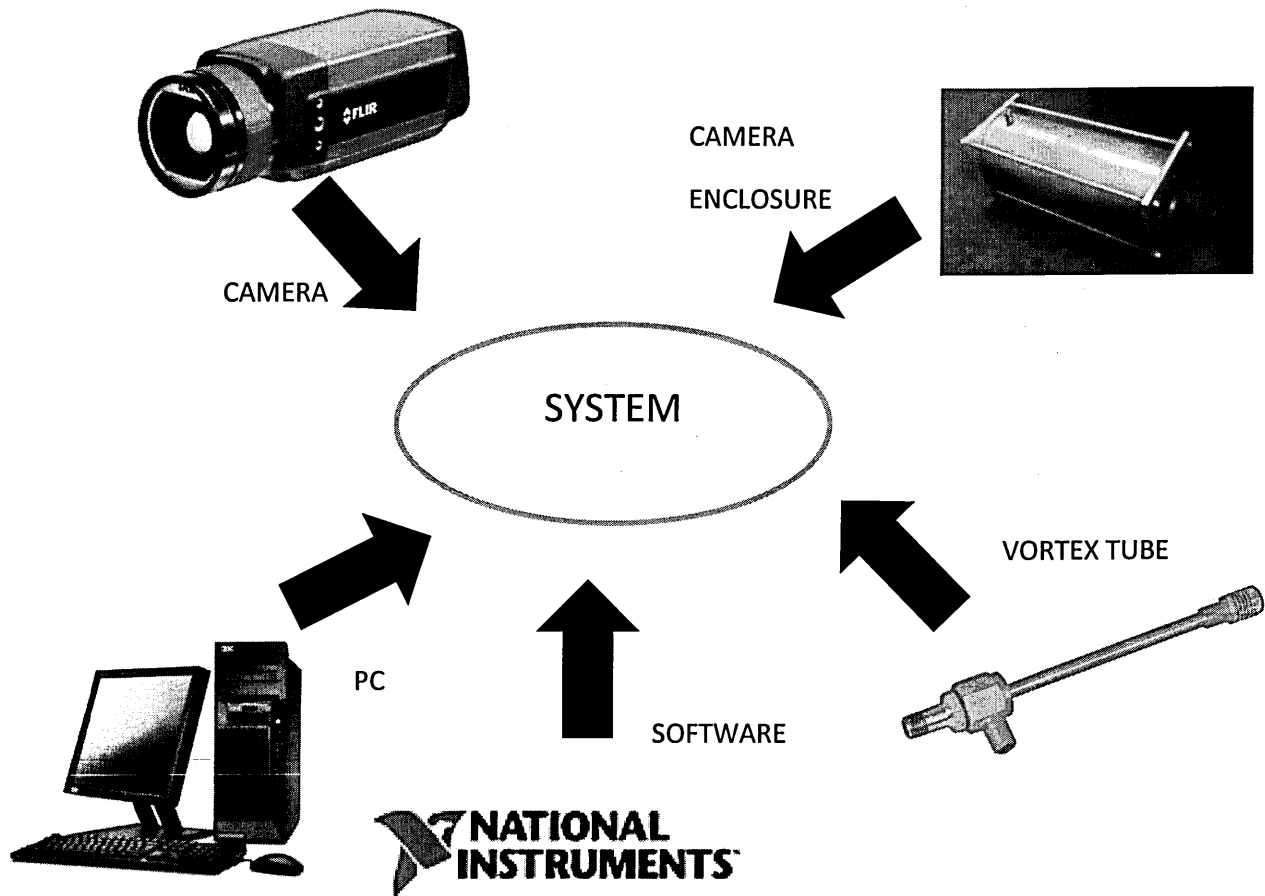
Figure 7-1 Components of the system

7.1 Infrared camera

The infrared camera used in this system is a FLIR 615. It is a microbolometer based camera which has a resolution of 640 x 480 and is capable of producing radiometric calibrated infrared images. The interface of the camera is the standard GigE Vision which is based on internet protocol standard and capable of transmitting high speed video (1000Mbit/s). The camera is also GeniCam compliant, which provides a unified application programming interface. This feature provides easier integration with other components, such as the camera and the image processing libraries.

7.2 Camera enclosure

A camera enclosure is required as the camera system must be capable of withstanding the hot and harsh environment in the glass plant. The average temperature where the camera will be mounted, which is at the side of the I.S. machine, could reach temperatures of 40°C. The enclosure will serve two purposes, keeping the camera electronics cool and keeping the camera lens clean. The enclosure uses the filtered plant air to create a "curtain" of flowing air that prevents dust and other outside debris from reaching the camera lens. To cool the camera, the enclosure uses cooled plant's air and circulate the air through the body of the camera at a constant rate. All exposed portions of the enclosure are made of aluminium to protect the camera from corrosive atmospheres.

7.3 Vortex tube

In order to keep the camera at a temperature range of 15°C to 25°C, a vortex tube is installed to cool the plant's air before it enters the camera enclosure. The vortex tube takes in normal plant's air and converts it into two air streams. One stream is cold air which goes to cool the camera and hot air which is dissipated in the environment. The advantage of a vortex tube is that is has no moving parts, therefore no maintenance is required.

7.4 PC

The PC used for this system is a i7 quad core processor which exploits the multithreading capabilities of the designed software. Multiple tasks could progress in parallel allowing efficient task execution and fast processing capabilities. User interaction with the system will be through standard keyboard and mouse.

7.5 Software

Labview was used to implement the software for this application, including the image processing algorithms, the software architecture and the user interface was designed in Labview. Labview is a graphical programming language with its built-in engineering specific libraries of software functions and hardware interfaces. The library used for image acquisition and image processing functions is NI's IMAQdx©. Figure 7-2 shows the software flow chart of the system.

```
┌─────────────────────┐
│   Acquire Images    │
│    Continuously     │
└─────────────────────┘
          │
          ▼
┌─────────────────────┐
│ Select Valid Image  │
│    for each section │
└─────────────────────┘
          │
          ▼
┌─────────────────────┐
│     Warp Image      │
└─────────────────────┘
          │
          ▼
┌─────────────────────┐
│    Deblur Image     │
└─────────────────────┘
          │
          ▼
┌─────────────────────┐
│   Un-Warp Image     │
└─────────────────────┘
          │
          ▼
┌─────────────────────┐
│    Temperature      │
│     Analysis        │
└─────────────────────┘
          │
          ▼
┌─────────────────────┐
│    Show Data on     │
│   User Interface    │
└─────────────────────┘
```
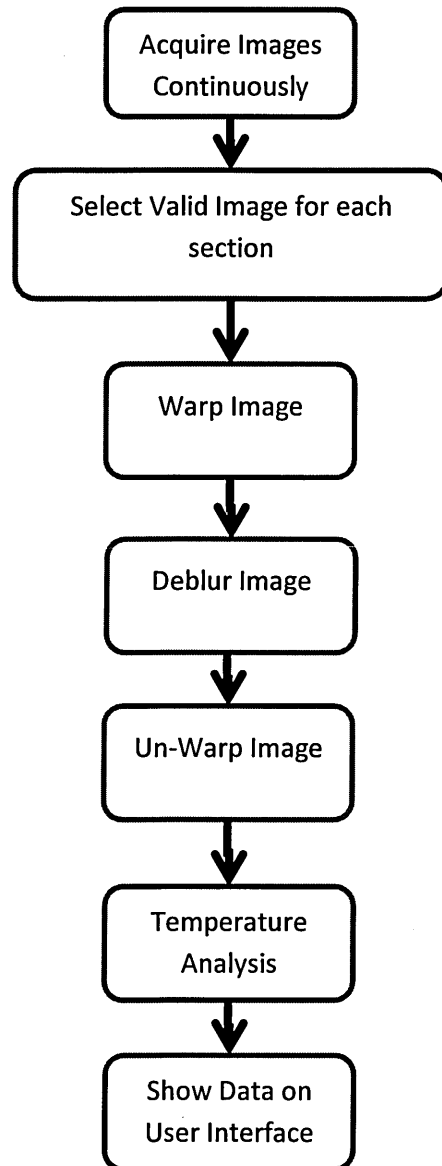
Figure 7-2 Software flow-chart

The software starts with a routine to find the centre of rotation of the invert mechanism for each individual section, as discussed in section 6.10.3. This centre of rotation is required for the image warp algorithm.

Then it will continuously acquire images and select valid images which have full view of the parisons, this was discussed in Chapter 4. These valid images will be fed to the deblurring algorithm. The deblurring routine starts by image warping to convert the rotational shift variant blur to linear shift invariant blur, then a shift invariant deblurring algorithm is applied to the converted image. The deblurring routine finishes by image un-warp to convert the image back to the original Cartesian coordinates system. The deblurring algorithm and image warping algorithm were discussed in Chapter 6.

Once the image has been deblurred, temperature analysis is performed. This is done simply by taking the average pixel values that depict the parisons. Finally, the temperature data is plotted on the graph display in the user interface of the system. All information is presented in clear graphs, these graphs give operator the necessary information about the parison and therefore help to improve it. Figure below shows the user interface of the system where eight graphs show each sections of the I.S. machine and the two plots show that it is double gob machine (i.e. two parisons).
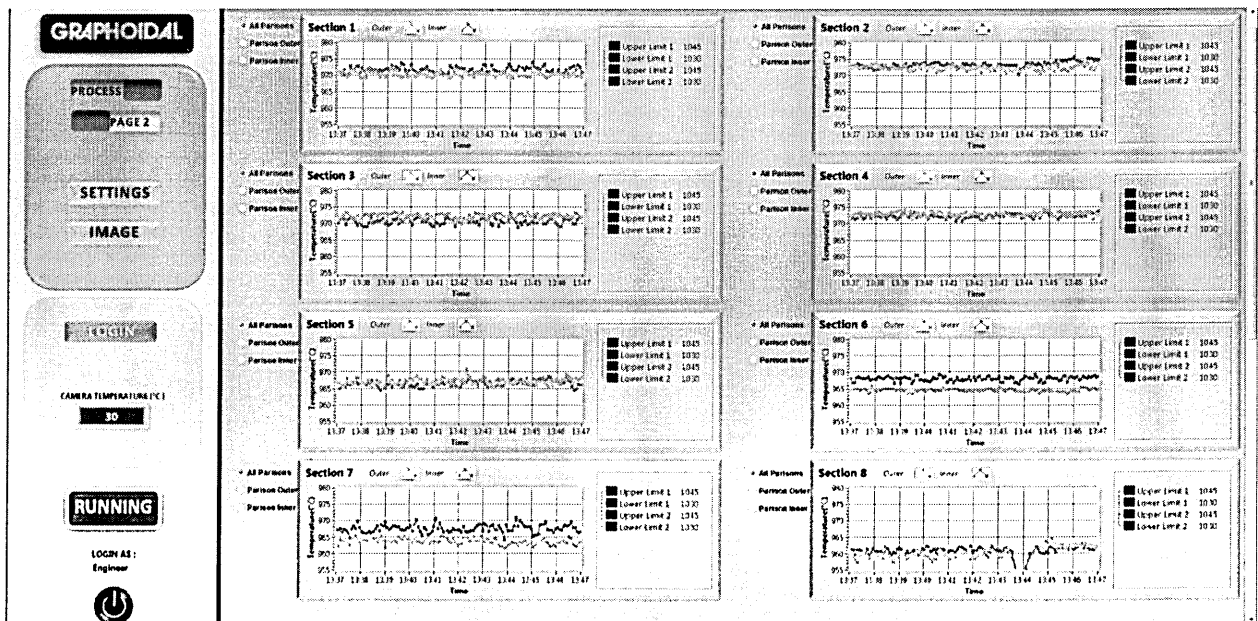

Figure 7-3 System user interface

7.6 Results

Figure 7-4 shows temperature data from section 2 when the machine is producing 500ml beer bottles. The data has been plotted using the EWMA techniques as described at section 2.6.2. When the mould cooling was reduce at 13:09 to simulate an error at the mould cooling, the data response to the change with a rise in temperature. The cooling was resumed to normal at 13:26 and the data shows that the parison temperature decreases gradually back to the initial temperature. The temperature data corresponded well to the mould temperature because with a LWIR camera, the surface temperatures of the parisons are measured and this temperature information has a strong correlation with the mould temperature. This is because when glass comes into contact with the working surface of the mould, intense heat transfer in the glass mould system takes place at the same time as well as changes in the glass shape. The fluctuation of other part of the data can be explain by the variation of the forming process due to the gob loading, swabbing, pollution of the mould, wear of cooling valve etc.
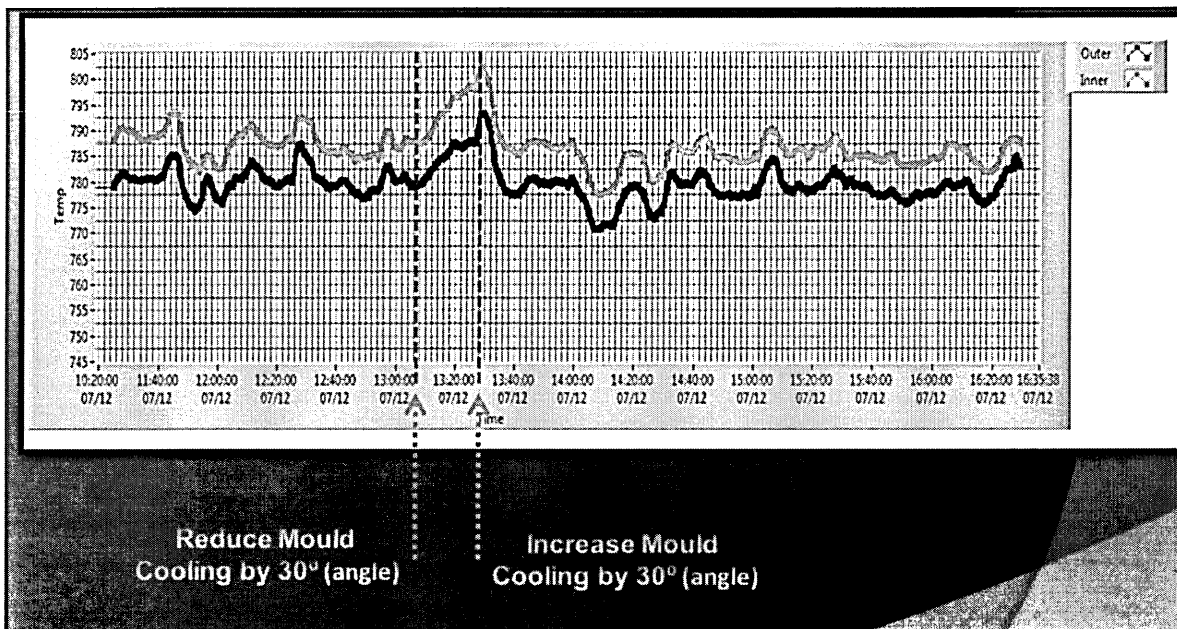

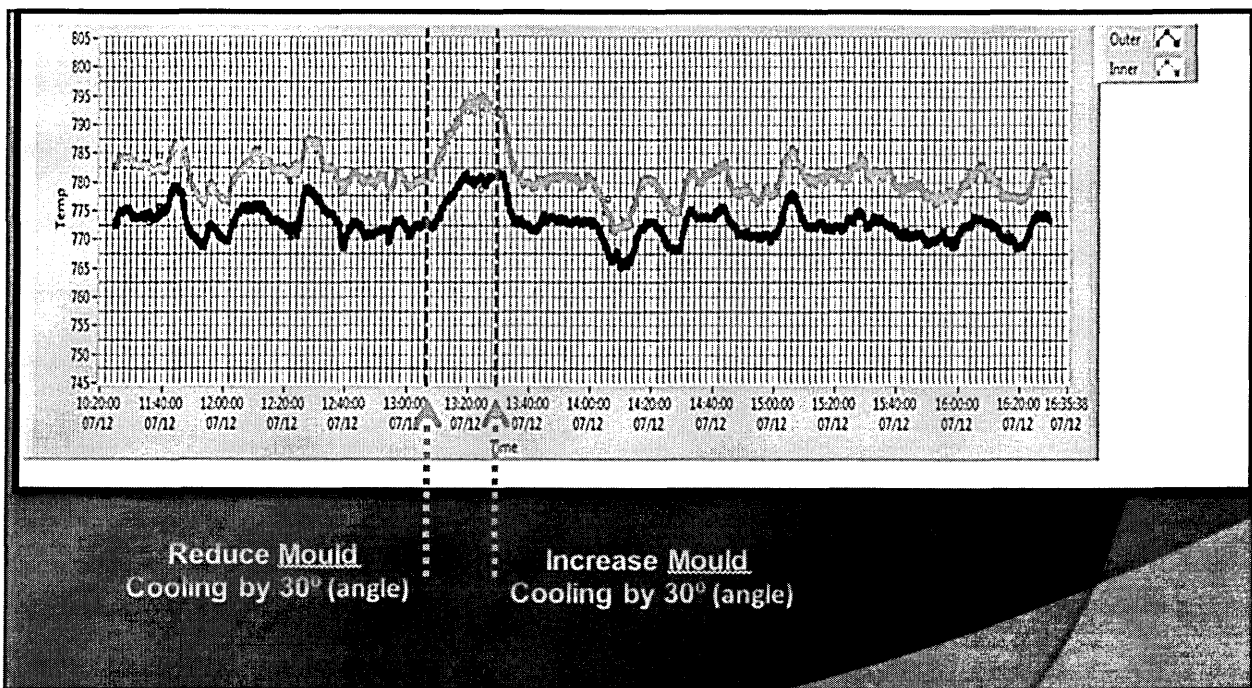Figure 7-4 Temperature data from section 2

114

Figure 7-5 Temperature data from section 8

Figure 7-5 shows data from section 8. Similar settings to the mould cooling were applied to section 8, the temperature increased at 13:09 where the operator reduced the mould cooling, then the temperature gradually resumed to the initial temperature when the operator increased the mould cooling at 13:26.

With this set of information, the data could be used to identify temperature trend of the parison and adjustment/optimisation of the I.S. machine can be made. When the forming process is deviating from the stable situation, there will be warning and the operator can intervene to restore the glass forming process. The operator could detect faults and adjust mould cooling accordingly to maintain the parison at an optimised temperature.

However, the system would not be able to provide a reliable absolute temperature reading, this is due to the deblur algorithm being very sensitive to its inputs parameters which are the motion speed, time constant of detector and resolution of camera system. In other words, a slight change in its input parameters would cause a big difference in temperature reading. Although the resolution and time constant of the detector can be determined relatively accurate, the speed of the parison motion is difficult to be determined. This is because the invert's arm mechanism does not necessary travel at a constant speed, therefore the parison's speed is not constant during the period what at

115

which is being transfer from blank to finish mould. In addition, in order to convert the rotational shift variant blur to a shift invariant blur, it is required to perform an image mapping, as described in Section 6.10.3, it requires the identification/estimation of the centre of rotation on the image. The prediction of these parameters is bound to have slight deviations from the true parameters, therefore accurate determination of parison's speed becomes difficult. Figures 7-6 and 7-7 show the effects of different speed to the temperature reading.
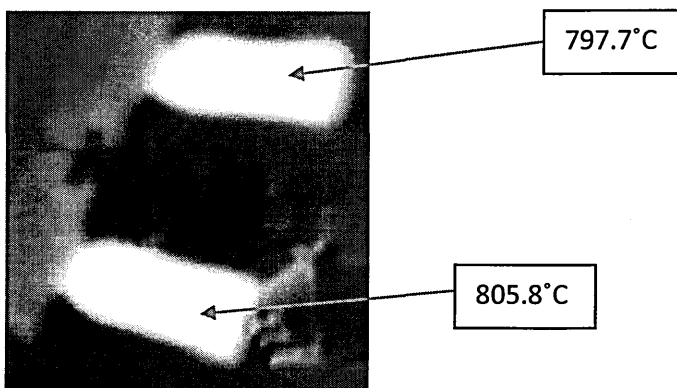
Figure 7-6 Deblurred with $\tau = 14.27$ pixels
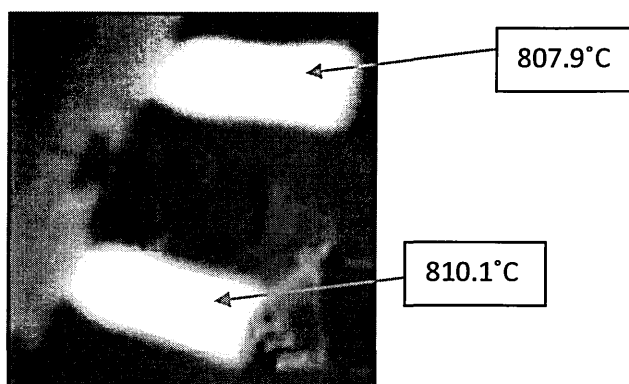
Figure 7-7 Deblurred with $\tau = 15.37$ pixels

Figure 7-6 shows the temperature reading of both parisons when the image is deblurred with an estimated velocity of 1.3 m/s. Figure 7-7 shows the parison's temperature when the image is deblurred with an estimated velocity of 1.4 m/s.

As shown, when the estimated velocity of the deblurring algorithm's parameter changes from 1.3 m/s to 1.4 m/s, the top parison increases in temperature by

116

10˚C while the bottom parison increases by 5˚C approximately. This shows that the algorithm is very sensitive to its input parameters. When the parameters are not determined accurately, the deblurring algorithm could have "over blurred" or "under blurred" a parison, this would give a false temperature reading. Therefore, this system would only be able to provide a trend of parison temperature and not the absolute temperature reading, these trends can be used for execute root cause analysis on faulty bottles and try to understand where the problem comes from, as well as what can be done to prevent faulty bottle being produce in future. As the IR information is real time, it is easier to execute root cause analysis to the machine. The temperature data represents fingerprint of the process failure and provides direct information on which process variables have failed such as thermal condition human interaction etc.

Chapter 8

Conclusion

During the formation of glass containers, the knowledge of the parison temperature is important because of the strong dependency of glass properties with its temperature. Within the forming range, a few degree changes in the glass temperature can change the glass viscosity by a huge factor, thus significantly affecting the moulding process. By monitoring the temperature of a parison, the operator could optimise the I.S. machine, thus increasing production rates and improving product quality with fewer defects.

This thesis describes a system that utilises an infrared camera and machine vision technology to monitor the temperature of the parison as it is being inverted, the camera is placed on the side of the machine to view parisons from each sections of an I.S. machine. The system is capable to automatically select images that have the full view of the parison from the image sequence, and then perform temperature analysis on these images.

A few issues were encountered during the development of this system. One of them is due to the perspective effect of the camera optics, parisons from further distance from the camera would be perceived as being smaller, and the reduction of pixels to represent the parison would cause the temperature reading to be reduced as the parison is further away from the camera. This could result in a large measurement error, therefore an offset was needed to correct for these inaccuracy. Apart from the effect of spatial resolution, the different distances of the parisons have an effect on the radiation received by the IR detector. The emitted infrared energy is attenuated by the atmosphere and it is a function of the distance causing the parison in further section appear to be colder. Therefore, an offset is applied based on the FLIR's built-in atmospheric models.

Another issue that was dealt with is the focus of the camera system. Ideally each parison from each section should be focused individually. A parison that is out of focus does not show the true temperature reading since temperature is corrupted by out of focus blurring. Constant adjustment of focus would cause

mechanical wear and tear and the speed of focus adjustment is a slow process relative to the machine speed, therefore a single optimal focus distance was investigated and this focus distance applied to every parison from each section.

The other issue encountered was the blurring of the parison due to the slow camera's detector response time. The blurring artefacts cause the camera to perceive the parison's temperature to be lower, therefore reducing the accuracy of the camera system. An image deblurring algorithm was developed to reduce this blurring artefact. Initially, a shift invariant deblurring algorithm was developed to reduce linear blur/shift invariant blur. Since the movement of the parison is rotational, the algorithm was modified to cope with the shift variant properties of the rotational blur. This is done by first converting the image so that the rotational blur becomes a shift invariant linear blur. Then a conventional linear deblur algorithm was applied to the transformed image. The algorithm was tested in the lab environment where all parameters (motion speed, camera time constant, image resolution) for the algorithm were known, the results show that it could successfully deblur an image. However, when it was tested in the practical situation, the algorithm became unreliable since the input parameters were an estimation of the real parameters. Due to the sensitivity of the algorithm to its input parameters, a small deviation from the real parameters would cause a significant temperature change.

This limitation causes the system to be less robust when it is used purely for temperature reading. However, when it is used to monitor trend of the parison temperature, the system would be able to aid operators in optimising the I.S. machine. It would be used to identify faults in mould when the parison temperature starts to decrease or increase beyond a control limit. It could also be used to detect faults in the mould cooling by monitoring the trend of the parison's temperature.

In order for the system to be able to provide reliable temperature readings, a "fast" photon detector based cooled camera could be used, as described in Section 6.1, these cameras are based on an electronic mechanism, direct conversion of the photon flux into an electrical signal (photocurrent), therefore it allows the possibility to change the integration/exposure time of the camera. The integration time can be set much lower than the time constant of a

microbolometer, this would allow a sharp image to be captured and accurate temperature analysis could be performed.

120

References

ANDERSON, Mathias (2005). *Image Processing Algorithms for Compensation of Spatially Variant Blur*. Linköping , Linkopings Universitet.

ARDAGH GROUP (2011). *Glass Making Process.* [online]. Last accessed 26 April 2012 at: http://www.anchorglass.com/glassmaking-process/

BRAMBLE, Reace (2012). *The Chemistry of Soda Lime Glass.* [online]. Last accessed 10 September 2012 at: https://sites.google.com/site/thechemistryofblank/

BUDZIER, Helmut and GERLACH, Gerald (2011). *Thermal Infrared Sensors-Therory, Optimisation and Practice*. West Sussex, UK, John Willey & Sons.

BUDZIER, Helmut, et al. (2006). Fast Microbolometer based Infared Camera System. *DIAS Infrared GmbH Publications*, (20),.

C.HOLST, Gerald (2000). *Common Sense Approach To Thermal Imaging*. Washington and Florida , USA, SPIE Optical Engineering Press and JCD Publishing.

CALEX ELECTRONICS LIMITED (2012). *Infrared Pyrometry*. [online]. Last accessed 8 8 2012 at: http://www.calex.co.uk/downloads/application_guidance/ir_in_glass_industry.pdf

CAMBRIDGE IN COLOUR (2012). *Depth Of Field.* [online]. Last accessed 2 September 2012 at: http://www.cambridgeincolour.com/tutorials/depth-of-field.htm

CHANDA, Bhabatosh and MAJUMDER, Dwijesh Dutta (2006). *Digital Image Processing and Analysis*. New Delhi, Prentice Hall.

EDDINS, Steve (2007). *Image Deblurring-Weiner Filter.* [online]. Last accessed 1 June 2011 at: http://blogs.mathworks.com

EMHART GLASS (2012). *Glass Education.* [online]. Last accessed 25 April 2012 at: http://gpi.org/glassresources/education/

FLIR AB (2005). *ThermoVision SDK*. FLIR.

FLIR AB (2012). *The Ultimate Infrared Handbook for R&D Professionals*. FLIR.

FLIR CORES AND COMPONENTS (2012). *Knowledge Base.* [online]. Last accessed 7 October 2012 at: http://www.flir.com/cvs/cores/knowledgebase/

GONZALEZ, Rafael C. and WOODS, Richard E. (2008). *Digital Image Processing*. 3rd ed., Prentice Hall.

HANSINOFF, Samuel W. (2012). *Photon, Poisson noise.* [online]. Last accessed 1 October 2012 at: http://people.csail.mit.edu/hasinoff/pubs/hasinoff-photon-2012-preprint.pdf

HAYDEN, Brendan F. (2005). *INF.* [online]. Last accessed 1 October 2012 at: http://homepages.inf.ed.ac.uk

HOCKINGS, Colin (2001). *Infrared System Specifications*. [online]. Last accessed 13 May 2012 at: http://www.ndt.net/apcndt2001/papers/867/867.htm

HOGGAR, S.G (2006). *Mathematics of Digital Images*. Glasgow, Cambridge University Press.

HOILUND, Carsten (2007). *The Radon Transform*. Aalborg, Aalborg University.

HYRE, Matthew (2007). Matching Mould Cooling Strategies to the blank side Forming Process. *Glass Machinery Plants & Accessories*, (6), 76-79.

KANG, Younsik (2011). *Investigation of a Localized Approach to Shift Invariant Image Restoration and Robust Autofocusing*. New York, Stony Brook University.

L.WILLIAMS, Thomas (2009). *Thermal Imaging Cameras, Characteristics and Performance*. Florida , USA, CRC Press.

MADDING, Robert P., L.ORLOVE, Gary and LYON, Bernard R. (2006). The Importantce of Spatial Resolution in Infrared Thermograhy Temperature Measurement. *InfraMation* ,.

MINKINA, waldemar and DUDZIK, Sebastian (2009). *Infrared Thermography Errors and Uncertainties*. West Sussex, UK, John Wiley and Sons Ltd.

MOGHADDAM, Mohsen Ebrahimi and JAMZAD, Mansour (2004). Finding Point Spread Function of Motion Blur Using Radon Transform and Modeling the Motion Length. In: *Signal Processing and Information Technology*, 18-21 Dec. 2004. , 314-317.

MOGHADDAM, Mohsen Ebrahimi and JAMZAD, Mansour (2006). Motion Blur Identification in Noisy Images using Mathematical Models and Statistical Measures. *Pattern Recognition Society*,.

MOGHADDAM, Mohsen Ebrahimi and JAMZAD, Mansour (2006). Motion Blur Identification in Noisy Images using Mathematical Models and Statistical Measures. *Pattern Recognition Society*, **40** (7), 1946-1957.

MÖLLMANN, Klaus-Peter, et al. (2006). Thermal Image Quality - Visualization of Spatial and Thermal Resolution in Thermal Imaging. In: *InfraMation*, , 79-91.

MURRAY, Johan (2012). *FLIR Support Centre*. [online]. Last accessed 2012 at: flir.custhelp.com

NORTHERN ARIZONA UNIVERSITY (2009). *Glossary Pp*. [online]. Last accessed 5 September 2012 at: www4.nau.edu

PORT, Roger (2007). *Glass Industry*.

QUINN GLASS (2012). *The Production Process*. [online]. Last accessed 25 April 2012 at: http://www.quinn-glass.com/production_process.cfm

RIBARIC, Slobodan, MILANI, Milivoj and KALAFATIC, Zoran (2000). Restoration of Images Blurred by Circular Motion. In: *Image and Signal Processing and Analysis*, Pula, 14-15 Jun 2000. , 53-60.

SHARMA (2004). *Infared Detectors*. Bombay,

SOLOMON, Chris and BRECKON, Toby (2011). *Fundamentals of Digital Image Processing*. Sussex, Wiley-Blackwell.

TAYLOR, James (2009). *An Introduction to Infrared Temperature Measurement*. Dronfield, UK, Land Instruments International Ltd.

TRANTA, Beata Oswald, MARIOSORGER and O'LEARY, Paul (2010). Motion Deblurring of Infrared Images from Microbolometer Camera. *Infrared Phyics & Technology*, **53** (4), 274-279.

VALLEY DESIGN (2012). *Pyrex*. [online]. Last accessed 10 September 2012 at: http://www.valleydesign.com/pyrexpic.htm

VOLLMER, Michael and MOLLMANN, Klaus Peter (2010). *Infrared Thermal Imaging*. Weinheim, Germany, Wiley VCH.

WANG, Yubing (2006). *Survey of Objective Video Quality Measurements*. Worcester, Worcester Polytechnic Institute.

WANG, Lu, WANG, Chen and PENG, Silong *Pixel-Wise Deconvolution of Rotational Motion Blurred Image with A Sparse Prior*. Beijing, The National Engineering and Technology Research Center for ASIC Design.

WANSBROUGH, Heather (2012). *Glass Manufacture*. [online]. Last accessed 12 March 2012 at: http://nzic.org.nz/ChemProcesses/inorganic/9A.pdf

XPAR VISION (2012). *Blank Temperature Control*. [online]. Last accessed 1 8 2012 at: http://www.xparvision.com/products/btc

YILDIRIM, Mehmet (2000). *Modeling Second Generation FLIR Sensor Detection Recognition and Identification Range with Polarization Filtering*. Monterey, Naval Postgraduate School.